Spring 5-15-2017

PET/MR imaging of hypoxic atherosclerotic plaque using 64Cu-ATSM

Xingyu Nie
Washington University in St. Louis

WASHINGTON UNIVERSITY IN ST. LOUIS

School of Engineering & Applied Science
Department of Biomedical Engineering

Dissertation Examination Committee:
Pamela K. Woodard, Chair
Suzanne Lapi, Co-Chair
Mark Anastasio
Richard Laforest
Rudy Yoram
Jie Zheng

PET/MR Imaging of Hypoxic Atherosclerotic Plaque Using ^{64}Cu-ATSM

by

Xingyu Nie

A dissertation presented to
The Graduate School
of Washington University in
partial fulfillment of the
requirements for the degree
of Doctor of Philosophy

May 2017
St. Louis, Missouri

Table of Contents

List of Figures

List of Tables

List of Abbreviations

Abbreviation	Definition
3D	3 dimensional
AC	attenuation correction
A/M	aortic arch-to-muscle
$ApoE^{-/-}$	apolipoprotein E knockout
BM	background muscle
CEA	carotid endarterectomy
Cu-ATSM	Cu-diacetyl-bis (N^4-methylthiosemicarbazone)
DCE	dynamic contrast enhancement
FDA	food and drug administration
FWHM	full width at half maximum
^{18}F-FDG	^{18}F-fluorodeoxyglucose
H&E	hemotoxylin and eosin
HD	high definition
HFD	high-fat (Western type) diet
HIF	hypoxia inducible factor
IF	injured femoral artery
IHC	immunohistochemistry
LDL	Low-density lipoprotein
ML	maximum-likelihood
MRI	magnetic resonance imaging
OP-OSEM	ordinary Poisson ordered subsets expectation maximization
PD	Photon density
PET	positron emission tomography
PIMO	pimonidazole
pO2	partial pressure of oxygen
PSF	point spread function
PSF-OSEM	point spread function corrected ordered subset expectation maximization
PVC	partial volume correction

PVE	partial volume effect
SCD	standard-chow diet
SD	standard deviation
SEM	standard error of mean
SF	sham-operated femoral artery
SNR	signal-to-noise ratio
SUV	standardized uptake value
TAC	time activity curve
TSE	turbo spin echo

Acknowledgments

I would thank Pamela K. Woodard, Suzy E. Lapi, Richard Laforest, Jie Zheng, Mark Anastasio, and Yoram Rudy for their mentoring and advice; the staff of Small Animal Imaging Facility and Center for Clinical Imaging and Research (CCIR) at Washington University School of Medicine and Barnes Jewish Hospital (Nicole Fettig, Margaret Morris, Amanda Roth, Lori Strong, Ann Stroncek, Glenn Foster, Linda Becker, Michael Harrod, Pamela Baum, David Muccigrosso, Susie Grathwohl, *Rich Pierce*) for their technical supports in the animal and human imaging studies; the Mallinckrodt Institute of Radiology (MIR) Cyclotron Facility (Tom Voller, Paul Eisenbeis Efrem Mebrahtu, Evelyn Madrid) for supplying ^{64}Cu isotopes and ^{64}Cu-ATSM patient doses; the Randolph laboratory (Gwendalyn Randolph, Andrew Elvington, Sahshi Bala , Lea Johnson) for their assistance in immunohistochemistry staining; Lapi lab (Nilantha Bandara, Lake Wooten, Bernadette Marquez, Efrem Mebrahtu, Alex Zheleznyak, Tolu Aweda, Brian Wright, Jennifer Burkemper,) and many other collaborators at Washington University in St. Louis (Robert Gropler, Dana Abendschein, Yongjian Liu, Hannah Luehmann, Lisa Detering, Jinbin Xu, Jeff M. Lau, Kathryn Andel, Janice Francis) for their ideas and helpful assistance during the thesis study in various aspects.

I appreciate the following sources who generously provided funding to support my work and life: sponsorship from the Department of Biomedical Engineering at Washington University in St. Louis, a pilot grant from the Diabetic Cardiovascular Disease Center (DCDC) at Washington University Institute of Clinical and Translational Sciences, grant UL1TR000448 from the National Center for Advancing Translational Sciences (NCATS) at the National Institutes of Health (NIH),

grant DESC0002032 from the Department of Energy, and NIH National Research Service Award (5-T32-HL07081-38) from the National Heart, Lung and Blood Institute.

In addition, I would like to say thanks to my parents, relatives and friends in China who had few opportunities to get together with me even in the most important festivals during the past five and half years. I'm also grateful to the people I met in St. Louis and other places in the United States who show their warmth and kindness to me.

Xingyu Nie

Washington University in St. Louis

May 2017

ABSTRACT OF THE DISSERTATION

PET/MR Imaging of Hypoxic Atherosclerotic Plaque Using ^{64}Cu-ATSM

by

Xingyu Nie

Doctor of Philosophy in Biomedical Engineering

Washington University in St. Louis, 2017

Professor Pamela K. Woodard, Chair

Professor Suzanne Lapi, Co-Chair

It is important to accurately identify the factors involved in the progression of atherosclerosis because advanced atherosclerotic lesions are prone to rupture, leading to disability or death. Hypoxic areas have been known to be present in human atherosclerotic lesions, and lesion progression is associated with the formation of lipid-loaded macrophages and increased local inflammation which are potential major factors in the formation of vulnerable plaque. This dissertation work represents a comprehensive investigation of non-invasive identification of hypoxic atherosclerotic plaque in animal models and human subjects using the PET hypoxia imaging agent ^{64}Cu-ATSM.

We first demonstrated the feasibility of ^{64}Cu-ATSM for the identification of hypoxic atherosclerotic plaque and evaluated the relative effects of diet and genetics on hypoxia progression in atherosclerotic plaque in a genetically-altered mouse model. We then fully validated the feasibility of using ^{64}Cu-ATSM to image the extent of hypoxia in a rabbit model with atherosclerotic-like plaque using a simultaneous PET-MR system. We also proceeded with a pilot clinical trial to determine whether ^{64}Cu-ATSM MR/PET scanning is capable of detecting hypoxic carotid atherosclerosis in human subjects.

In order to improve the ^{64}Cu-ATSM PET image quality, we investigated the Siemens HD (high-definition) PET software and 4 partial volume correction methods to correct for partial volume effects. In addition, we incorporated the attenuation effect of the carotid surface coil into the MR attenuation correction μ-map to correct for photon attention.

In the long term, this imaging strategy has the potential to help identify patients at risk for cardiovascular events, guide therapy, and add to the understanding of plaque biology in human patients.

Chapter 1: Introduction

1.1 Significance

Cardiovascular atherosclerosis is the leading cause of death worldwide despite primary and secondary prevention. Cardiovascular disease impacts the public broadly and affects an estimated 80 million people in the United States (*1*). Each year more than a million people in the United States experience a sudden cardiac event (acute coronary syndrome or sudden cardiac death) and an additional 700,000 experience stroke (*2*). Diabetes mellitus, another leading cause of morbidity and mortality in Western nations, is strongly associated with accelerated atherosclerosis – 86% of patients with newly diagnosed diabetes have atherosclerosis and as blood glucose levels increase, the incidence of clinical or preclinical atherosclerosis also increases (*3*).

Cardiovascular atherosclerosis is a systemic degenerative and inflammatory vascular disease that develops over decades, leading to advanced lesions characterized by a lipid core separated from the lumen by a fibrous cap. It has been recognized that plaque composition more than the degree of luminal stenosis determines the risk of acute clinical events (e.g. stroke, myocardial infarction) (*4*). Macrophage-rich plaques with a thin fibrous cap, large lipid core, and abundance of leaky microvessels tend to be more vulnerable (*4*). The rupture or erosion of the fibrous cap in vulnerable plaque may lead to thromboembolization and arterial occlusion (*5*, *6*).

There is growing evidence that hypoxic plaques are more likely to develop angiogenesis which leads to thrombosis (*2*, *3*). Additionally, there is some suggestion that plaque hypoxia is increased in patients who are diabetic (*7*, *8*). However, at present there is a lack of an effective approach to monitor non-obstructive asymptomatic but potentially unstable atherosclerosis. It will be

significant to find a competent, inexpensive, non-toxic PET imaging agent to detect potentially unstable atherosclerosis, and ideally, have it be FDA approved for commercialization.

1.2 Innovation

This study may represent the first use of Cu-ATSM, the first bis(thiosemicarbazone) complexes demonstrated to exhibit hypoxia selectivity (*9-11*), to target hypoxic atherosclerosis. We hypothesize that the tumor hypoxia PET imaging agent ^{64}Cu-ATSM can be able to detect hypoxia in atherosclerotic plaque in animal and human subjects using the PET-CT or PET-MRI imaging system.

Despite the relatively extensive use of Cu-ATSM in oncology (*12-14*), its use in cardiology has so far been limited. Retrospective review of PET-CT examinations in cervical cancer patients imaged with ^{64}Cu-ATSM at our institution revealed ^{64}Cu-ATSM uptake in regions corresponding to atherosclerosis. Although ^{18}F-fluorodeoxyglucose (FDG), an agent used to image metabolic activity as a glucose analog, is well-described as an agent in atherosclerosis imaging (*15*) and has been shown to detect vascular atheroma (*15*), it provides limited value for evaluating the coronary arteries due to the confounding effects of myocardial uptake of the radiotracer. If successful, ^{64}Cu-ATSM imaging would overcome this limitation. ^{18}F-FMISO is one of the most commonly used investigational PET agents for the measurement of tumor hypoxia (*16*). However compared to ^{64}Cu-ATSM, it has two major disadvantages: low cellular uptake and slow washout from normoxic tissue (*16*). The more efficient uptake and washout kinetics of ^{64}Cu-ATSM in hypoxic and normoxic cells offers the possibility of a fast and efficient means of detecting hypoxia by PET imaging. ^{18}F-EF5 has also been studied to detect hypoxic plaques in atherosclerotic mice by *ex vivo* methods, but the slow blood clearance and high adventitial uptake limit its value for in vivo imaging of atherosclerosis (*17*). These anecdotal findings raised the suggestion that ^{64}Cu-ATSM

is a more discriminating agent and led us to perform some basic preclinical experiments to assess our hypothesis.

Nevertheless, it has been shown that ^{64}Cu-ATSM is a valid PET hypoxia marker in some tumor types, but not for all (*18*). This cell–dependent hypoxia selectivity of ^{64}Cu-ATSM, along with its time-dependent spatial distribution and retention kinetics suggested in other studies, challenges the use of ^{64}Cu-ATSM as a universal PET hypoxia marker (*18-23*) . Therefore, further studies are needed to validate the retention behavior for this PET marker in hypoxic atherosclerotic plaques.

In this dissertation research, we imaged the hypoxic atherosclerosis in both animal and human subjects *in vivo* using ^{64}Cu-ATSM, and following removal of the diseased sections in animals, assessed its histopathologic characteristics *ex vivo*. In addition, we used the hypoxia-specific dye pimonidazole (PIMO). It is a 2-nitroimidazole containing a basic, piperidine moiety and reduced in cells with low oxygen tension ($pO_2 \leq 10$ mm Hg). The resulting PIMO derivatives form protein adducts, which can be detected by immunostaining (*24*). This agent primarily has been used in oncologic specimen assessment (*25*) and only recently in assessment of atherosclerosis (*26*). Another highly innovative aspect to this study is our work to image these subjects simultaneously by MR and PET in a newly acquired state-of-the-art PET-MRI system (Biograph mMR, Siemens, Erlangen, Germany). This system, which was FDA approved in June, 2011, is one of only several currently operational in the United States. This system uses MRI for attenuation correction as well as diagnostic imaging allowing for simultaneous co-registered high-resolution 3 Tesla MR imaging of rabbit's femoral artery or human's carotid atherosclerosis anatomy and ^{64}Cu-ATSM PET imaging. Lastly, this study incorporated advanced partial volume correction techniques and coil-attenuation correction method for PET image quality improvement.

1.3 Specific Aims

This research evaluated the PET hypoxia imaging agent ^{64}Cu-ATSM for non-invasively identifying and characterizing hypoxic atherosclerotic plaque. In the long term, this imaging strategy will help identify patients at risk for cardiovascular events, guide therapy, and study plaque biology in human patients.

As such, in the dissertation work, a dedicated, start-to-finish process for a ^{64}Cu-ATSM simultaneous PET-MRI examination, together with the image processing and histopathological correlation studies has been conducted to detect hypoxic atherosclerosis in animal and human subjects. The specific aims for this work are as follows:

Specific Aim 1: Radiolabeling of ^{64}Cu-ATSM compounds

I practiced the steps of processes to radiolabel of ^{64}Cu with ATSM compounds using in-house methods for future pre-clinical and clinical studies.

Specific Aim 2: Evaluating the capability of ^{64}Cu-ATSM PET imaging for determining hypoxia in atherosclerotic plaque.

I first demonstrated the feasibility of ^{64}Cu-ATSM for the identification of hypoxic atherosclerotic plaque and evaluate the relative effects of diet and genetics on hypoxia progression in atherosclerotic plaque in a genetically-altered mouse model. We then fully validated the feasibility of using ^{64}Cu-ATSM to image the extent of hypoxia in a rabbit model of atherosclerotic-like plaques using a simultaneous PET-MR system. Finally, we proceeded with a pilot clinical trial to determine whether ^{64}Cu-ATSM MR/PET scanning is capable of detecting hypoxic carotid atherosclerosis in human subjects.

Specific Aim 3: Improving ^{64}Cu-ATSM PET image quality via corrections for partial volume effects and photon attention effects.

I improved the ^{64}Cu-ATSM PET image quality though: (1) reconstructing the PET image using Siemens HD (high-definition) PET software incorporating our optimized reconstruction parameters; (2) investigating 4 partial volume effects (PVE) correction methods using phantom and clinical data; (3) incorporating attenuation effects of the carotid surface coil in the MR attenuation correction (AC) μ-map for PET image reconstruction.

This dissertation represents a development of ^{64}Cu-ATSM as a hypoxic atherosclerotic plaque imaging agent to identify carotid atherosclerotic plaque clinically. Correction for spillover/partial volume effects and photon attenuation effects were investigated to improve the PET image quality. Correlation between the ^{64}Cu-ATSM uptake with atherosclerotic parameter measured by MRI and immunohistochemistry staining solidly confirmed the finding of atherosclerosis and validated the potency of ^{64}Cu-ATSM to identify carotid atherosclerosis in patients.

Chapter 2: ^{64}Cu-ATSM-PET imaging of hypoxia in atherosclerosis

Using ^{64}Cu-ATSM to target hypoxic cells within plaque is of interest to us because this imaging radiopharmaceutical has been used extensively in preclinical models and human subjects to assess tumor hypoxia in oncology but its use in cardiology has so far been limited to assessing myocardial ischemia (*11, 27-29*). However, there is growing evidence that the combination of increased oxygen demand together with impaired oxygen diffusion capacity also results in the presence of severe hypoxia (<1% oxygen) in macrophage-rich zones into the lesion (*26, 30-32*).

2.1 Atherosclerosis: a dangerous chronic cardiovascular disease

The development of atherosclerosis in individuals with hyperlipidaemia and signs of systemic inflammation is initiated by the activation and dysfunction of endothelial cells (*33*). This local endothelial-cell defect promotes the adhesion of leukocytes and activated platelets to the damaged endothelium and leads to an increase in the permeability of blood vessels for lipid components in the plasma, such as low-density lipoprotein (LDL). Monocytes, which become loaded with cell-activating oxidized LDL (oxLDL) and other lipids, then accumulate in the evolving lesion and transform into foam cells to form early plaques (known as fatty streaks) in the intima. The intima then becomes thicker as a result of a pathophysiological response to changes in fluid dynamics at atherosclerosis-prone areas of the arterial tree, such as artery branching points. Fatty streaks progress into advanced atherosclerotic plaques following the accumulation of additional inflammatory-cell subsets and extracellular lipids to form a core region that is surrounded by a cap of smooth muscle cells (SMCs) and a collagen-rich matrix. The secretion of cytokines and growth factors by plaque cells, and the further deposition of extracellular matrix components, contribute

to the progression of plaques that cause a narrowing of the arterial lumen (stenosis). The central core of the mature plaques can become necrotic, and neovascularization in the plaques can allow leakage of blood components and haemorrhage (*33*) (Fig. 1).

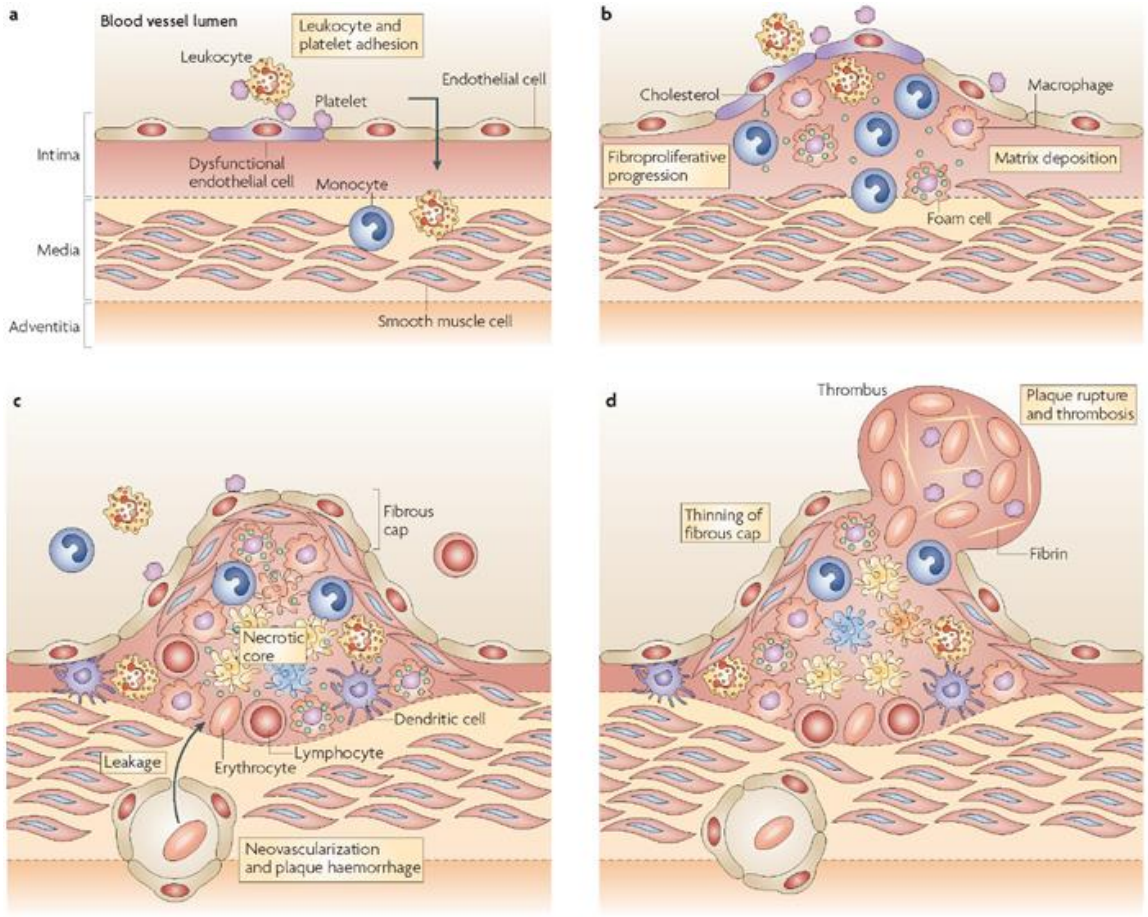

Figure 1 The progression of atherosclerotic lesions. a). Endothelial-cells become dysfunctional and are activated by hyperlipidemia which leads to a pro-inflammatory state, early platelet and leukocyte adhesion, and increased endothelial permeability. b). In early lesions, monocytes are recruited to the intima and subintima. These monocytes scavange lipids and, thus, turn into macrophages (foam cells). Grossly, this appears as fatty streaks along the intima of the artery wall. Monocytes continue to enter, and matrix components and vascular smooth muscle cells cause plaque fibroproliferative progression. c). In advanced lesions, hypoxia and apoptosis of macrophages causes a necrotic core. A fibrous cap develops. When a plaque is hypoxic, neovascularization can develop. This often begins in the adventitia. Disruption of the neoangiogenesis can lead to plaque hemorrhage and rupture. d). Ruptured plaque often occurs after thinning and erosion of the fibrous cap, causing instability. This often leads to arterial occlusion causing myocardial infarction or stroke. (*33, 34*) (Adapted from "The multifaceted contributions of leukocyte subsets to atherosclerosis: lessons from mouse models," by Christian Weber, Alma Zernecke and Peter Libby, 2008, Nature Reviews Immunology, Volume 8, p802-815. Copyright (2008) by title of publisher.)

The atherosclerotic lesions, or atherosclerotic plaques, are roughly separated into two broad categories: stable and unstable (also called vulnerable) (*35*). In general, stable atherosclerotic plaques are rich in extracellular matrix and smooth muscle cells, and tend to be asymptomatic. On the other hand, unstable plaques are characterized by weak and rupture-prone extracellular matrix separating the lesion from the arterial lumen (also known as the fibrous cap), rich macrophages and foam cells, large lipid-rich necrotic core, increased plaque inflammation, positive vascular remodeling, increased vasa-vasorum neovascularization, and intraplaque hemorrhage (*36, 37*). Ruptures of the fibrous cap expose thrombogenic material, such as collagen, to the circulation and eventually induce thrombus formation in the lumen. Upon formation, intraluminal thrombi can occlude arteries outright (e.g., coronary occlusion), but more often they detach, move into the circulation, and eventually occlude smaller downstream branches causing thromboembolism (e.g. coronary thrombosis causing myocardial infraction) (*38*). Apart from thromboembolism, chronically expanding atherosclerotic lesions can cause complete closure of the lumen. Chronically expanding lesions are often asymptomatic until lumen stenosis is so severe (usually over 80%) that blood supply to downstream tissue(s) is insufficient, resulting in ischemia (*38, 39*).

Atherosclerotic plaque is dangerous because it's so “stealthy”. This process of narrowing and hardening of the arteries occurs over decades, usually without any symptoms (*40*). It affects the entire artery tree, but mostly larger, high-pressure vessels such as the coronary, renal, femoral, cerebral, and carotid arteries (*39*). However, because early and intermediate atherosclerotic lesions of atherosclerosis is “clinically silent” (*41*), the person may notice the problem and not seek medical until advanced lesions have ruptured to cause infraction, or when they do, physicians do not recognize what has happened. It is thus essential to identify the vulnerable atherosclerosis in the arteries before the life-threatening catastrophic events take place.

2.2 Hypoxia in atherosclerotic lesions

It has been demonstrated that atherosclerotic lesions, in particular macrophage-rich areas in advanced plaques which are more vulnerable, contain regions of severe hypoxia (*26, 31*).

Recent studies have shown that hypoxia is involved in several processes that contribute to the progression of atherosclerotic lesions (Fig. 2). In the initial stages of atherogenesis, modified lipoproteins recruit monocytes and T cells into the intima (*42*). Recruited monocytes differentiate into macrophages and internalize the modified lipoproteins, resulting in the accumulation of highly oxygen-consuming lipid-loaded macrophages (also known as foam cells) in developing lesions before cell apoptosis (*43*). The intima and media of the artery wall rely on oxygen supplied from the luminal blood and the adventitial vasa vasorum, and the maximum oxygen diffusion limit (100-200 μm) is often exceeded in developing lesions (*44*). Thus, the combination of increased oxygen demand together with insufficient oxygen supply results in the presence of severe hypoxia (<1% oxygen) in macrophage-rich zones 150-300 μm into the lesion (*26, 31*).

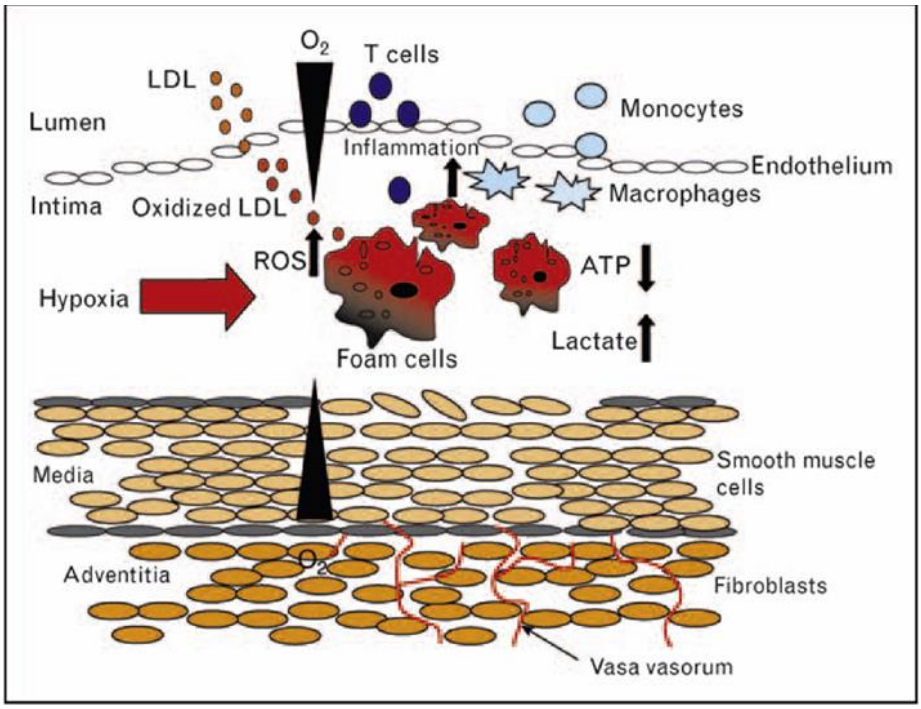

Figure 2 Hypoxia promotes the formation of highly oxygen-consuming, lipid-loaded foam cells. Exposure of macrophages to hypoxia resultes in chemokine secretion which promotes recruitment of monocytes and T cells to induce an inflammatory response, and increased lactate and decreased ATP levels in hypoxic macrophages which promote progression of advanced lesions, and increased LDL oxidation which further promotes formation of foam cells. (Adapted from "The role of hypoxia in atherosclerosis," by Hultén, Lillemor Mattsson and Levin, Max, 2009, *Current Opinion in Lipidology, Volume 20(5), p 409-414.* Copyright (2009) by title of publisher.)

Lesion hypoxia thus may be a key factor in the progression to advanced atherosclerosis by promoting lipid accumulation, inflammation, ATP depletion and angiogenesis.

First, hypoxia promotes formation of foam cells. Foam cells are characteristic of both early and late atherosclerotic lesions (*45, 46*), and hypoxia converts human macrophages to into triglyceride-loaded foam cells (*47*). It has been demonstrated that exposure of human macrophages to hypoxia increases the accumulation of triglyceride-containing cytosolic lipid droplets and differentiation-related protein (ADRP) expression, even in the absence of exogenous lipids (*47*).

Second, hypoxia promotes inflammation. Hypoxia has been shown to influence gene expression in macrophages, leading to an inflammatory response with increased production of the T cell attractant IL-8/CXCL8 (*48*). Hypoxia-induced chemokine secretion from macrophages leads to

the recruitment of T cells and monocytes to atherosclerotic plaques and, subsequently, to plaque progression (*49*). Additionally, the hypoxia-induced activation of macrophages plays a role in the production of reactive oxygen species and subsequent lipoprotein modification (*48, 50*).

Third, hypoxia induces ATP depletion. The most central role of oxygen is to maintain mitochondrial ATP production. Macrophages maintain ATP levels in a 100-200 μm rim of the hypoxic zone of advanced lesions, which is the rim closest to the lumen (*51*). This is not surprising because macrophages efficiently adapt to hypoxia by producing ATP from anaerobic glycolysis (*51*). Glycolysis, however, is energy-inefficient and consumes 15 times more glucose per ATP molecule produced than mitochondrial ATP production. To satisfy the high glucose demand, there is an upregulation of the hypoxia-inducible transcription factor (HIF)-1α-regulated glucose transporter GLUT-3 in hypoxic macrophages (*26*). The extensive glycolysis also promotes lactate accumulation with the lesion, which results in decreased pH and increased binding of native and modified lipoprotein to human proteoglycans, a mechanism that may enhance lipoprotein retention and lipid accumulation in the atherosclerotic lesion (*52, 53*). Deeper into the lesion, macrophage ATP production fails because anaerobic glycolysis decreases glucose concentrations. Importantly, ATP-depleted macrophages in this zone remain viable and may be further depleted in lipid-loaded macrophages by the hydrolysis and re-esterification of LDL cholesterol esters in a futile ATP-consuming cycle (*51, 54*). ATP depletion is likely a key factor promoting macrophage death and the formation of necrotic core, a key feature of an unstable lesion and consisted largely of dead macrophages, probably in concert with toxic stimuli such as free cholesterol loading and endoplasmatic stress (*51*).

Moreover, hypoxia induces lesion angiogenesis. A recent study in human atherosclerotic lesions showed a strong correlation between hypoxia and angiogenesis (*26*). It is likely that angiogenesis

is promoted within plaques in an attempt to restore tissue oxygenation and ATP level (*55*). However, lesion angiogenesis may be maladaptive as it not only fails to restore oxygenation but also promotes lesion instability (*44*). One explanation is that lesion angiogenesis is a sign of more hypoxic lesions, and thus more advanced atherosclerosis (*26, 56*). There is also evidence that lesion angiogenesis *per se* may be detrimental. In mice models, angiogenic vessels provide an additional route for inflammatory cells to enter the plaque and thus promote atherosclerosis progression (*57, 58*). In human lesions, angiogenic vessels are structurally defective, showing features typical of vascular endothelial growth factor (VEGF)-induced angiogenic vessels (*59*). Angiogenic vessels formed under the influence of this HIF-1-regulated angiogenic factor are characterized by poorly supported walls, leakiness, and blind-ending vessel tubes, which make perfusion sluggish and oxygen delivery inefficient (*60*). Angiogenesis has been shown to correlate with VEGF in human atherosclerotic lesions (*26*), and thus hypoxia-induced increases in VEGF may contribute to the development of unstable lesions by promoting angiogenesis.

In conclusion, in spite that additional studies are required to understand the precise mechanisms involved in the many responses to hypoxia in the process of atherogenesis, the level of hypoxia has pronounced effects on almost every aspect of cell physiology (*61*). In particular, our focus was on the role of hypoxia on the formation of lipid-loaded macrophages and increased inflammation. These two responses may be inter-related as recent evidence has shown that lipid droplets are dynamic organelles with many enzymes involved in inflammation located on their surface.

2.3 PET imaging of hypoxia

In recent decades there has been increasing interest in developing methods for measuring the levels of oxygen in tumors, which can probably be expanded to other human tissues such as atherosclerotic plaques. The existing techniques for *in vivo* evaluation tissue hypoxia status was

summarized in (*62*).These methods can be separated into three major groups: methods directly related to assessing the oxygen concentration (e.g. oxygen electrodes/optodes, phosphorescence quenching, photoacoustic lifetime imaging, electron paramagnetic resonance (EPR), overhauser-enhanced MRI), methods reporting on the physiologic processes involving oxygen molecules (e.g. detection of metabolized exogenous markers PET and PIMO, near-infrared spectroscopy (NIRS), blood oxygen level-dependent (BOLD) MRI, dynamic contrast-enhanced (DCE) MRI, photoacoustic tomography), and methods evaluating the expression of endogenous markers as a response to hypoxia (e.g. CAIX, HIF-1α, GLUT-1, OPN, LOX, Ephrin A1, Galectin 1) (*62*).

These methods can be invasive, such as the polarographic O_2 sensor (Eppendorf GmbH, Hamburg, Germany), or non-invasive, mainly based on imaging techniques (*63, 64*). Non-invasive imaging modalities are undoubtedly more appealing for the assessment of tissue hypoxia because they guarantee all-encompassing visualization and can identify the phenomenon even at sites inaccessible to invasive procedures. Among the many techniques now available are optical-based methods, magnetic resonance imaging (MRI), and nuclear medicine techniques (*64-66*). Among the potential image-based modalities for hypoxia assessment, positron emission tomography (PET) is one of the most extensively investigated based on the various advantages it offers: (a) a broad assortment of radiopharmaceuticals; (b) reasonable intrinsic resolution (~4 mm); (c) three-dimensional (3D) tissue representation; (d) possibility of semiquantification/quantification of the hypoxic burden; (e) relative ease of use, and (f) ease of repetition (*67*). Compared with the other non-invasive techniques, however, the biggest advantage of PET is that it using certain radiotracers such as ^{64}Cu-ATSM it displays the highest specificity for hypoxic tissue (*68*).

Starting with the 2-nitroimidazole family of compounds in the early 1980s (*66, 69*), a great number of PET tracers have been developed for the identification of hypoxia in living tissues and solid

tumors (Fig. 3; also see Table 2 in (*64*) for details). The driving force behind this development has been the need for highly specific imaging "probes" able to overcome the inconsistent correlation between findings on other imaging modalities, including PET with ^{18}F-fluorodeoxyglucose (^{18}F-FDG), and the hypoxia levels determined in tumor tissue (*66*, *70*, *71*).

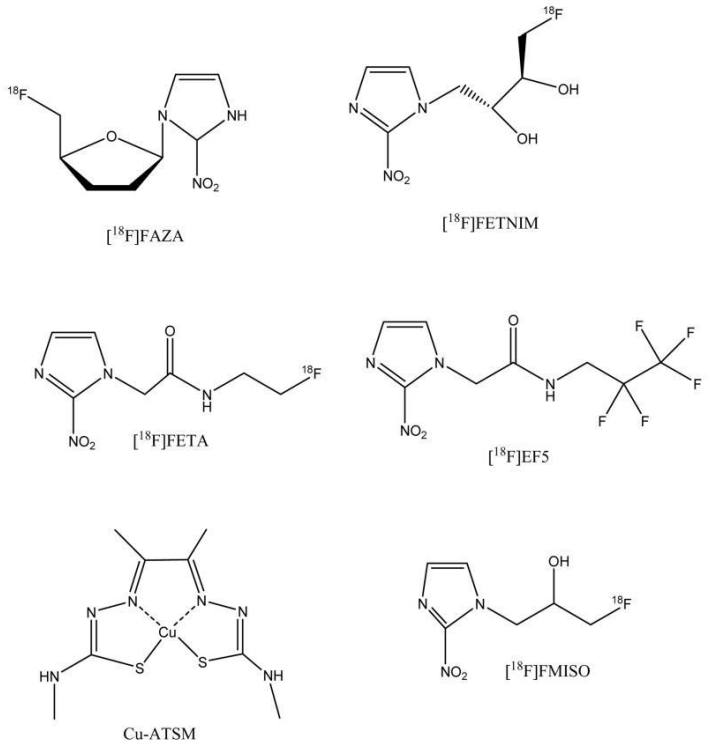

Figure 3 Structure of representative hypoxia PET imaging agents. (Adapted from "Positron Emission Tomography Imaging of Hypoxia," by Suzanne E. Lapi, Thomas F. Voller and Michael J. Welch, 2009, *PET Clin, Volume 4 (1), p39-47.* Copyright (2009) by title of publisher.)

As an FDA approved radiopharmaceutical, ^{18}F-FDG is widely available and remains a cornerstone for the assessment of glucose metabolism in heart, lungs, brain, and tumors in oncology, but it requires careful handling when trying to depict hypoxic tissue (*71*). Patient studies by Folco *el al.* concluded that glucose uptake and therefore FDG uptake signals in atheroma may reflect hypoxia-stimulated macrophages rather than mere inflammatory burden, which suggested that PET imaging using ^{18}F-FDG could detect "active" atherosclerotic plaques (*72*). The fact that tumor hyperglycolysis due to up-regulation of glucose transporters (GLUTs) and glycolytic enzymes can

be can be driven by HIF-1α offers some justification for the use of ^{18}F-FDG as a surrogate marker of hypoxia (*69, 71, 73*) (Fig. 4A). Moreover, under reduced oxygen level (↓pO_2), living cells switch their metabolic pathway for ATP production to anaerobic glycolysis, also known as the Pasteur effect (*74*). In the case of hypoxic tumor cells, a wide overlap exists between ^{18}F-FDG uptake due to aerobic glycolysis, the so-called Warburg effect (*75*), and anaerobic glycolysis (*74, 76*) (i.e., normoxic and hypoxic conditions, respectively) (Fig. 4A). The fact that HIF-1α expression can be observed also in non-hypoxic tumor regions (*77, 78*) suggests that other factors can indirectly influence glucose metabolism and ^{18}F-FDG uptake in those areas (*71*). This limits on the specific application of ^{18}F-FDG for the detection of hypoxia in tumor and probably atherosclerosis.

Several radionuclide-labeled hypoxia markers have been developed for PET – for example, 2-nitroimidazole-containing agents that rely on the reduction of nitro function groups in hypoxia conditions and then covalent binding to macromolecules in hypoxic conditions (e.g. ^{18}F-fluoromisonidazole (FMISO) (*79*), ^{18}F-fluoroazomycinarabinofuranoside (FAZA) (*80*), ^{18}F-tracer 2-(2-nitro-1H-imidazol-1-yl)-N-(2,2,3,3,3-pentafluororpropyl) acetamide (EF5)) (*81*), Cu-containing bis-(thiosemicarbazone) complexes (e.g. Cu-ATSM) that rely on the one-electron reduction of the metal center and ^{99m}Tc-labeled 4,9-diaza-3,3,10,10-tetramethydodecan-2,11-dione dioxime (^{99m}Tc-HL91) that relies the bioreducible property of ^{99m}Tc itself and has been used as markers of myocardial hypoxia (*82*). Silvola et al. introduced ^{18}F-EF5 for its ability of detecting hypoxia in atherosclerotic plaques in mice (*17*). EF5 has been used to detect hypoxia in rodent and human tumors, and it has shown good correlation with other hypoxia markers, such as HIF-1. The study included 2 types of atherosclerotic mice with different genetic backgrounds (low-density lipoprotein receptor$^{-/-}$ apolipoprotein B100/100 and insulin-like growth factor II/ low-density

lipoprotein receptor$^{-/-}$ apolipoprotein B100/100). After dietary induction of plaque development, both types of mice and control mice were injected with ^{18}F-EF5. Large atherosclerotic plaques in mice contained hypoxic areas and showed uptake of ^{18}F-EF5. Their study demonstrated that despite its slow blood clearance, the high uptake of ^{18}F-EF5 in plaques suggested that plaque hypoxia is a potential target for identifying high-risk plaques noninvasively.

Among all the hypoxia PET imaging agents, ^{18}F-fluoromisonidazole (^{18}F-FMISO) has received most attention (*66*). ^{18}F-labeled misonidazole was first proposed as a radioactive derivative of the nitroimidazoles (*83, 84*). Like the other compounds in the nitroimidazole family, this tracer is passively diffused through the cell membrane owing to its lipophilicity, and once within the intracellular environment it is reduced into R-NO_2 radicals by the nitroreductase enzyme (NTR). This process is reversible and when the cell is well oxygenated, the tracer is not entrapped and can freely flow back into the extracellular environment. Conversely, in the presence of reduced levels of oxygen (pO_2 <10 mmHg) the process of ^{18}F-FMISO reduction continues slowly; the consequence is the progressive production of R-NHOH compounds that bind covalently to intracellular molecules, and ultimately entrapment of the tracer within the cell (*16, 85, 86*) (Fig. 4B).

Over the past two decades ^{18}F-FMISO has been extensively studied as a PET agent for imaging hypoxia in both the preclinical and the clinical context and to date (*66*). It has been shown to be retained in hypoxic cells both *in vivo* and *in vitro.* ^{18}F-FMISO has been used in numerous oncology clinical studies including gliomas (*87*), head and neck cancer, and non-small cell lung cancer (*88*). In an early study involving patient with malignant glioma, a feasibility study demonstrated the use of FMISO to detect hypoxia in the brain *in vivo* (*89*). ^{18}F-FMISO is currently the most widely used

PET agent for mapping regional hypoxia and is generally considered to be the gold standard for PET hypoxia imaging (*66*).

Nevertheless, the aspects representing the main drawbacks of ^{18}F-FMISO may limit the applicability of the tracer in clinical practice. Owing to the high lipophilicity and slow kinetics of this tracer, 2-4 h post intravenous injection imaging times are required which is rather long for an ^{18}F-fluorine labeled tracer ($T_{1/2}$ = 109 min) (*90, 91*). In addition, high contrast images are not typical with this agent (tumor-to-plasma or tumor-to-muscle ratio of 1.2-1.4 (*66, 90*)). The slow washout of this tracer leading to a delay time of two hours required after injection to allow for clearance of the tracer from normal background tissues delays imaging and can result in poor statistics and images of limited quality (*92*).

[^{64}Cu]Copper(II)-diacetyl-bis(N^4-methylthiosemicarbazone (^{64}Cu-ATSM) (Fig. 4C) was developed as an alternative to ^{18}F-FMISO (*66*). [^{64}Cu] ($t_{1/2}$ = 12.7 h, β^+ = 17.4%) can be produced in high specific activity in reliable quantities and the longer half-life allows for distribution to centers without a cyclotron over longer distances than possible with ^{18}F (*66*). This isotope also decays by β^- and can therefore have potential as both a diagnostic and therapeutic agent (*9*). Section 2.4 will introduce the properties of ^{64}Cu-ATSM in more detail.

In the assessment of tumor hypoxia, ^{64}Cu-ATSM overcomes many limitations of ^{18}F-FMISO. ^{64}Cu-ATSM is an agent that shows rapid delineation of tumor hypoxia (<1 h), and in high tumor to background tissue ratios (tumor-to-blood ratio >>2.0) which allows prediction of poor response to therapy (*93*). In addition, Cu-ATSM shows higher and faster cellular uptake than FMISO *in vitro*, and correlated with O_2 electrode studies (*93*). The more efficient uptake and washout kinetics

of ^{64}Cu-ATSM in hypoxic and normoxic cells compared to ^{18}F-FMISO offers the possibility of a faster and more selective means of detecting hypoxia by PET imaging.

All of these hypoxia agents have shown certain preferential uptake in hypoxic cells, although thorough validation studies are still needed for them to be used with confidence clinically.

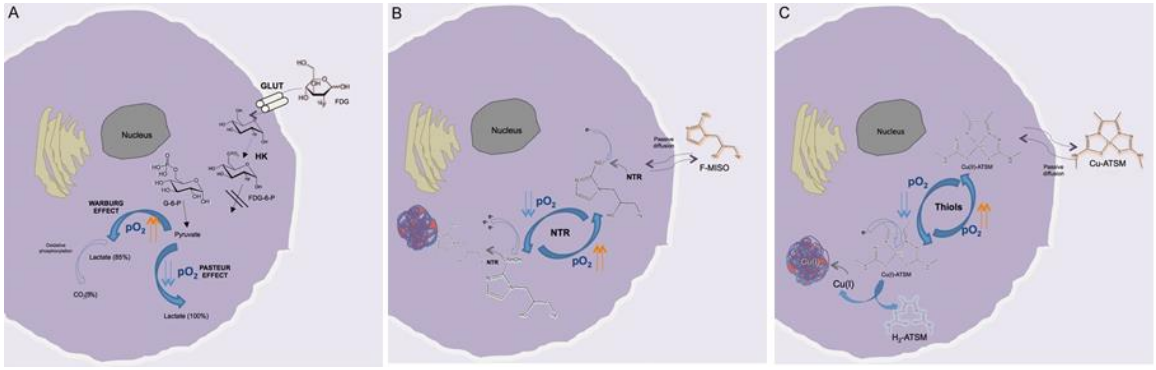

Figure 4 Comparison of the retention mechanisms of (A) FDG, (B) F-MISO (B), and (C) Cu-ATSM (C) in hypoxic living cells. The cellular uptake of FDG occurs both in normoxic (Warburg effect) and hypoxic conditions (Pasteur effect), while the retention of F-MISO and Cu-ATSM after passive diffusion through the cell membrane depends on oxygen tension (pO2) of the cells. In the condition of reduced pO2 (hypoxia), F-MISO is progressively reduced by nitroreductase enzyme (NTR) and covalently bound to the intracellular proteins; Cu(II)-ATSM nuclide is reduced to Cu(I) by the intracellular thiols, and less stable Cu(I)-ATSM complex is progressively dissociated to form H_2-ATSM and free Cu(I), which is very rapidly incorporated into intracellular proteins. In the presence of sufficient O_2 (normoixa) the processes are reversible and the F-MISO and Cu(II)-ATSM molecules are free to leave the cell. (Adapted from "PET radiopharmaceuticals for imaging of tumor hypoxia: a review of the evidence," by Egesta Lopci et al., 2014, Am J Nucl Med Mol Imaging, Volume 4(4), p 365-384. Copyright (2014) by the title of publisher and is released under the "Creative Commons Attribution Noncommercial License (CC BY-NC) License.)

2.4 Cu-ATSM as a hypoxia imaging agent for PET

Cu-ATSM is a promising hypoxia marker in PET imaging with a lot of advantages. The radiolabeling of Cu-ATSM is relatively easy with a 1-step reaction between copper and the substrate. Cu-ATSM has small molecular weight and is a neutral lipophilic molecule and highly membrane permeable; thus, it can diffuse easily from bloodstream to surrounding cells.

The bis(thiosemicarbazone) ligands in Cu-diacetyl-bis (N^4-methylthiosemicarbazone) [Cu-ATSM] derived from 1,2-diones react rapidly with copper to form stable, low molecular weight, neutral complexes which are capable of fast cellular uptake. For thiosemicarbazone complexes,

the reductive potential can be altered to match the bioreductive character of the oxygen-depleted tissue by modifying the chelate. Cu-ATSM depends on its single methyl group, which shifts its Cu(II/I) redox potential by approximately 80 mV. In contrast, the blood perfusion agent ^{64}Cu-pyruvaldehyde-bis(N^4-methylthiosemicarbazone) [PTSM] is not hypoxia selective. This change in chemical property is hypothesized to be due to subtle energy shifts in the frontier orbitals that alter the order and, as a consequence, the occupancy of these orbitals (*94*).

Copper has several positron-emitting isotopes (^{60}Cu, ^{61}Cu, ^{62}Cu, and ^{64}Cu) with various half-lives, ranging from 9.7 minutes for ^{62}Cu to 12.7 hours for ^{64}Cu. This allows a wide choice of isotopes, so that half-life ($t_{1/2}$) and radiation energy level can be tailored to particular needs. ^{60}Cu ($t_{1/2}$ = 23.7 min), ^{61}Cu ($t_{1/2}$ = 3.35 h), and ^{64}Cu ($t_{1/2}$ = 12.7 h) can be produced by proton bombardment of solid targets using a medical cyclotron, while ^{62}Cu is available from a generator similar to that used for ^{99m}Tc (*66, 93*). Among them, Copper-64 is the most commonly used copper isotope (*93*). It has been reported in that ^{64}Ni(p, n)^{64}Cu nuclear reaction can produce large quantities of the nuclide with high specific activity (*95*). The 12.7-hour half-life of ^{64}Cu makes it ideally suited for PET studies that can be conducted over a 48-hour period, while the short half-lives of ^{60}Cu and ^{62}Cu preclude delayed imaging. This long half-life also allows for the regional distribution of this nuclide, as with ^{18}F. Copper-64 decays 17.4% by positron emission and has a β^+ maximum energy of 0.66 MeV, similar to ^{18}F, with an average energy of 0.28 MeV. This low kinetic energy positron results in short positron range (2.4 mm R_{max} and 0.6 mm R_{mean}) and therefore high resolution PET images (*96, 97*). Copper-64 also decays by electron capture (43%) and β^- (43%) and has, therefore, been studied as both a diagnostic and therapeutic radionuclide (*9*).

The first report of the hypoxia selectivity of Cu-ATSM was with ^{62}Cu-ATSM in an isolated rat heart model of ischemia in 1997 by Takahashi and colleagues (*28*), and the first report of Cu-

ATSM in human study was conducted in normal subjects and patients with lung cancer by the same group (*98*). Because of the profound impact of hypoxia on tumor behavior (*99*), ^{64}Cu-ATSM has also been extensively studied subsequently by Michael Welch, Farrokh Dehdashti, Jason Lewis and colleagues in Washington University in St. Louis for noninvasive detection and quantification of tumor hypoxia *in vitro* (*12, 100*) and *in vivo* (*13, 14, 101*).

The retention mechanism of ^{64}Cu-ATSM in viable cells under low cellular partial pressure of oxygen (PO_2) explored by a number of groups in the US, Europe and Japan over the last few decades. Although different schemas in the retention mechanism of Cu-ATSM were proposed in the literature, but, to date, there is a consensus that *in vitro* Cu-ATSM undergoes bioreductive trapping under hypoxic conditions (*11, 102-104*). As presented by Fujiyabashi et al. (*11, 27*), in theory Cu-ATSM Cu(II) is a lipophilic molecule, with high membrane permeability and low redox potential, and is reduced only in hypoxic cells and involves electron transfer from hyper-reduced Complex I (ubiquinone oxidoreductase) using NADH as a two-electron donor. Upon the intracellular reduction, Cu-ATSM becomes trapped irreversibly and thus the radioactivity accumulates in these areas. In normoxic cells, Complex I is incapable of reducing Cu-ATSM (Fig. 4C).

It has been shown that redox potential is the major factor controlling hypoxia selectivity but not the only one: although complexes with potentials in the range -0.57V to -0.59V were all hypoxia selective, they differed in the degree of selectivity (*102*). Varying the alkylation pattern of bis-thiosemicarbazone complexes or substituting sulfur with selenium as the donor atom can change the properties of the thiosemicarbazone complexes. McQuade examined new copper hypoxia PET imaging agents for a higher selectivity for hypoxia or ischemic tissue by increasing alkylation or replacing the sulfur atoms with selenium (*94*). Of the compounds synthesized, only ^{64}Cu-ASSM

(2,3-butanedione bis(-selenosemicarbazone)) and ^{64}Cu-ATSE (diacetyl-bis(N^4-ethylthiosemicarbazone)) could be examined *in vitro* and *in vivo*. The additional alkylation present in Cu-ATSE modifies the hypoxia selectivity and *in vivo* properties when compared with Cu-ATSM. However, the fully alkylated species, ^{64}Cu-ASSM demonstrated no hypoxia selectivity (*94*).

It should be noted that ^{64}Cu-ATSM has been shown to be a valid PET hypoxia marker in some tumor types, but not for all (*18*). Although all types of solid tumors, especially malignant solid tumors, are subject to hypoxia, the oxygen tension in tumors and fraction of hypoxic tumors are significantly varied (also see Table 1 in (*62*)). This cell–dependent hypoxia selectivity of ^{64}Cu-ATSM, along with its time-dependent spatial distribution and retention kinetics suggested in other studies, raises concerns regarding the usage of ^{64}Cu-ATSM as a universal PET hypoxia marker (*18-23*) . Therefore, further studies are needed to validate the retention behavior for this PET marker in hypoxic atherosclerotic plaques.

2.5 Preparation the compound of ^{64}Cu-ATSM

Preparation the compound of ^{64}Cu-ATSM was clearly divided into two major components: ^{64}Cu isotope production and radio-labelling of ^{64}Cu-ATSM. The ^{64}Cu isotope was produced on the Washington University CS-15 cyclotron by the ^{64}N (p,n)^{64}Cu nuclear reaction as previously described (*95, 105*).

2.5.1 Preparation of ^{64}Cu-ATSM doses for preclinical studies

Radioactivity was counted with a Beckman Gamma 8000 counter containing a NaI crystal (Beckman Instruments, Inc., Irvine, CA). EM Science Silica Gel 60 F254 thick-layer chromatography (TLC) plates (10 × 5 cm) were purchased from EMD Millipore Corporation

(Billerica, MA). Radio-TLC plates were analyzed using a BIOSCAN System 200 imaging scanner (Bioscan, Inc., Washington, DC).

Diacetyl-bis (N^4-methylthiosemicarbazonate) [H_2-ATSM] was labeled with ^{64}Cu using the methods developed in house. Briefly, 10 mg of ATSM powder was dissolved in 1 ml of DMSO to give an overall concentration of 10 mg/mL. A total of 1 µL (10 µg) of this solution was then added to 1 µL (~92.5 MBq) of $^{64}CuCl_2$ in 200 µl of 1 M NaOAc or 3 M HCl buffer, at a concentration of 0.46 MBq/µL. This solution was then stirred for 3 to 5 minutes and then allowed to sit briefly at room temperature, after which it was loaded onto a C_{18} Sep-Pak® Light (Waters Corporation, Milford, MA), which had been pre-conditioned with 5 mL of ethanol and 5 mL of water. After loading the sample, 10 mL of water was passed through to remove the DMSO and any unreacted ^{64}Cu. The labeled complex was then eluted in 350 µL of ethanol (following a 150 µL ethanol elution for the void volume). The purity of the labeled material was determined by radio-TLC using silica gel plates with ethyl acetate as the mobile phase. Radiochemical yield was 75-85% and purity > 95% (Fig 5).

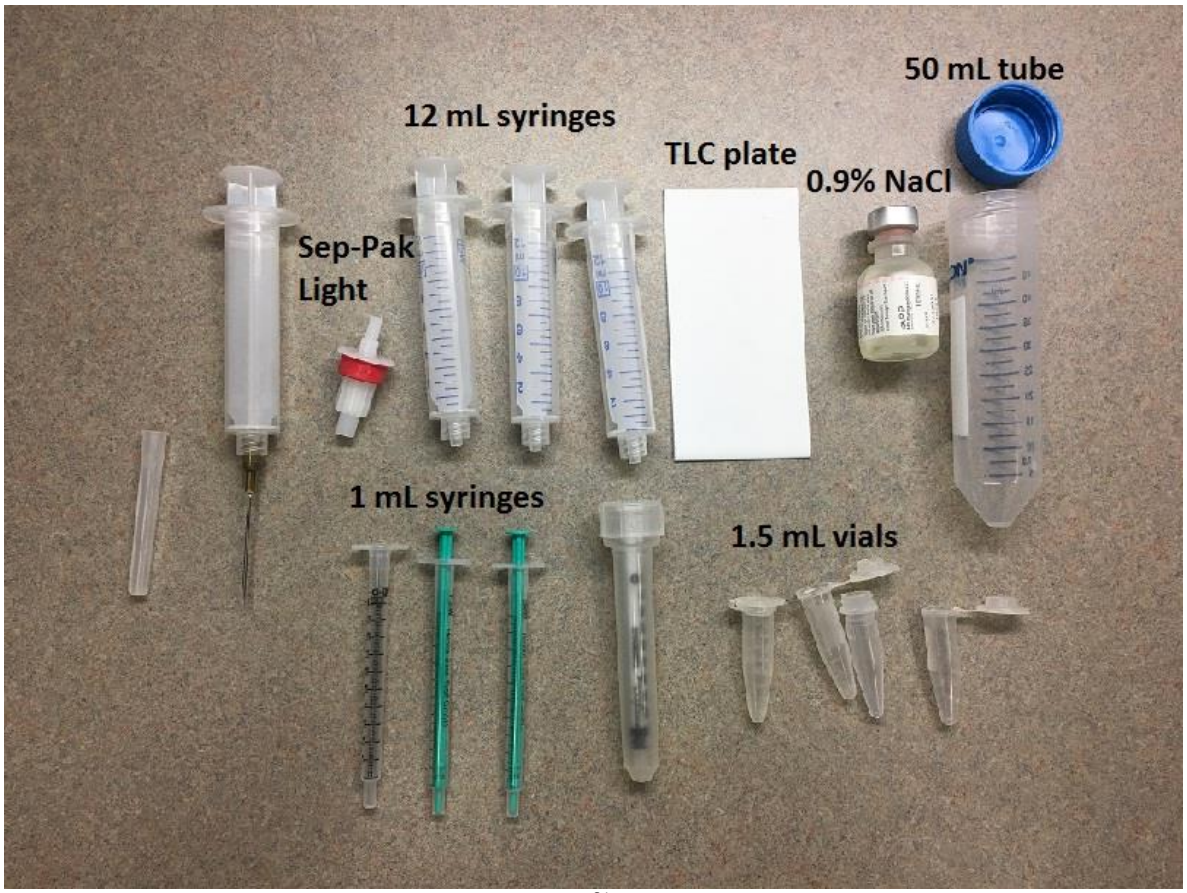

Figure 5 Demonstration of the materials for preparing ^{64}Cu-ATSM pre-clinical doses.

2.5.2 Preparation of ^{64}Cu-ATSM doses for clinical studies

Preparing ^{64}Cu-ATSM compounds for patient studies was more rigorous than for animal studies. During all procedures, personnel must follow all good manufacturing practice (GMP) rules in addition to all radiation safety procedures at the drug compounding site: lab coats, eye protection and disposable protective shoe covers were needed; sleeve protectors and two pairs of disposable gloves must be worn; all personnel must wear TLD radiation badges and rings.

I. Drug Compounding Environment

For ATSM preparation, drug compounding took place in an ISO Class 5 environment and involved aseptic processing. Principles of ALARA were observed for all aspects of drug compounding.

II. Supplies and Equipment

Supplies used to produce ATSM included lyophilized ATSM ligand (50-mL vial from PTI, Inc.), ATSM reconstitution solution (10-mL vial from PTI, Inc.), $^{64}CuCl_2$ in 0.1 M HCl (10-mL evacuated vial), radiation shield for vial of $^{64}CuCl_2$ solution, and 6" extension tube (Fig. 6A).

Additional supplies were three 0.22-µm Millex-GV sterile filters, two 10-mL Luer-Lok syringes, one 60-mL Luer-Lok syringe, five 21-gauge needles, one 19-gauge 3 ½-inch spinal needle, one 33" extension tube, one 10-mL sterile evacuated vial, six sterile 70% isopropyl alcohol pads (Fig. 6B).

The equipment required were freezer for storage of Lyophilized ATSM kit, refrigerator for storage of reconstitution solution, tongs, dose calibrator, vortex mixer, and radiation shield for final product vial.

III. Procedures of ^{64}Cu-ATSM synthesis

First, we reconstituted the ATSM ligand in the lyophilized ATSM vial and the reconstitution solution. Second, ATSM was radio-labelled with $^{64}CuCl_2$. Then, we placed a 10-mL sterile empty vial into a radiation shield to prepare the product vial, and prepare and insert two 21-gauge needle-Millex GV filter assemblies into the septum of the Product Vial as depicted (one high, one low) (Fig. 6C). We attached a 33" extension tube to the upper needle-filter assembly on the product vial, attached a 60-mL syringe to the 33" tube, and attached a 6" extension tube to the lower. We inserted the spinal needle as well as the vent filter into reaction vial (Fig. 6D).

The last step was sterile filtration of drug product. We slowly drew back on the 60-mL syringe connected to the 33" extension tube; the reaction solution was pulled through the sterilizing filter

into the product vial (Fig. 6E). Complete fluid transfer from the Reaction Vial was visually checked. When the fluid transfer was complete, we withdrew the needle-filter assemblies from the product vial.

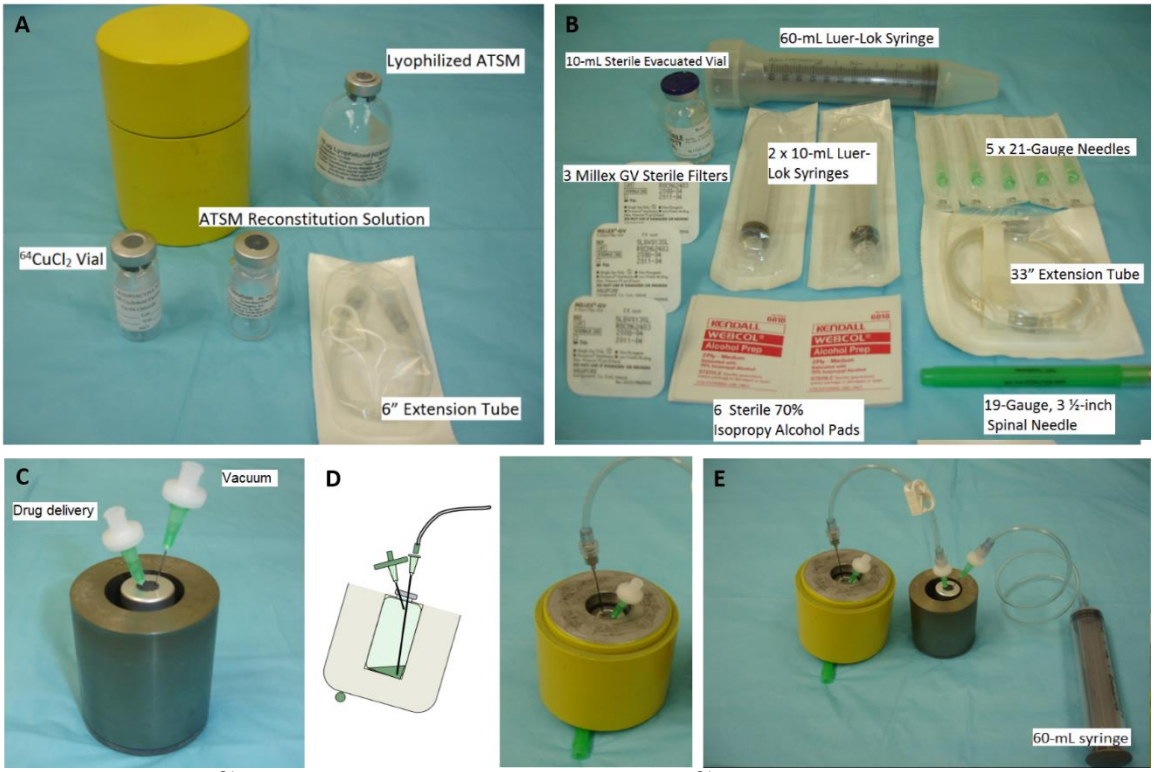

Figure 6 Preparation of ^{64}Cu-ATSM patient doses. A). Supplies for ^{64}Cu-ATSM synthesis; B). Additional supplies for ^{64}Cu-ATSM synthesis; C). Preparation of product vial; D). Preparation of reaction vial; E). Sterile filtration of drug product. (Courtesy of Tom Voller, WUSM)

IV. Membrane Integrity Test

After the ATSM preparation, the Millex-GV Sterilizing Filter was removed from the 6" tube to perform membrane integrity testing according to institutional procedures. The membrane must pass integrity testing for drug product release. We documented the results of radiopharmaceutical compounding on the trial-specific batch record form (BR Form).

V. Radiochemical Purity Test

The Oasis cartridge was used for radiochemical purity test. When the ^{64}Cu-ATSM sample and Oasis cartridge were prepared, the sample was loaded onto the cartridge, rinsed on cartridge with 1 ml of 0.9% NaCl two times, and eluted by washing the cartridge with 1 ml of absolute ethanol three times (Fig. 7). Lastly, the cartridge was removed for assay. Radiochemical Purity (RCP) was

then calculated. The RCP must be > 95%, and the results of radiopharmaceutical purity testing was documented on the trial-specific batch record.

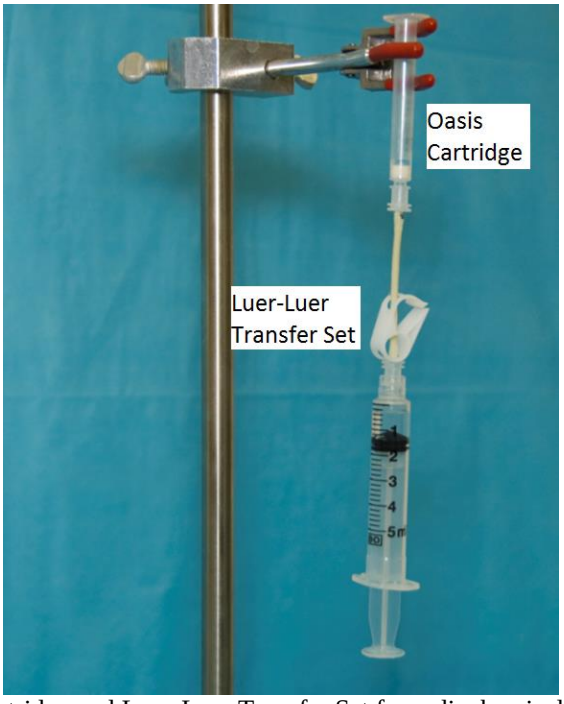

Figure 7 Setting up of Oasis Cartridge and Luer-Luer Transfer Set for radiochemical purity (RCP) test. (Courtesy of Tom Voller, WUSM)

Chapter 3: Evaluating the capability of ^{64}Cu-ATSM PET imaging for determining hypoxia in atherosclerotic plaque

3.1 ^{64}Cu-ATSM small animal PET imaging of hypoxic atherosclerosis in an ApoE$^{-/-}$ mouse model

This research was originally published as "Imaging of hypoxia in mouse atherosclerotic plaques with ^{64}Cu-ATSM" in Nuclear Medicine and Biology (*106*). Copyright (2016) by Elsevier Inc.

3.1.1 ^{64}Cu-ATSM mouse study: introduction

In this study, we assessed the feasibility of imaging the development of hypoxia in an apolipoprotein E knockout (ApoE KO or ApoE$^{-/-}$) mouse model of atherosclerosis using the PET imaging agent ^{64}Cu-ATSM. Lack of ApoE results in severe hypercholesterolemia and spontaneously developed atherosclerotic lesions. This mouse model was widely used to study atherosclerosis (*107*, *108*), therefore we investigated the feasibility of ^{64}Cu-ATSM for the identification of hypoxic and potentially unstable atherosclerotic plaque with this mouse model. We used the hypoxia-specific dye pimonidazole and the pan macrophage marker CD68 to assess for co-localization of hypoxia in macrophages. Pimonidazole is reduced in cells with low oxygen tension to form protein adducts that can be detected by immunostaining (*24*). We hypothesized that there would be high PET image contrast between hypoxic and normoxic tissues after the administration of ^{64}Cu-ATSM, and that the presence of hypoxia by ^{64}Cu-ATSM uptake would correlate with pimonidazole uptake within the *ex vivo* atherosclerotic arch specimens. We also hypothesized that pimonidazole uptake would co-localize to macrophages (CD68) on immunohistochemistry (IHC).

3.1.2 ^{64}Cu-ATSM mouse study: materials and methods

I. General

All animal studies were performed under a protocol approved by the Animal Studies Committee at our institution. Ten-month-old wild type (C57Bl/6, n=7) mice weighting ~30g were purchased from Charles River Laboratories (Wilmington, MA) and fed standard-chow diet (SCD). One-year-old ApoE$^{-/-}$ mice (n=9) spontaneously expressing atherosclerosis were fed SCD for one year and had roughly the same weight as the wild type mice prior to ^{64}Cu-ATSM PET imaging. A subset of ApoE$^{-/-}$ mice (n = 4) and wild type mice (n = 4) also underwent ^{18}F-FDG PET imaging in addition to ^{64}Cu-ATSM PET imaging one day later. Additional SCD wild type mice (n = 6) and ApoE$^{-/-}$ mice fed either with SCD (n = 6) or a high-fat Western type diet (n = 6; HFD, containing 21.2% fat and 0.2% cholesterol; Harlan Laboratories, Inc., Indianapolis, IN) underwent longitudinal imaging. These mice underwent PET imaging in 2-month intervals for a total of 10 months. This was done in order to assess the uptake of ^{64}Cu-ATSM at various stages of plaque development. The experimental arms are given below in Table 1. All chemicals, unless otherwise stated, were purchased from Sigma-Aldrich Chemical Co. (St. Louis, MO). Water was distilled and then deionized (18 MΩ/cm^2) by passing through a Milli-Q water filtration system (Millipore Corp., Milford, MA).

Copper-64 ATSM doses was prepared as previously described (see section 2.4.2.1).

Table 1 Experimental cohorts.

Preliminary Mouse Study (N = 16)			
Number of Mice	Species/Diet	Age of Imaging	Radiopharmaceuticals
4	ApoE-/-, SCD	54 -62 (day 1)	^{18}F-FDG
9	ApoE-/-, SCD	54 -62 (day 2)	^{64}Cu-ATSM
4	C57Bl/6, SCD	43 (day 1)	^{18}F-FDG
7	C57Bl/6, SCD	43 (day 2)	^{64}Cu-ATSM
Longitudinal Mouse Study (N = 18)			
6	ApoE-/-, HFD	14, 23, 32, 41	^{64}Cu-ATSM
6	ApoE-/-, SCD	14, 23, 32, 41	^{64}Cu-ATSM
6	C57Bl/6, SCD	14, 23, 32, 41	^{64}Cu-ATSM

II. Dynamic Small Animal PET Imaging

Small animal imaging studies were carried out on a Siemens Inveon (Siemens Medical Solutions USA, Inc., Malvern, PA) or Focus 220 microPET scanner (Concorde MicroSystem Inc., Knoxville, TN). Isoflurane (1-2%) was used to induce and maintain anesthesia during imaging. Each animal received ~3.7 MBq of activity in 100 µL saline via lateral tail-vein injection. Mice were imaged in pairs in a supine position in a specially designed bed. Imaging was performed using 0-30 minute dynamic scan sessions for ^{64}Cu-ATSM or 0-60 minute dynamic scan sessions for ^{18}F-FDG. PET data was reconstructed using standard methods with the maximum *a posteriori* probability (MAP) algorithm. ^{64}Cu-ATSM images were reconstructed in 10 second intervals up to 2 minutes, 30 seconds intervals up to 5 minutes, and 5 minute intervals up to 30 minutes. ^{18}F-FDG scans were reconstructed in 2-5 seconds intervals up to 1 minute p.i., 10-30 seconds intervals up to 4 minutes p.i., 60-120 second intervals up to 10 minutes p.i. and 5 minute intervals up 1 hour.

CT was performed prior to each PET study for attenuation correction and anatomical co-localization of the PET data.

III. Image Analysis

Images were evaluated by measuring the radioactivity concentration of the aortic arch and non-target (thigh muscle) of each mouse on the co-registered PET/CT images using the Inveon Research Workplace (IRW; Siemens Medical Solutions USA, Inc., Malvern, PA).

Regions of interest (ROIs) were drawn around the entire aortic arch (~15 mm^3) or a region of ~50 mm^3 on the thigh muscle on multiple consecutive, transaxial image slices. Time activity curves (TACs) in kBq/cm^3 were generated by plotting the ROI values over time.

Standardized Uptake Values (SUVs) were calculated by dividing the decay-corrected activity per unit volume of tissue (Bq/cm^3) by the injected activity per unit of body weight (Bq/g), as described by the following equation:

$$\mathrm{SUV} = \frac{\text{radioactivity concentration } \left(\frac{Bq}{cm^3}\right)}{\text{injected dose}\frac{Bq}{\text{body}}\text{weight } (g)}. \quad (1)$$

The aortic arch-to-leg muscle (A/M) SUV ratios were calculated and compared.

III. Statistical Methods

Graph generation and statistical analysis were performed using GraphPad Prism version 6 (GraphPad Software Inc., La Jolla, CA). Differences between groups were evaluated by Student's *t*-test (two groups) or one-way ANOVA (three or more groups) using *Fisher's least significant difference* method for post-hoc test. Data were reported as mean ± S.E.M. (standard error of mean)

unless otherwise indicated and differences at the 95% confidence level ($P < 0.05$) were considered statistically significant.

IV. Immunohistochemistry

4 mice from each subset (wild type, ApoE$^{-/-}$ fed SCD or HDF) were sacrificed to collect *ex vivo* endarterectomy specimens for histopathological assessment and pimonidazole immunohistochemistry. The animals were injected with the hypoxia-reactive reagent PIMO hydrochloride (Hypoxyprobe^{TM}-1 Kit, Hypoxyprobe, Inc, Belmont, MA) 60-90 minutes before euthanasia. Specimens were embedded in paraffin and sectioned transversely. Serial 5 μm sections of even intervals were placed on slides for immunohistochemistry and histology with hemotoxylin and eosin (H&E) stains. Aortic arch specimens and leg muscle tissue specimens were stained for the presence of hypoxia using an antipimonidazole antibody (Natural Pharmacia Inc., Belmont, MA) and mounted in solution containing 4'-6-diamidino-2-phenylindole (Vector Laboratories, Palo Alto, CA). Although PIMO may react with reactive oxygen species (*109*), the antipimonidazole antibody only recognizes hypoxia derivatives (*8*).

Rat anti mouse CD68 antibody (AbD Serotec, Bio-Rad Laboratories, Hercules, CA) which recognizes mouse macrosialin for the identification of CD68 was used to stain atherosclerosis-associated macrophages (*110-115*) in the paraffin-embedded aortic arch of mouse, and the result was co-localized to the PIMO staining. Fluorescein isothiocyanate (*116*) and Cy3 fluorescent labeled antibodies were used as the secondary fluorescent antibodies, respectively. The slides were incubated with DAPI (4, 6-diamino-2-phenylindole) (Fluoro-Gel II with DAPI, electron microscopy sciences, Inc., Hatfield, MA) to show cell nuclei. Negative control staining was performed by replacing the primary antibody with matching isotype control followed by same

fluorescent labeled secondary antibody. IHC slides were imaged by Leica TCS SP5 confocal laser scanning microscope (Leica Microsystems Inc., Buffalo Grove, IL).

V. Autoradiography

Specimens from 4 SCD ApoE$^{-/-}$ mice and 4 wild-type control mice were collected for autoradiography. The animals were injected with pimonidazole hydrochloride 60-90 minutes before euthanasia. Harvested fresh tissues of aortic arch (with heart attached) were fixed in 4% Paraformaldehyde (PFA) for ~12 hours and cut transversely into a series of adjacent sections on a cryostat (Leica) at 20 μm thickness and attached to adhesive glass slides (CFSA 1X, Leica Microystems, Buffalo Grove, IL). Both the aortic arch of the control mice and the heart of the same ApoE$^{-/-}$ mice were used as negative controls. The slides used for autoradiography were covered by adhesive tape (CryoJane Tape Transfer System®, Leica Microsystems, GmbH, Nussloch, Germany) and exposed to a phosphor imaging plate (GE Healthcare Life Sciences, Pittsburgh, PA) for 12 hours at -20^{o}C, and the plates were scanned using phosphor imager plate scanner (Storm® 840, Amersham Biosciences Corp., Piscataway, NJ). The resulting images were processed using ImageQuant 5.2 (Molecular Dynamics, Inc, Sunnyvale, CA) and ImageJ (v1.48, public domain) software. After decaying for at least 3 days, the adjacent slides were treated with pimonidazole and CD68 staining for the presence of hypoxia and macrophages. Due to the different resolution of the immunohistochemistry image obtained from the confocal microscopy (< 5μm) and the autoradiograph obtained from the plate scanner (50 μm), the autoradiographs were scaled up 11.2 times with bilinear interpolation to match the size of the IHC images in the same ROI for comparison.

3.1.3 ^{64}Cu-ATSM mouse study: results

^{64}Cu-ATSM was distributed rapidly in the blood pool and quickly excreted; thus activity was found in the kidney and liver at all time-points post injection likely due to clearance. The leg muscle is not hypoxic under normal conditions and therefore was used for comparison with aortic arch. A strikingly different uptake pattern was observed between muscle and aortic arch. ROIs were drawn on the PET and CT co-registered images over the aortic arch and an area of leg muscle on each mouse after administration of ^{64}Cu-ATSM or ^{18}F-FDG (Fig. 8).

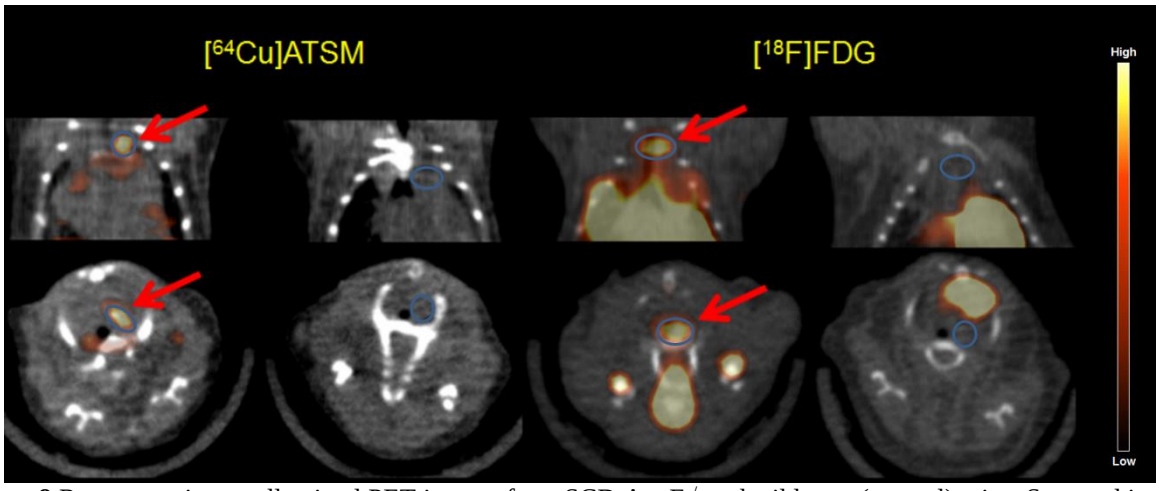

Figure 8 Representative small animal PET images from SCD ApoE$^{-/-}$ and wild type (control) mice. Summed images of coronal (top) and transverse (bottom) slices 7.5-30 minutes post injection (p.i.) of ^{64}Cu-ATSM (left) and 40-60 minutes p.i. of ^{18}F-FDG (right) with ROIs of aortic arch (in blue circles) drawn on each mouse.

7.5 minutes post injection of ^{64}Cu-ATSM, the radioactivity in the aortic arch and leg muscle was stable (Figure 9A), while the difference in time activity curves (TACs) of aortic arch between the SCD ApoE$^{-/-}$ mice and control mice increased over time from 15 minutes post injection of ^{18}F-FDG until the end of imaging (Figure 9B). There was no significant difference in activity in leg muscle (background) (Figure 9, A and B). The average SUVs of the aortic arch 7.5-30 minutes post injection of ^{64}Cu-ATSM were significantly higher in the SCD ApoE$^{-/-}$ mice (n = 9) than the wild type mice (n = 7): 7.80 ± 0.41 and 5.45 ± 0.52, respectively (p = 0.004), as were average aortic arch to muscle (A/M) SUV ratios of the SCD ApoE$^{-/-}$ mice and the wild type mice: 5.66 ±

0.23 and 3.87 ± 0.22, respectively ($p < 0.0001$) (Figures 10A). For the mice injected with ^{18}F-FDG, the A/M SUV ratios between SCD ApoE$^{-/-}$ mice and control mice became statistically significant at about 40 minutes post injection of ^{18}F-FDG (Figure 10B). The 40-60 minutes p.i. average A/M SUV ratio difference between SCD ApoE$^{-/-}$ mice (n = 4, 8.07 ± 0.96) and control mice (n = 4, 4.55 ± 0.21) after ^{18}F-FDG injection (Figure 11) was also significant ($p < 0.005$), as was the average A/M SUV ratio difference (5.57 ± 0.38 V.S. 3.67 ± 0.61) 7.5-30 minutes after ^{64}Cu-ATSM for the same subset of mice.

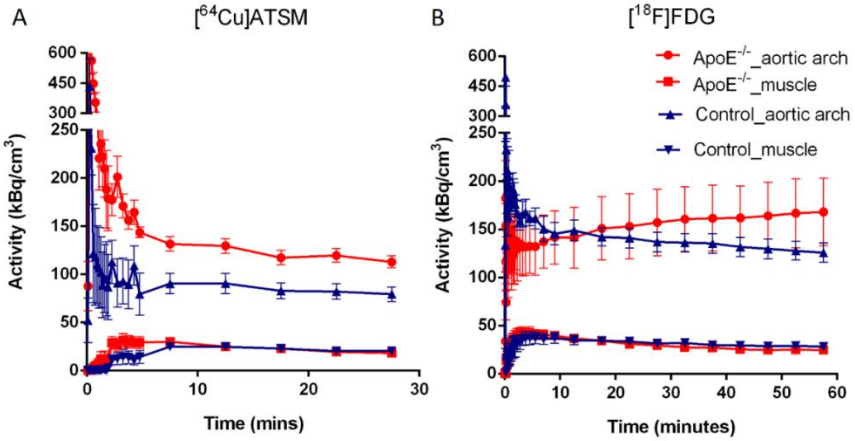

Figure 9 Time activity curves (TACs) of ^{64}Cu-ATSM **(A)** and ^{18}F-FDG **(B)** show increased difference in aortic arch activity between the SCD ApoE$^{-/-}$ and wild type mice injected with ^{64}Cu-ATSM in comparison to ^{18}F-FDG injection. Results are presented as mean ± S.E.M. in the graph. The numbers of ApoE$^{-/-}$ and control mice were 9 and 7 for ^{64}Cu-ATSM imaging, and 4 and 4 for ^{18}F-FDG imaging, respectively.

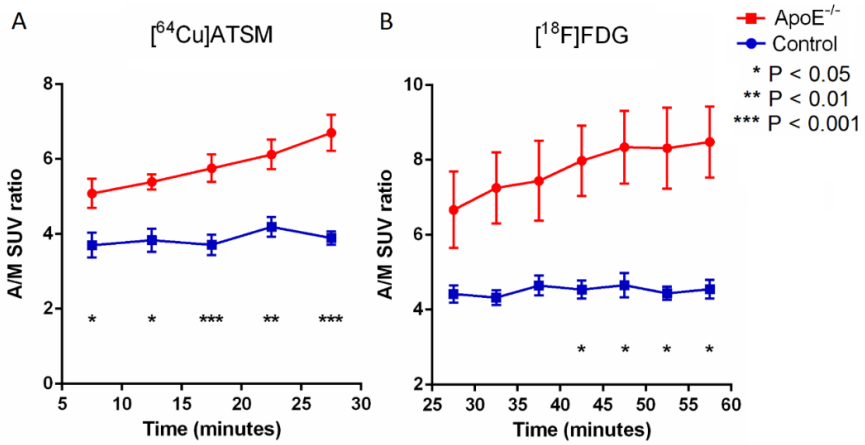

Figure 10 A/M SUV ratios observed with small animal PET imaging after injection of ^{64}Cu-ATSM (A) and ^{18}F-FDG (B) in SCD ApoE$^{-/-}$ mice and control mice. ^{64}Cu-ATSM injection yields significant difference in the ratios at a faster rate in comparison to ^{18}F-FDG injection, which increases over time from 7.5 minutes p.i. to the end of imaging. Results are presented as mean ± S.E.M. in the graph. The numbers of ApoE$^{-/-}$ and control mice were 9 and 7 for ^{64}Cu-ATSM imaging, and 4 and 4 for ^{18}F-FDG imaging, respectively.

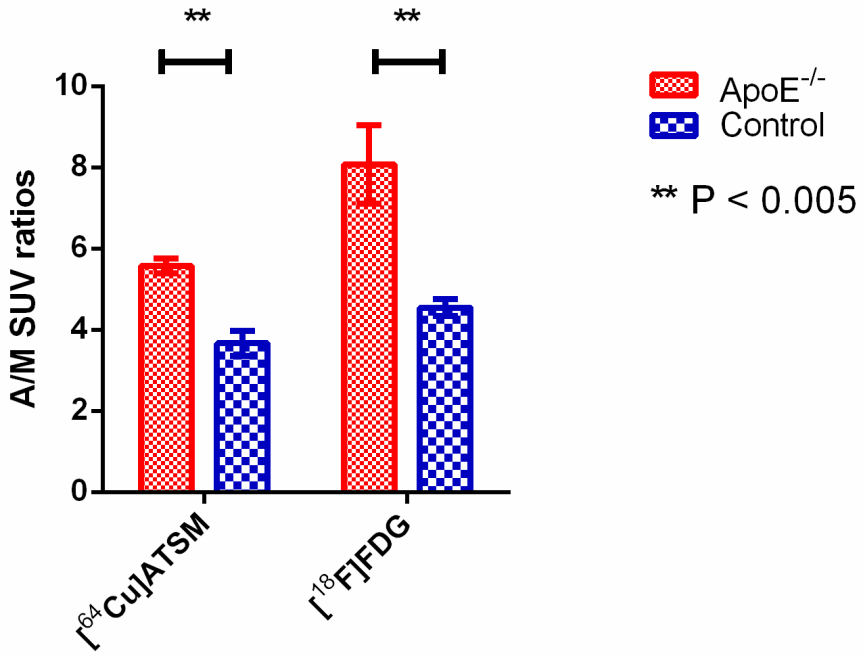

Figure 11 Comparison of A/M SUV ratios ± S.E.M. for the same subset of SCD ApoE$^{-/-}$ mice (n = 4) and control mice (n = 4) 7.5 - 30 minutes p.i. of ^{64}Cu-ATSM and 40- 60 minutes p.i. of ^{18}F-FDG. Significant differences were observed between ApoE$^{-/-}$ mice and control mice for both ^{64}Cu-ATSM and ^{18}F-FDG imaging.

IHC of the aortic arch in ApoE$^{-/-}$ mice showed the presence of atherosclerosis whereas IHC of the aortic arch of wild type mice did not. PIMO uptake was found in the aortic arch of both SCD and HFD ApoE$^{-/-}$ mice (Fig. 12, Fig. 13). There was large overlap of the fluorescent areas corresponding to the CD68 macrophage staining co-localized to the PIMO adducts, demonstrating co-localization of hypoxia to macrophages (Fig. 12, Fig. 13). Wild type aortic specimens did not demonstrate hypoxia by PIMO staining (Fig. 14). The DAPI staining for nuclei delineated and confirmed the cellular components of the plaques imaged.

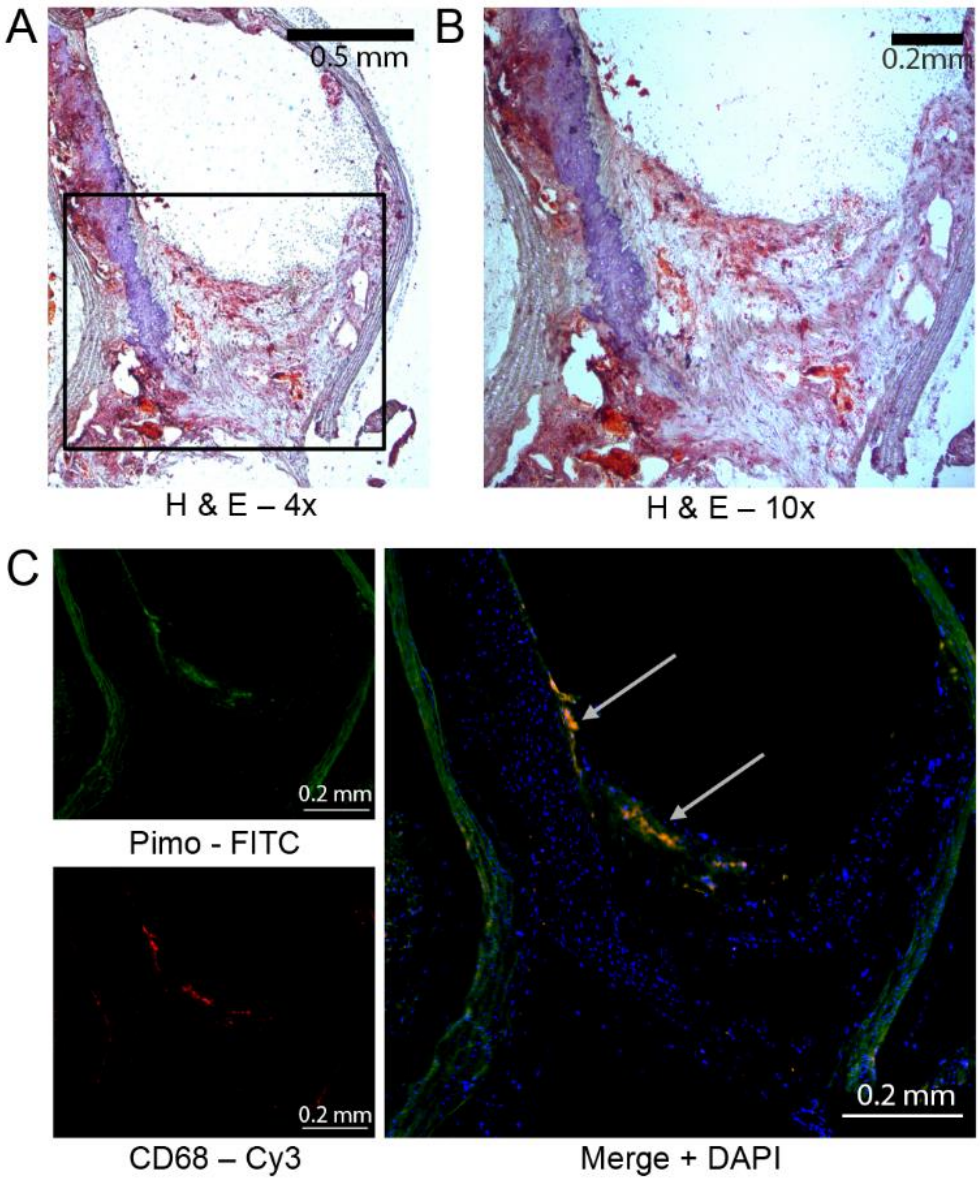

Figure 12 Detection of PIMO adducts co-localizes with macrophages within atherosclerotic plaque of aortic arch. Aorta were harvested from 40 week old ApoE$^{-/-}$ mouse on western diet for 33 week that received PIMO 2 hours prior to sacrifice. (A) Representative image of H&E stained section from aortic arch. (B) Magnification of region of interest from (A). (C) Immunofluorescence image from serial section of aortic arch shown in (A). Green is mAb 4.3.11.3 staining pimodiazole adducts (internal elastic lamina is autofluorescent), red is CD68 staining for macrophages, blue is DAPI nuclear stain, and yellow is the overlay of PIMO and CD-68. Representative of at least three animals.

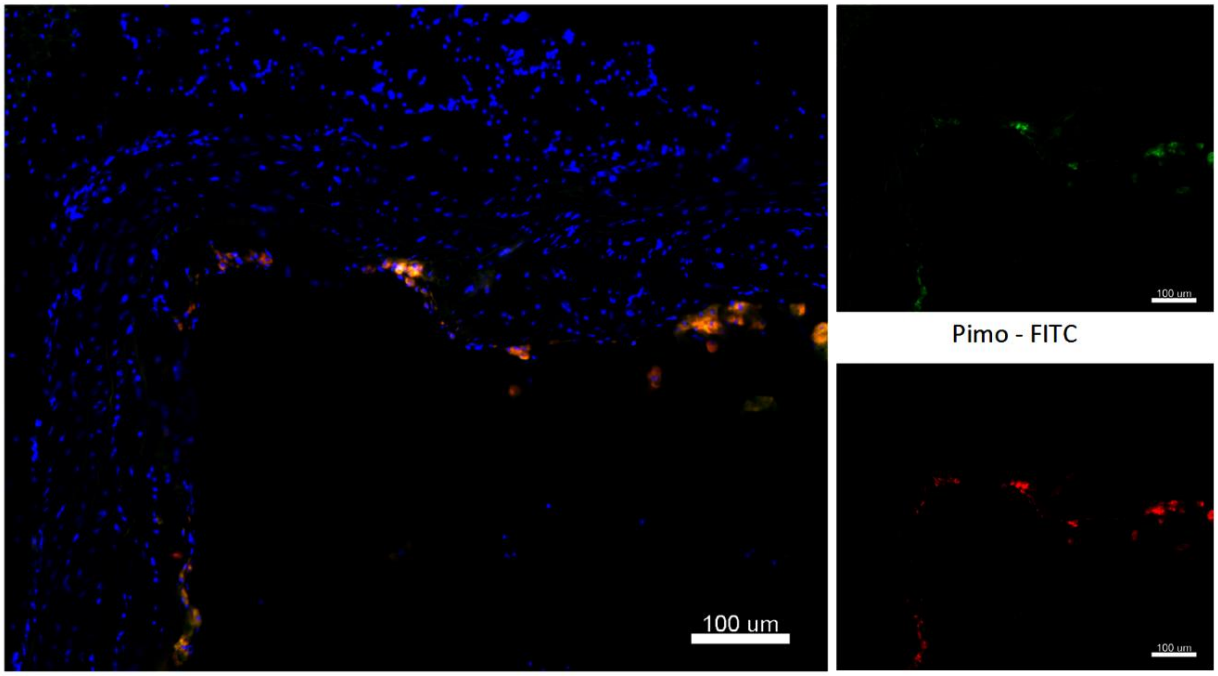

Figure 13 Immunofluorescence images from serial sections of aortic arch in 10 months ApoE$^{-/-}$ mouse on standard chow diet that received PIMO 2 hours prior to sacrifice. PIMO adducts were colocalized of with macrophages (CD68) within atherosclerotic plaque of aortic arch. Green is mAb 4.3.11.3 staining PIMO adducts (internal elastic lamina is autofluorescent), red is CD68 staining for macrophages, blue is DAPI nuclear stain. Scale bar = 100 µm. Representative of at least three animals.

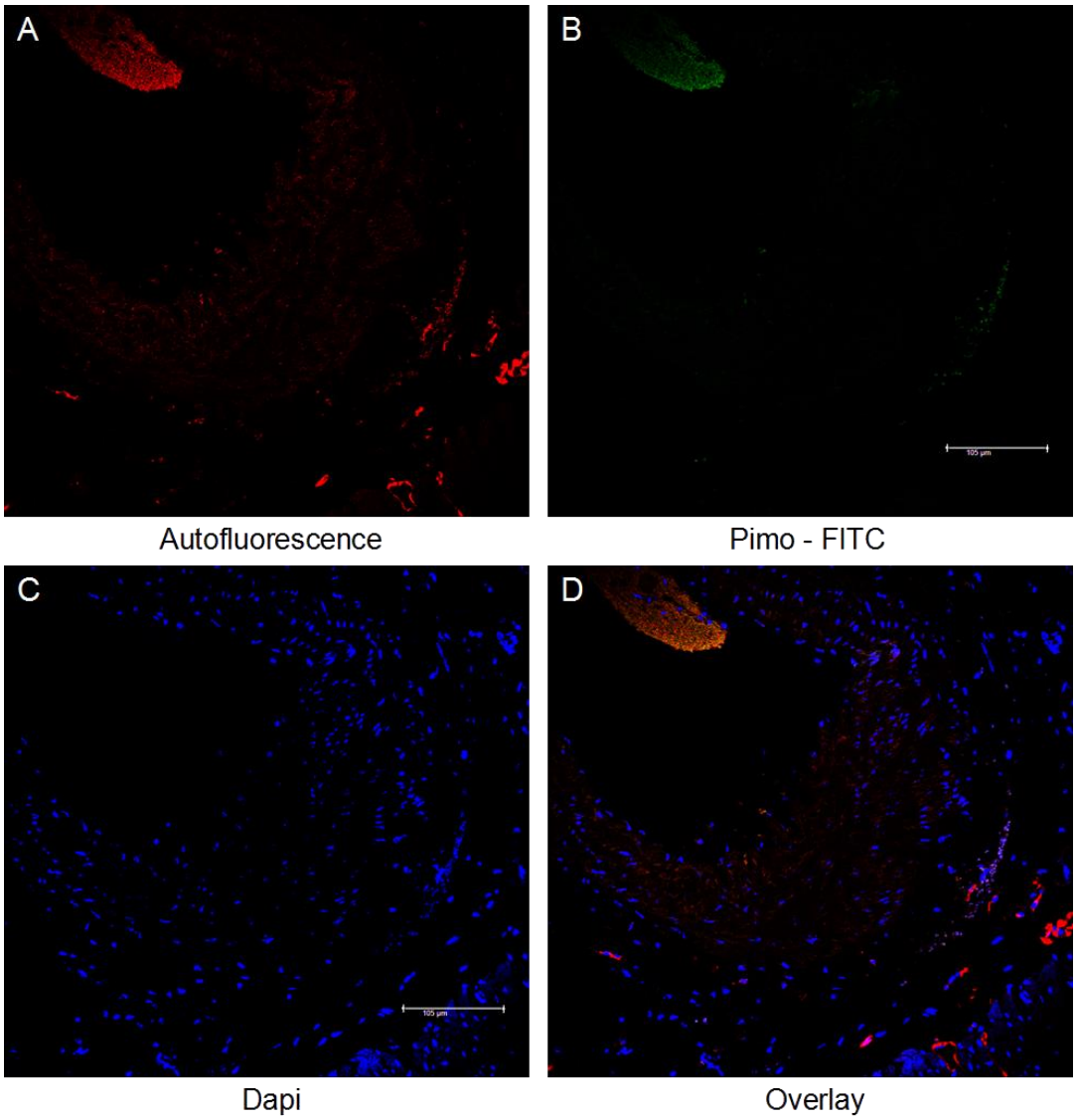

Figure 14 Confocal laser-scanning microscopy images of the aorta harvested from 10 months old SCD wild-type mouse that received PIMO 2 hours prior to sacrifice. No remarkable ^{64}Cu-ATSM uptake was measured in microPET images in the aortic arch of this mouse, which is consistent with the IHC staining that no PIMO signal was detected in this region. **(A)** Representative image of autofluorescence from aortic arch (red). **(B)** PIMO adducts stained with mAb 4.3.11.3 (green); internal elastic lamina is autofluorescent **(C)** Nuclei stained with DAPI (blue) (A). Overlay of autofluorescence, PIMO staining and DAPI staining (*117*). Scale bar = 105 µm. Representative of at least three animals.

Autoradiographs from different transverse slides confirmed that SCD ApoE$^{-/-}$ mice had higher uptake of ^{64}Cu-ATSM in comparison to the aortic arch of control mice as well as the heart of the same ApoE$^{-/-}$ mice (Fig. 15A). The hot spots in the scaled-up autoradiograph (Fig. 15B) regionally co-localized to the IHC image of the adjacent slide (Fig. 15, C-E).

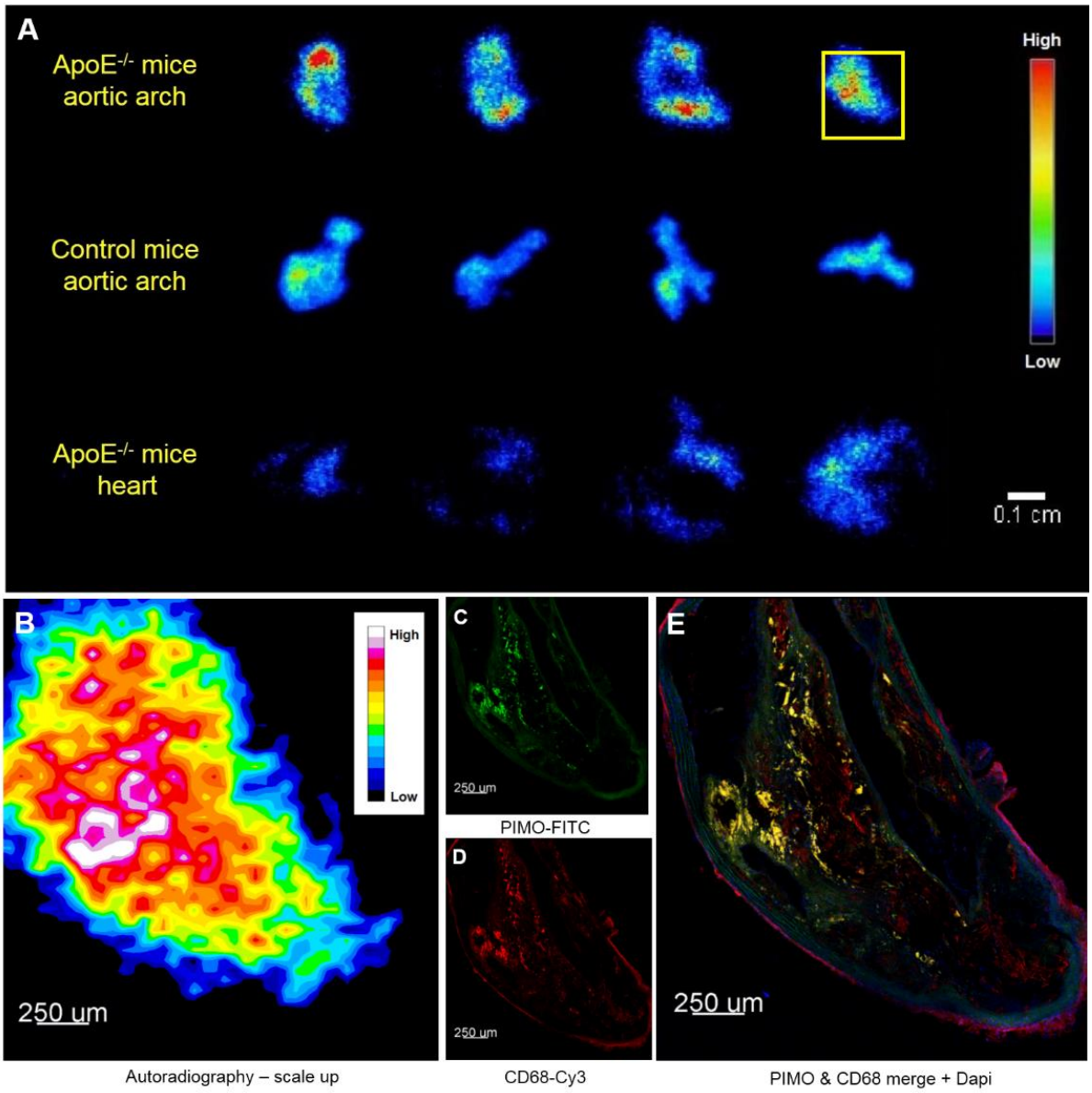

Figure 15 (A) Representative autoradiographs obtained from transverse slices of the aortic arch in SCD ApoE$^{-/-}$ mice (top) and control mice (middle) and heart in SCD ApoE$^{-/-}$ mice (bottom) 30 minutes p.i. of ^{64}Cu-ATSM. (B) The section in the yellow square in (A) were scaled-up 11.2 times with bilinear interpolation. The bright spots in scaled-up autoradiograph were co-localized in shape to the (C) PIMO and (D) CD-68 strongly-positive area and their merged area. Green is mAb 4.3.11.3 staining for PIMO adducts (internal elastic lamina is autofluorescent), red is CD68 staining for macrophages, blue is DAPI nuclear stain, and yellow is the overlay of PIMO and CD68.

The results of our longitudinal studies comparing ^{64}Cu-ATSM uptake in SCD and HFD ApoE$^{-/-}$ mice at various time points suggested that both groups of mice developed hypoxic atherosclerosis longitudinally over time. There was no significant difference in A/M SUV ratios between the three

groups of mice at 14 weeks old, suggesting that no advanced atherosclerosis had been developed in the ApoE$^{-/-}$ mice at that age. However, ^{64}Cu-ATSM uptake in the both SCD and HFD fed ApoE$^{-/-}$ mice increased significantly from 14 to 23 weeks ($p < 0.05$, Fig. 16) with both SCD and HFD ApoE$^{-/-}$ mice showing significantly higher A/M SUV ratios at 23 weeks ($p < 0.01$) in comparison to the wild-type control mice fed with standard chow. The difference between SCD and HFD ApoE$^{-/-}$ mice progressively increased over time until 32 weeks old and began to decrease until end of the study (41 weeks old). Although HFD ApoE$^{-/-}$ mice always had higher A/M SUV ratios than the SCD ApoE$^{-/-}$ mice, this difference was only statistically significant at 32 weeks.

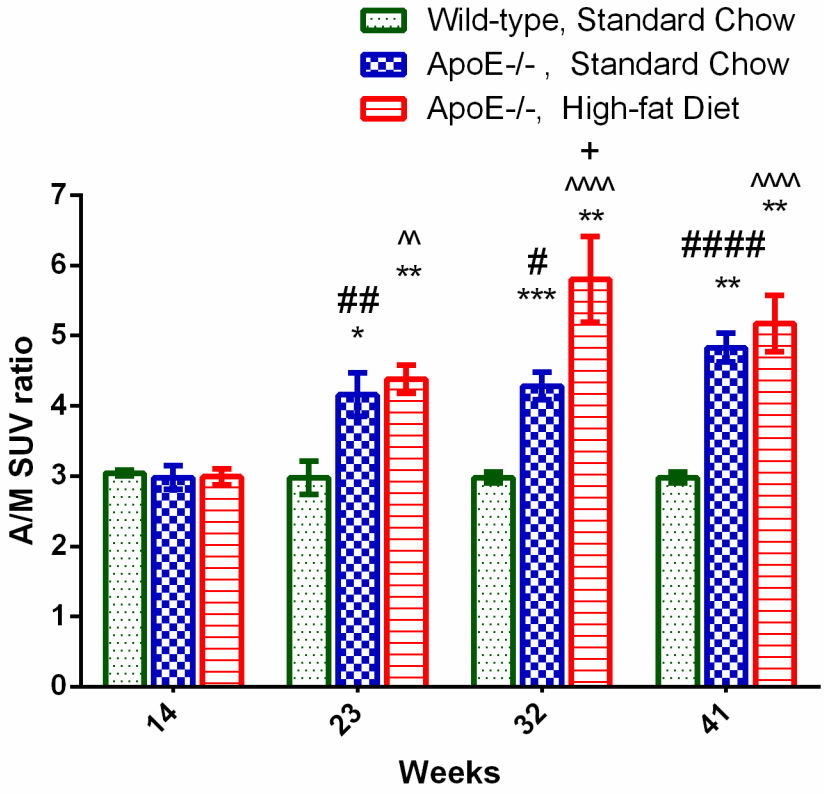

Figure 16 Longitudinal study of ^{64}Cu-ATSM uptake in ApoE$^{-/-}$ mice at the same age fed either with SCD or HFD. ^{64}Cu-ATSM uptakes were assessed by A/M SUV ratios as mean ± S.E.M of n = 6. $^{*}p < 0.01$, $^{**}p < 0.001$, and $^{***}p < 0.001$ are groups vs. 14 weeks groups. $^{\#}p < 0.05$, $^{\#\#}p < 0.01$ and $^{\#\#\#\#}p < 0.0001$ are SCD ApoE$^{-/-}$ groups vs. SCD wild-type groups at the same age. $^{\wedge\wedge}p < 0.01$ and $^{\wedge\wedge\wedge\wedge}p < 0.0001$ are HFD ApoE$^{-/-}$ groups vs. SCD wild-type groups at the same age. $^{+}p < 0.05$ is HFD ApoE$^{-/-}$ group vs. SCD ApoE$^{-/-}$ group at the same age. The numbers of ApoE$^{-/-}$ HFD, ApoE$^{-/-}$ SCD and wild-type SCD mice were all 6.

3.1.4 ^{64}Cu-ATSM mouse study: discussion

This study demonstrated the utility of ^{64}Cu-ATSM for imaging hypoxia in atherosclerotic plaque in an ApoE$^{-/-}$ mouse model, permitting image contrast between hypoxic and normoxic tissues 7.5-30 minutes post injection. The longitudinal study investigating the role of diet and age in this mouse model suggested that ^{64}Cu-ATSM imaging may assist in evaluating the progression of hypoxia over time and formed the basis of our future preclinical and clinical studies.

It is well established that macrophages play a key role in atherosclerosis (*118*). In the initial stages of atherogenesis, modified lipoproteins recruit monocytes and T cells into macrophages and internalize the modified lipoproteins, resulting in the accumulation of highly oxygen-consuming lipid-loaded macrophages (foam cells) in developing lesions before apoptosis (*49*). The present of plaque hypoxia in macrophage-rich areas with neovascularization has been demonstrated in rabbit advanced atherosclerosis (*119*). Despite relatively low resolution for autoradiography, the brightest area in the autoradiograph, which indicated the highest ^{64}Cu-ATSM uptake, regionally correlated to the PIMO and CD68 positive areas, the elevated ^{64}Cu-ATSM was accumulated in the hypoxic macrophage-rich core of the atherosclerotic plaques in the aortic arch of ApoE$^{-/-}$ mouse. ^{64}Cu-ATSM has time-dependent and cell-dependent spatial distribution and retention kinetics, which result in various correlation between the uptake of Cu-ATSM and immunofluorescent markers of hypoxia in different tumor cell lines (*18-23*). There are reports of mildly (pO_2 < 2% O_2) (*120*) and severely hypoxic retention threshold (2.0-5.0 mmHg and even lower (*121*); 0.5% and 0.1% O_2 (*12*); versus 40-60 mmHg in normal tissue (*122*)) of ^{64}Cu-ATSM in different tumor types and acquisition time after injection. In a recent review article by Colombié *et al.* (*123*), the authors attribute the low correlation between Cu-ATSM uptake and hypoxic distribution in some tumors to the differing redox status of them. These tumor types might have a lower than average

redox potential with high concentrations of electron donors leading to reduction and trapping of Cu-ATSM in both hypoxic and normoxic areas, i.e. human prostate tumor which overexpresses the fatty acid synthase (FAS) because this enzyme requires a large amount reductive species (NADPH) as cofactor for function (*123, 124*). In atherosclerosis, although the redox potential caused by ATP-consumption in the lipid-loaded macrophages does not tend to be unusually low, we are still uncertain about the exact oxygen retention threshold of ^{64}Cu-ATSM in hypoxic plaque. It be either higher or lower than pimonidazole ($pO_2 \leq 10$mm Hg), resulting in smaller or larger spatial distribution of ^{64}Cu-ATSM than PIMO.

Although ^{18}F-FDG has been a well-described agent for in vivo imaging of atherosclerosis in animal (*115, 125*) and human subjects (*15*) and there is strong experimental and clinical evidence supporting that the increased ^{18}F-FDG uptake in atherosclerotic plaque is associated with the abundance of macrophages, it is a relatively non-specific tracer with many practical limitations (*126*) because it provides complementary information on metabolic function as opposed to hypoxia. ^{18}F-FDG vascular uptake can also present in vascular smooth muscle cells and endothelial cells (*72, 127*). Moreover, because of the long time course of ^{18}F-FDG in arteries, a longer ^{18}F-FDG circulation time is always required for vascular ^{18}F-FDG PET imaging protocol, preferably at least 90 minutes (*128*). One other hand, the rapid blood pool clearance of ^{64}Cu-ATSM allowed PET imaging within 30 min of tracer injection, a significant advance over ^{18}F-FDG. Our finding that the SUV and A/M SUV ratios between HFD and SCD ApoE$^{-/-}$ with ^{64}Cu-ATSM imaging differ from a previous study using ^{18}F-FDG as the PET imaging agent where ApoE$^{-/-}$ mice receiving SCD had stable and low ^{18}F-FDG SUVs while the ApoE$^{-/-}$ mice receiving HFD showed progressively higher ^{18}F-FDG uptake up to the end of their study at 32 weeks (*115*). This difference may be secondary to the different retention mechanisms between ^{64}Cu-ATSM and ^{18}F-FDG. It

implies that the either the oxygen tension (<1% oxygen (*129*)) is not low enough to be distinguished by ^{64}Cu-ATSM imaging or alternatively, this finding may also suggest that the relative effect of the ApoE$^{-/-}$ mouse model genetics is stronger than the effect of diet on hypoxia progression in atherosclerotic plaque, or a combination of these reasons.

Further studies could be performed using logistic regression analysis to compare immunoreactivity scores of PIMO-determined hypoxia in the plaques as well as other immunohistochemistry markers of hypoxia (HIF 1α, HIF 2α and VEGF) to the continuous variable of SUV, and to the A/M SUV ratios post injection of ^{64}Cu-ATSM. HIF-1α and HIF-2α are often used as markers of hypoxia. The expression of VEGF is low in normal vessel wall and up-regulated by hypoxia, inflammatory mediators, and certain growth factors. The human study from Slumer et al. in 2008 (*26*) demonstrated increasing expression of these hypoxia markers over the development of atherosclerosis. Nevertheless, another study using an atherosclerotic murine model found that all three markers of hypoxia correlated negatively with SUV_{mean} of ^{18}F-FDG (*115*). The discordant finding was explained by the limited number of lesions investigated in the human study, smaller lesions in mice compared to human, and potentially dissimilar gene expression of molecular markers of hypoxia between and mice and human, etc. In future studies, we can validate whether these hypoxia markers will correlate positively with the uptake of ^{64}Cu-ATSM to provide more data to explain this discrepancy.

One limitation in the study is the relatively poor spatial resolution of the small animal PET and coregistered CT scanner. The diameter of mouse aortic arch is about 1 mm (*130*), which is at the same level of the small animal PET resolution (1-2 mm). As a result the effect of partial volume and spillover may deteriorate the imaging quality and cause underestimation the resultant radioactivity. In further studies we will increase the size of animal model from mouse to rabbit, and apply post-processing techniques to correct for partial volume effects. The tiny size of the

mouse aortic arch, which may easily generate shift and deformation during obtaining adjacent sections for autoradiography and immunohistochemistry, together with the dramatic different resolution of the autoradiography plate scanner (50 um) and the confocal microscope (< 5 um), brings up technical difficulty to correlate the autoradiograph and immunohistochemistry images at the pixel level.

In order to justify the activity in the thigh muscle as the background activity for uptake normalization purposes, we collected the samples of aortic arch (with heart attached), blood pool and leg muscle from at least three SCD ApoE$^{-/-}$ mice and control mice after sacrificing (30 minute post injection of ^{64}Cu-ATSM). For the ApoE$^{-/-}$ mice, the %ID/gram of aortic arch with heart (4.02 ± 0.69) was 1.5 time higher than that of blood (2.72 ± 0.18), and 5.1 times higher than that of muscle (0.79 ± 0.11). However, for the control mice the %ID/gram of aortic arch with heart (2.34 ± 0.56) showed a similar value with blood (2.30 ± 0.60), and was 3.9 times higher than the muscle (0.61 ± 0.12). These findings suggest that activity of tracer in muscle is the same between the groups.

In summary, we evaluated the presence of hypoxia in a mouse model of atherosclerosis using ^{64}Cu-ATSM. This PET imaging agent is demonstrated to be superior to ^{18}FDG in terms of imaging hypoxia in atherosclerotic plaques and high image contrast between hypoxic and normoxic tissues 7.5-30 minutes post injection. The results of longitudinal study suggested that genetic factor was a more important reason than environment (e.g. diet) in the development of atherosclerosis.

3.2 ^{64}Cu-ATSM PET/MR imaging of hypoxic atherosclerotic plaque in a rabbit model

This section was previously published as "PET/MRI of hypoxic atherosclerosis using ^{64}Cu-ATSM in a rabbit model" in Journal of Nuclear Medicine (*131*). Copyright (2016) by the Society of Nuclear Medicine and Molecular Imaging, Inc.

3.2.1 ^{64}Cu-ATSM rabbit study: introduction

Hybrid PET/MR imaging modalities provide complementary information to aid in the diagnosis and stating of cardiovascular disease. MR imaging provides superior soft-tissue contrast even in the absence of intravenous MR contrast agents, and multiple MR sequences can be acquired to better clarify tissue and lesion characteristics in a single imaging session. Simultaneous acquisition of MR imaging sequences and PET data avoid image mis-registration and is ideal when using both PET and MR imaging to study rapidly changing biologic processes. In addition, since MR imaging does not use ionizing radiation, PET/MR offers the additional benefit of lower radiation dosimetry than the PET/CT.

Due to the above benefits, we investigated ^{64}Cu-ATSM in a PET/MR hybrid scanner for detecting hypoxic atherosclerosis in a rabbit model. The PET/MR imaging strategy uses MRI for attenuation correction and for co-localization of ^{64}Cu-ATSM uptake on PET to the rabbit femoral artery lesion depicted anatomically on a 3 Tesla MR image. We showed that ^{64}Cu-ATSM could detect hypoxia in this animal model with atherosclerotic-like lesions and that hypoxia in these lesions as determined by ^{64}Cu-ATSM uptake on PET and PIMO staining of the ex-vivo specimen obtained after imaging co-localized to macrophages.

3.2.2 ^{64}Cu-ATSM rabbit study: materials and methods

I. General

Animal studies were performed under a protocol approved by the Animal Studies Committee at our institution. Advanced atherosclerotic-like lesions were induced in the right femoral arteries of 5 New Zealand White rabbits weighing 2.5-3 kg by endothelial denudation with air desiccation 2-4 wk after the start of a Western diet (0.25% cholesterol, Purina TestDiet, Indianapolis, TN) (*132, 133*), depending on when the serum cholesterol level of the rabbits exceeded 2 mg/mL. The left femoral artery underwent a sham operation as the negative control. At the end of the last imaging procedure, the anesthetized animals were euthanized by exsanguination and the arterial segments collected for IHC.

^{64}Cu was prepared as previously described (see section 2.4.2.1).

II. Imaging protocol

The rabbits underwent simultaneous PET/MR (Siemens Biograph mMR) examination 4 and 8 wk after arterial injury operation (Fig. 17). At each time-point, a 0-60 min dynamic whole-body PET/MR exam was performed post-injection (p.i.) of ~111 MBq ^{64}Cu-ATSM. At the second time point, an additional 0-75 min dynamic PET/MR exam p.i. of ~111 MBq ^{18}F-FDG was performed one day prior to the ^{64}Cu-ATSM imaging.

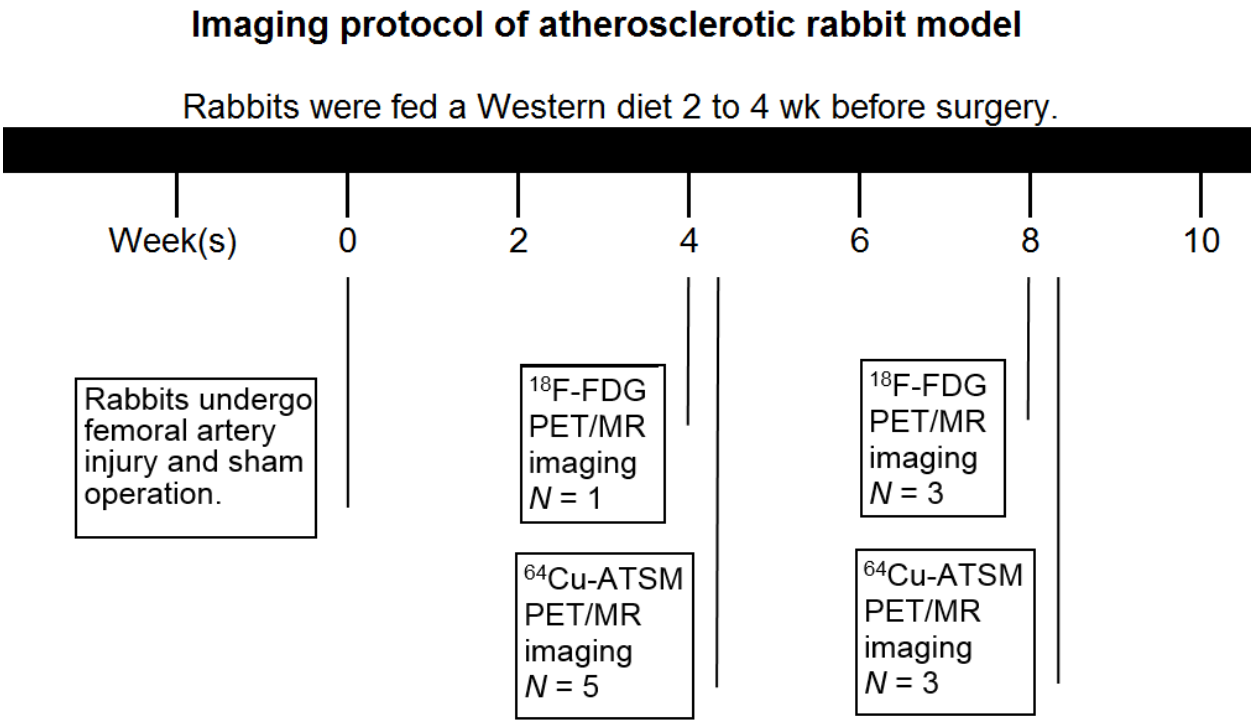

Figure 17 Study protocol for imaging atherosclerosis rabbits.

During PET acquisition, MR scans consisted of T_1-weighted 2D turbo-spin-echo (TSE) (TR/TE = 600/11 ms, number of slices = 16, *field of view* = 60×120 mm, interpolated matrix size = 384×768, signal averages = 12), T_2-weighted 2D TSE (TR/TE = 2200-2890/56 ms, number of slices = 16, *field of view* = 60×120 mm, matrix size = interpolated 384×768, signal averages = 10), and proton density (PD)-weighted 2D TSE (TR/TE = 2200-2890/11 ms, number of slices = 16, *field of view* = 60×120 mm, interpolated matrix size = 384×768, signal averages = 10) were obtained. For all sequences, magnetic field strength = 3T, pixel bandwidth = 260 kHz, echo train length = 7, in-plane resolution = 0.16×0.16 mm, and slice thickness = 2 mm.

MR-based 2-point Dixon attenuation correction for the PET image was performed. The data from the last 30 min of each PET scan was used for *high-definition* (HD) PET imaging reconstruction, performed on the Siemens e7-tools software using point spread function corrected ordinary

Poisson *ordered subsets expectation maximization* (PSF-OP–OSEM) algorithm with 21 subsets, 8 iterations, and a 2-mm full width at half maximum (FWHM) Gaussian smoothing filter. The size of the image matrices were 344×344×127 resulting in a pixel size of 1.04 mm and a slice thickness of 2.03 mm. Dynamic images were decay corrected to the injection time. An average PET spatial resolution of 4.3 mm at 1 cm offset from the *center* of *field of view* was expected to be obtained from the PET/MR scanner (*134*).

III. Image analysis

PET images were co-registered with MR images using Inveon Research Workplace (IRW; Siemens Medical Solutions USA, Inc., Malvern, PA) to identify the location of the plaques developed in the femoral artery. The fused images were evaluated by measuring the radioactivity concentration within the regions of interests drawn on the injured femoral artery (IF), sham-operated femoral artery (SF) and a representative area on the non-target background thigh muscle (BM) of each rabbit.

The mean and maximum of standardized uptake values (SUV_{mean} and SUV_{max}) of IF, SF, and BM were calculated by dividing the decay-corrected activity per unit volume of tissue (Bq/cm^3) by the injected activity per unit of body weight (Bq/g), as described previously.

The mean cross-sectional area of the femoral artery blood vessel wall was measured in transverse T_1-weighted images that show the best contrast between lumen and vessel wall by subtracting the number of pixels of the inner blood vessel area from the outer blood vessel area in transverse MR images and taking the average of the slices containing the plaque.

IV. Histologic analysis

The animals were injected intravenously with the hypoxia-reactive reagent PIMO hydrochloride (Hypoxyprobe-1, Natural Pharmacia International, Belmont, MA) 1.5-2 h before euthanasia. A vitamin capsule as an external marker was used to match injured vessel site and the MRI image volume. The IF and SF were collected and perfusion-fixed with freshly prepared 3-4% paraformaldehyde (PFA) solution to collect specimens for histopathological assessment. Specimens were embedded in paraffin and sectioned transversely. To visualize the spatial co-localization of the hypoxic cells and macrophages, adjacent 5 μm thick cross-sections of the femoral artery were obtained.

IF and SF specimens were stained for the presence of hypoxia using the anti-pimonidazole antibody (Natural Pharmacia Inc., Belmont, MA) and mounted in solution containing 4'-6-diamidino-2-phenylindole (DAPI; Vector Laboratories, Palo Alto, CA) for fluorescent staining of nuclei. Although PIMO may react with reactive oxygen species, the anti-pimonidazole antibody only recognizes hypoxia derivatives (*26*). Fluorescein isothiocyanate was used as the secondary antibody.

Adjacent serial sections were assessed for macrophage content and hypoxia inducible factor-1α (HIF-1α) using mouse monoclonal antibodies for rabbit macrophages (clone RAM-11, Dako North America, Inc., Carpinteria, CA) and anti-HIF-1α (clone H1α67, Novus Biologicals, Littleton, CO).

The bound markers were detected by Cy3 and Cy2 secondary fluorescent antibodies, respectively. The slides were incubated with DAPI prior to cover-slipping. Negative control staining was performed by replacing the primary antibody with a matching isotype control followed by the same

fluorescent-labeled secondary antibody. IHC slides were imaged with use of a Leica TCS SP5 confocal laser scanning microscope.

V. Statistical methods

Data are presented as mean ± standard deviation (SD). Statistical analysis was performed using GraphPad Prism 6 (GraphPad Sofrware, Inc., La Jolla, CA). Differences between the IF/BM and SF/BM SUV were assessed using the Student's *t*-test. The correlation between the IF/SF cross-section area ratios in MR images and the IF/SF SUV ratios in the corresponding ^{64}Cu-ATSM PET images were analyzed by simple linear regression with 95% confidence intervals. $P < 0.05$ was considered statistically significant.

3.2.3 ^{64}Cu-ATSM rabbit study: results

PET/MR imaging showed increased uptake of ^{64}Cu-ATSM in the IF of all 5 rabbits 4 wk after injury, as indicated by the bright spots in both transverse and coronal views co-localizing to the lesion as identified by anatomic MRI (Fig. 18, A and D; Fig. 19). Eight weeks post injury, significantly higher ^{64}Cu-ATSM was found in IF in the PET images fused with T_1-weighted MRI, T_2-weighted MRI and PD-weighted MRI (Fig. 18, B and E; Fig. 20, PD-weighted MRI not shown). Higher uptake of ^{18}F-FDG in the IF of the rabbits confirmed the development of advanced atherosclerotic-like plaque (Fig. 19, C and F; Fig. 21).

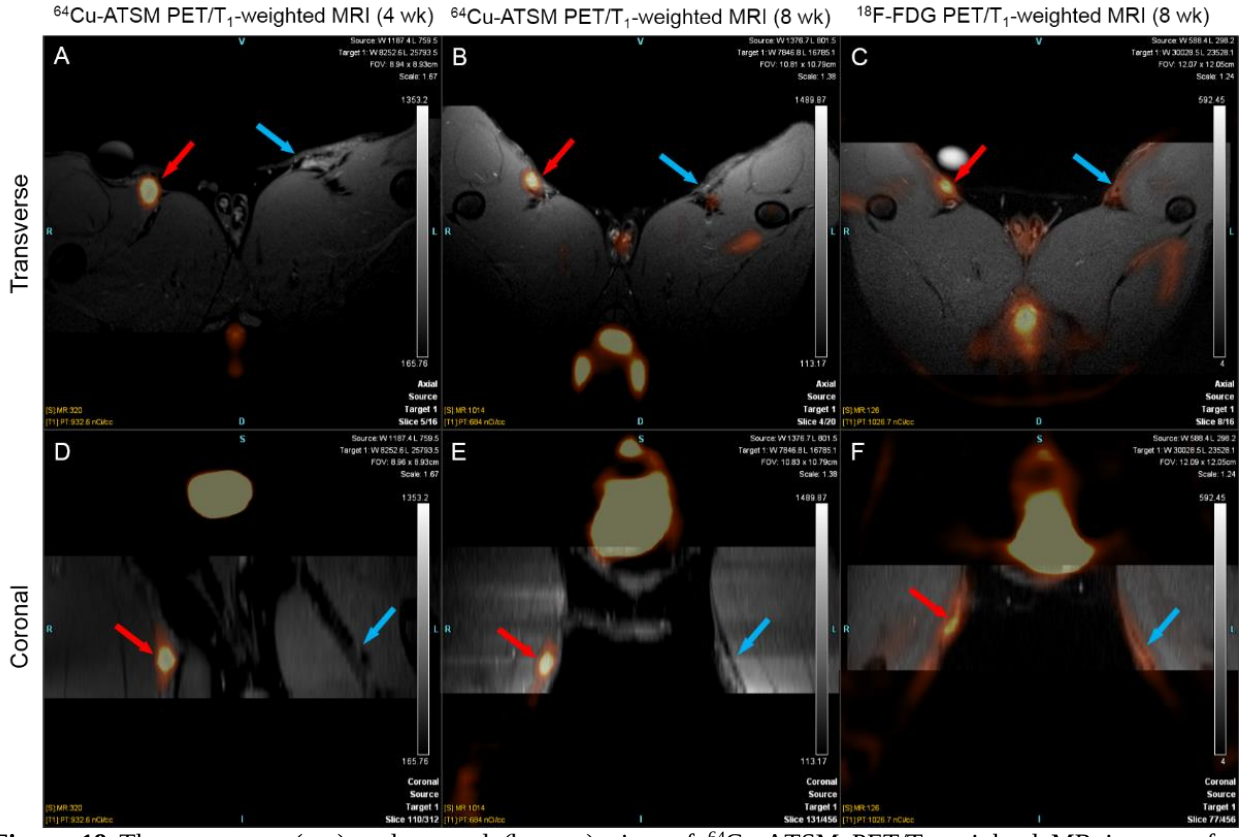

Figure 18 The transverse (top) and coronal (bottom) view of ^{64}Cu-ATSM PET/T_1-weighted MR images of a representative rabbit 4 wk (A, D) and 8 wk (B, E) post injury, and ^{18}F-FDG PET/ T_1-weighted MR images of the same rabbit 8 wk post injury (C, F). Red arrows point to injured femoral artery; blue arrows point to sham-operated femoral artery.

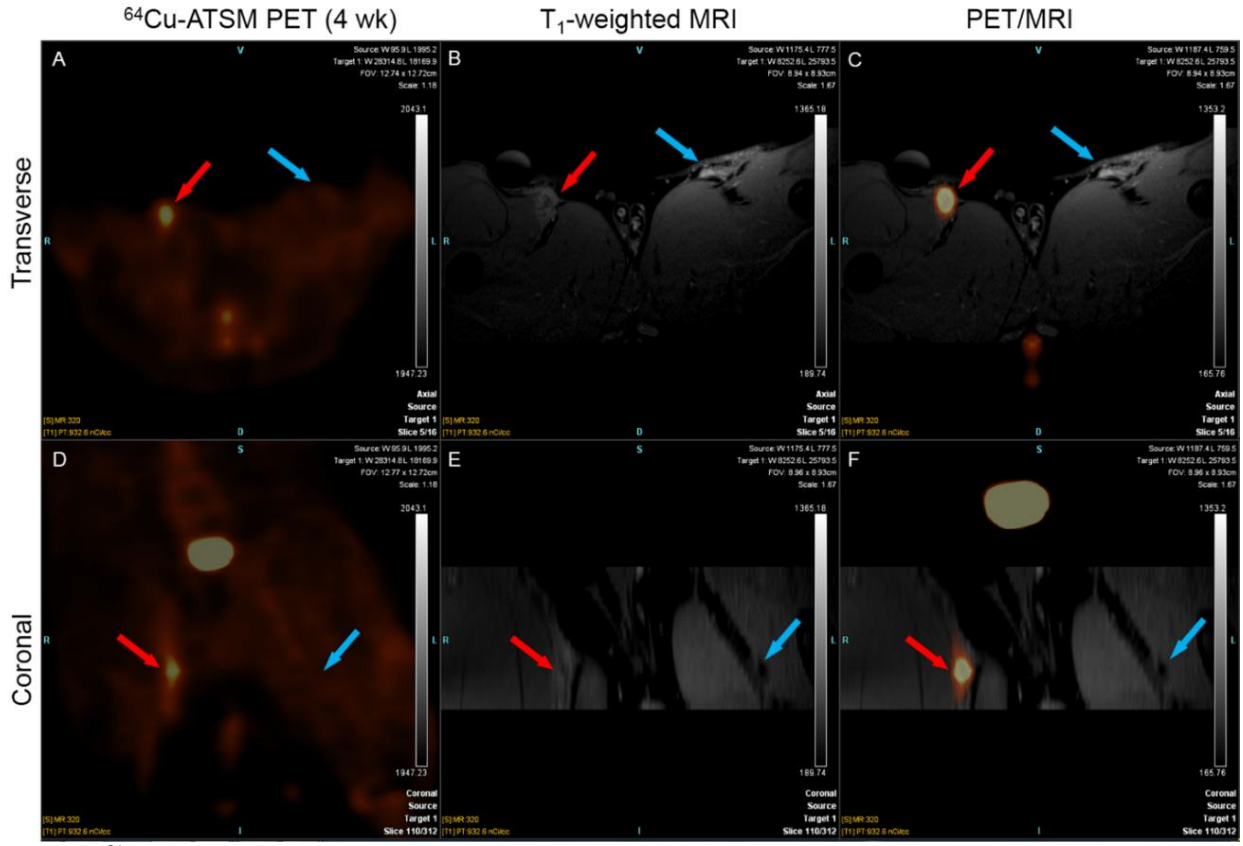

Figure 19 ^{64}Cu-ATSM PET/MR images of a representative rabbit shown in Figure 21 4 wk post injury. The transverse (top) and coronal (bottom) view of the PET images (A, D), T_1-weighted MR images (B, E) and fused PET/MR images (C, F) indicated a significantly elevated uptake of ^{64}Cu-ATSM in the IF as compared to the SF. Red arrows point to injured femoral artery; blue arrows point to sham-operated femoral artery.

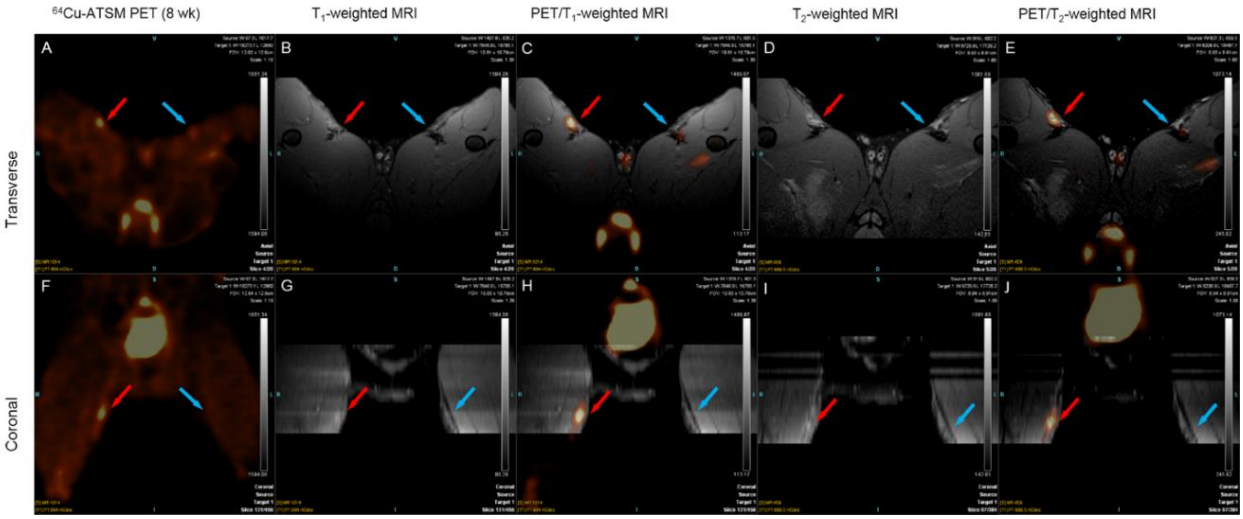

Figure 20 ^{64}Cu-ATSM PET/MR images of the same representative rabbit shown in Figure 21 8 wk post injury. Significant uptake of ^{64}Cu-ATSM was also found in the IF as compared to the SF as shown in transverse (top) and coronal (bottom) views of the PET images alone (A, F), fused either with T_1-weighted MR images (MR: B, G; fused PET/MR: C, H) or T_2-weighted MR images (MR: D, I; fused PET/MR: E, J). Red arrows point to injured femoral artery; blue arrows point to sham-operated femoral artery.

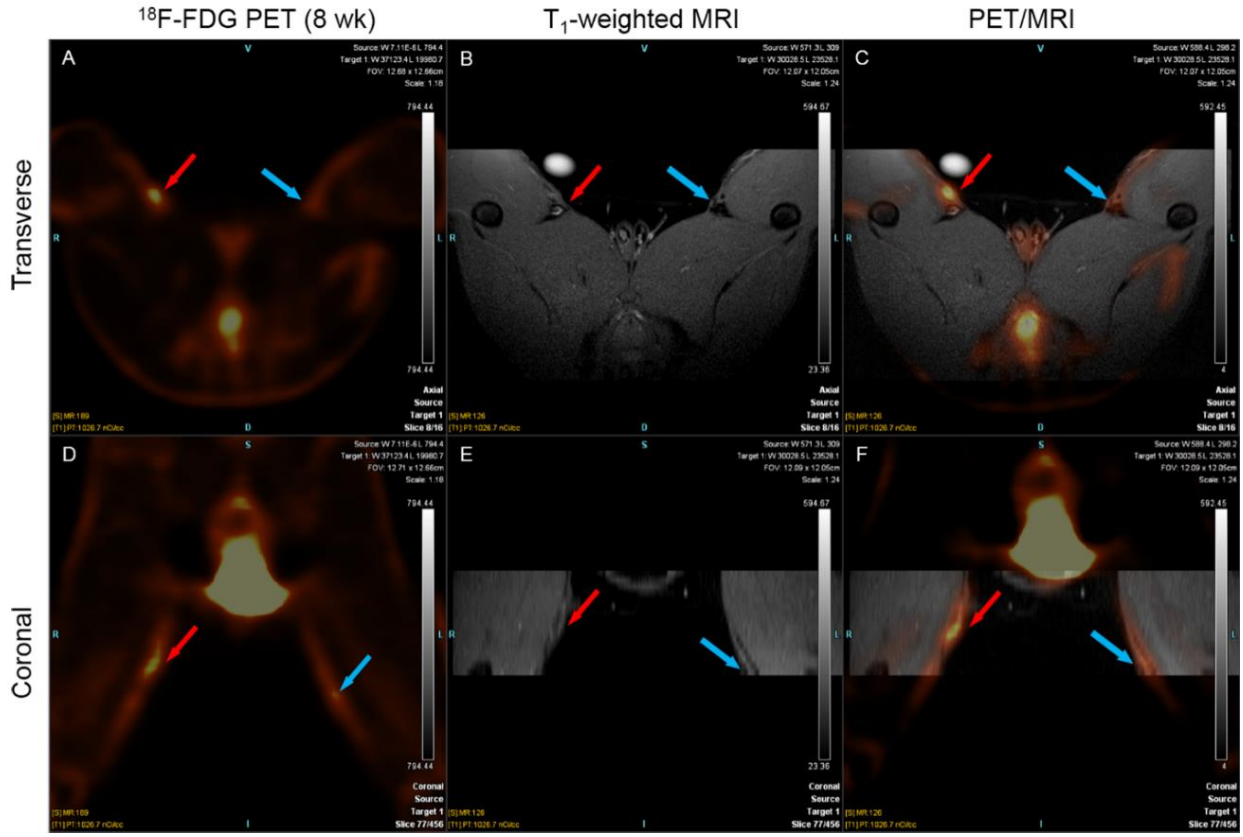

Figure 21 ^{18}F-FDG PET/MR images of the same representative rabbit shown in Figure 21 8 weeks post injury. The transverse (top) and coronal (bottom) view of the pure PET images (left, A, D), pure MR images (middle, B, E) and fused PET/MR images (right, C, F) showed a higher uptake of ^{18}F-FDG in the IF as compared to the SF. Red arrow points to injured femoral artery; blue arrow points to sham-operated femoral artery.

The IF demonstrated 1.75 ± 0.21, and 2.30 ± 0.26 fold higher SUV_{mean} ratios and 1.61 ± 0.15, and 1.84 ± 0.12-fold higher SUV_{max} ratios 30-60 min p.i. of ^{64}Cu-ATSM in comparison to the SF 4 and 8 wk after injury (Fig. 22), respectively. ^{18}F-FDG imaging demonstrated 2.31 ± 0.29 IF/SF SUV_{mean} ratios and 1.82 ± 0.26 IF/SF SUV_{max} ratios 4 and 8 wk after injury (Fig. 22). IF/BM SUV ratios were significantly higher ($P < 0.001$) than SF/BM SUV ratios both 4 and 8 wk after injury p.i. of ^{64}Cu-ATSM and 8 wk after injury p.i. of ^{18}F-FDG ($P < 0.05$) (Fig. 23).

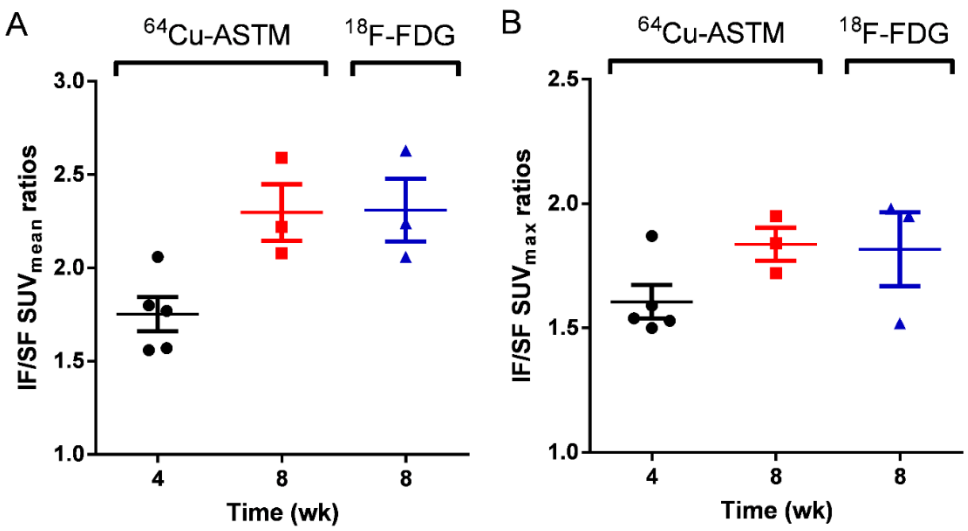

Figure 22 IF/SF SUV_{mean} (A) and SUV_{max} (B) of the rabbits in both ^{64}Cu-ATSM and ^{18}F-FDG images increased over time after injury.

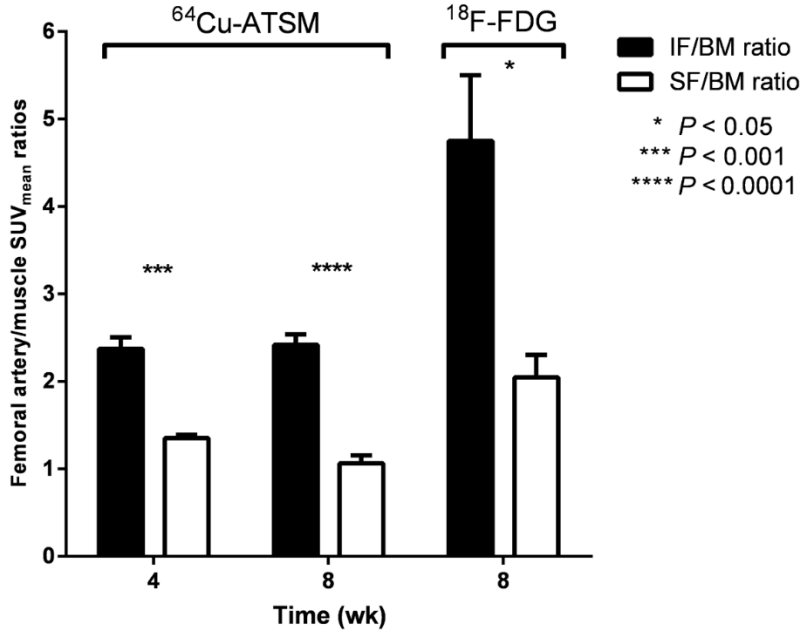

Figure 23 IF/BM SUV_{mean} ratios were significantly higher than SF/BM SUV_{mean} ratios 4 and 8 wk post injury in ^{64}Cu-ATSM imaging, and 8 wk post injury in ^{18}F-FDG imaging.

IF/SF SUV ratios measured from ^{64}Cu-ATSM PET images did not show a significant correlation with specific signal on T_1, T_2, or PD-weighted MR images. Nevertheless, the combination of all three sequences helped to delineate the plaque and lumen boundaries. The ratios of IF/SF blood vessel wall cross-sectional areas determined by T_1-weighted images was strongly positively

correlated to IF/SF SUV_{mean} ratios in a linear regression (R^2 = 0.742, *P* = 0.0002) (Fig. 24). This finding suggested an increasing lipid content and hypoxic level in the IF during the progression of atherosclerosis, as supported by the thickening of the IF blood vessel wall.

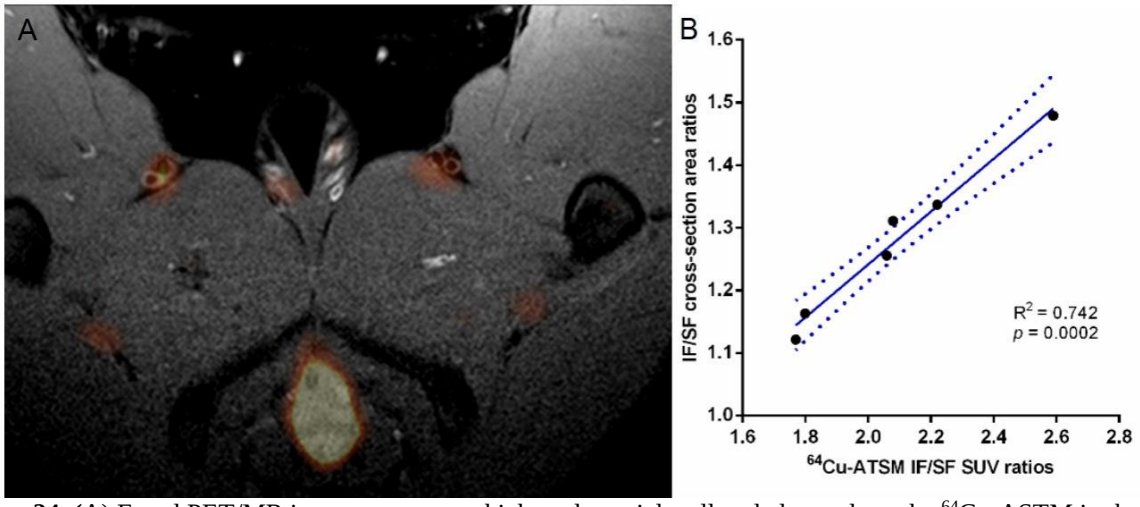

Figure 24 (A) Fused PET/MR image suggests a thickened arterial wall and elevated uptake ^{64}Cu-ASTM in the IF as compared to the SF. (B) Linear regression analysis shows that ^{64}Cu-ATSM PET IF/SF SUV_{mean} ratios are positively correlated to IF/SF cross-section area ratios measured in T_1-weighted MRI images.

Hematoxylin and eosin (H&E) stain demonstrated a focal thickened neointima comprised of foam cells and vascular smooth muscle cells was generated in the injured vessel (Fig. 25). Immunohistochemical analysis showed that the induced atherosclerotic-like lesions contained macrophages as indicated by RAM-11, which co-localized to the HIF-1α positive area (Fig. 26, A, B and D). Hypoxia, as shown by PIMO staining of the adjacent section, was located in the deep macrophage-rich area within the atheromatous core of the plaque (Fig. 26, C; Fig. 27). Superficial macrophages adjacent to the lumen stained negatively with PIMO, suggesting that these superficial macrophages were not hypoxic (Fig. 27), consistent with what has been described previously (*119*). No immunofluorescence of RAM-11, HIF-1α, or PIMO was seen in the sham-operated femoral artery sections (Fig. 28).

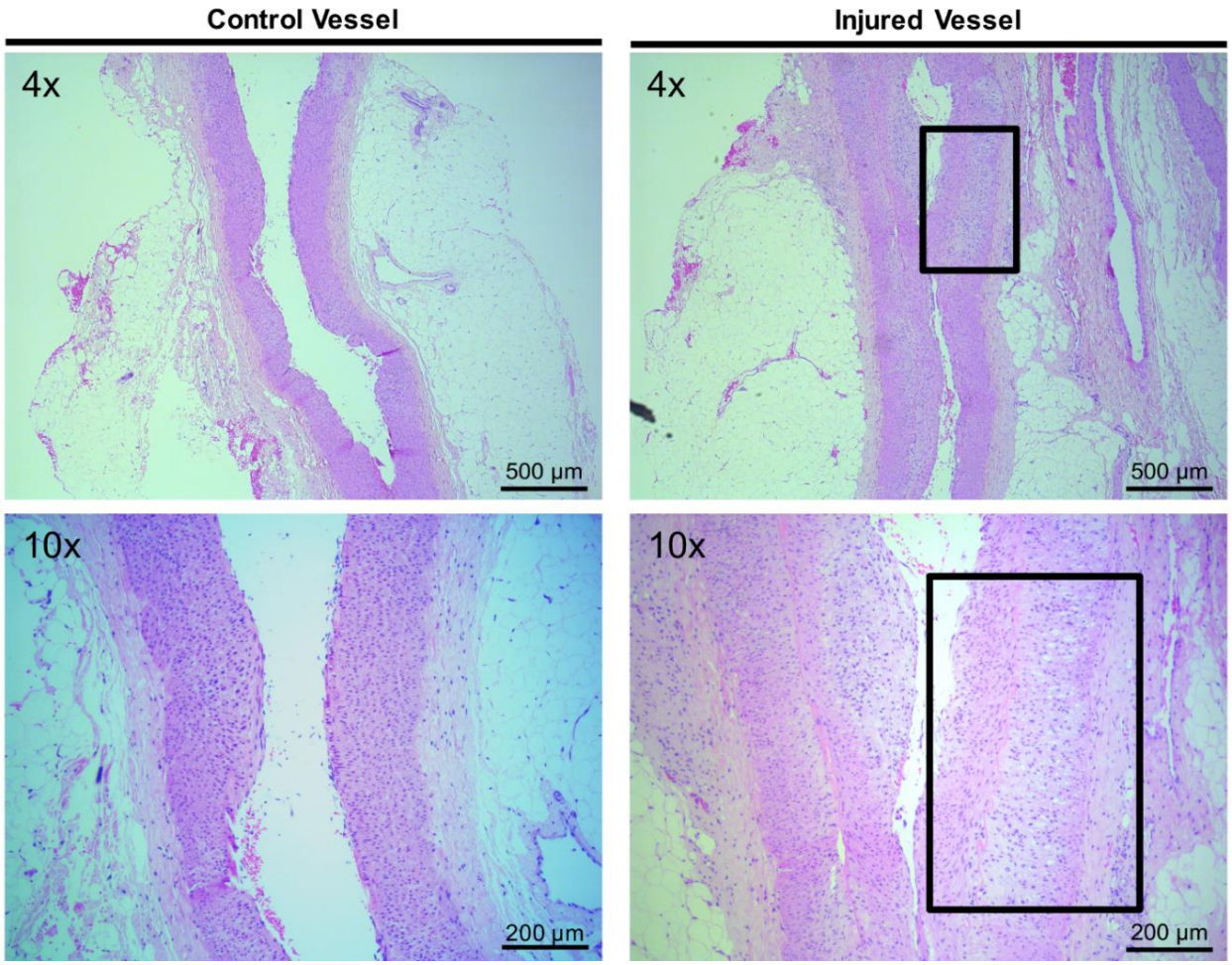

Figure 25 Hematoxylin and eosin (H&E) stain of the sham-operated (control) femoral artery (left) and injured femoral artery (right) in 4X (top) and 10X (bottom) magnification shows that feeding cholesterol-enriched diet and air dessication produced a focal thickened neointima in the area of previous air dessication that was comprised of foam cells, and vascular smooth muscle cells. The duration of cholesterol diet was too short to see lesions induced in peripheral arteries other than the one associated with air dessication.

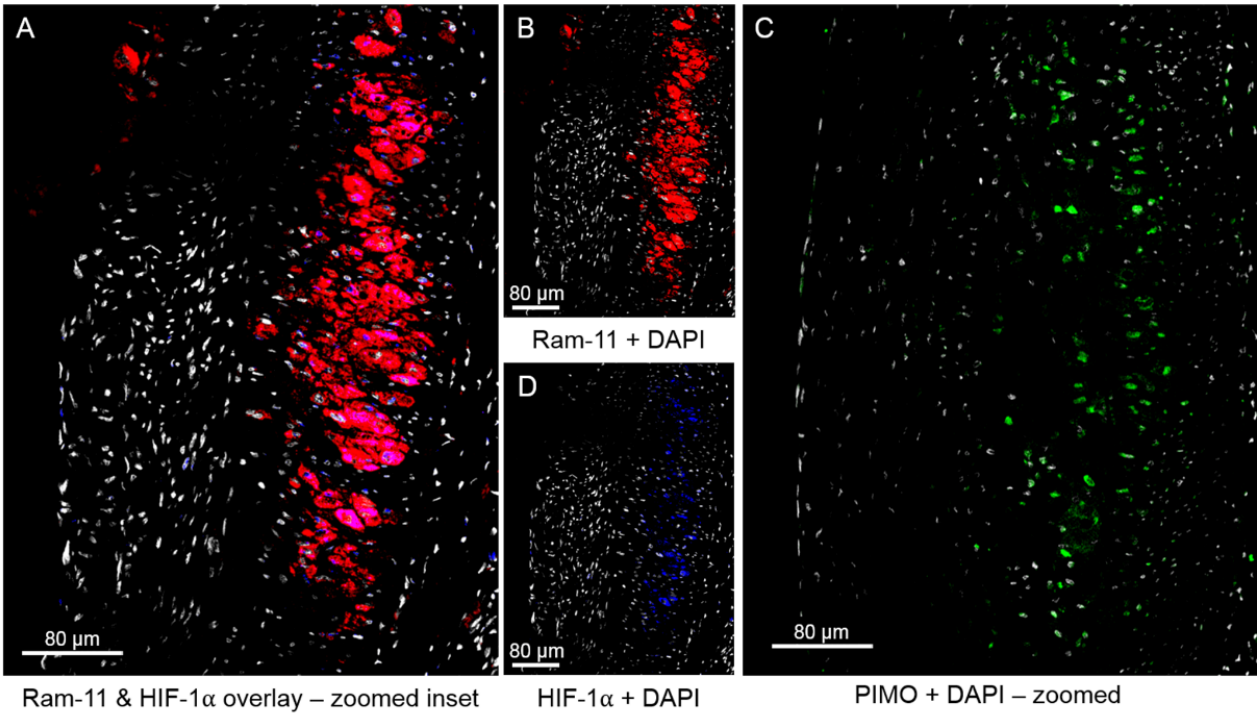

Figure 26 In the atherosclerotic plaque of the injured femoral artery, HIF-1α staining is localized within areas of high RAM-11-positive macrophages (A), confirmed by viewing single channels staining of RAM-11 (B) and HIF-1α (D). Detection of pimonidazole (PIMO) adducts was done on the adjacent slide (C), and pimonidazole positivity was observed in the area of RAM-11+HIF-1α displayed in panels A, B and D. Panels A and C are at the same scale. For all panels the color code is as follows: DAPI, white; RAM-11, red; HIF-1α, blue; PIMO, green.

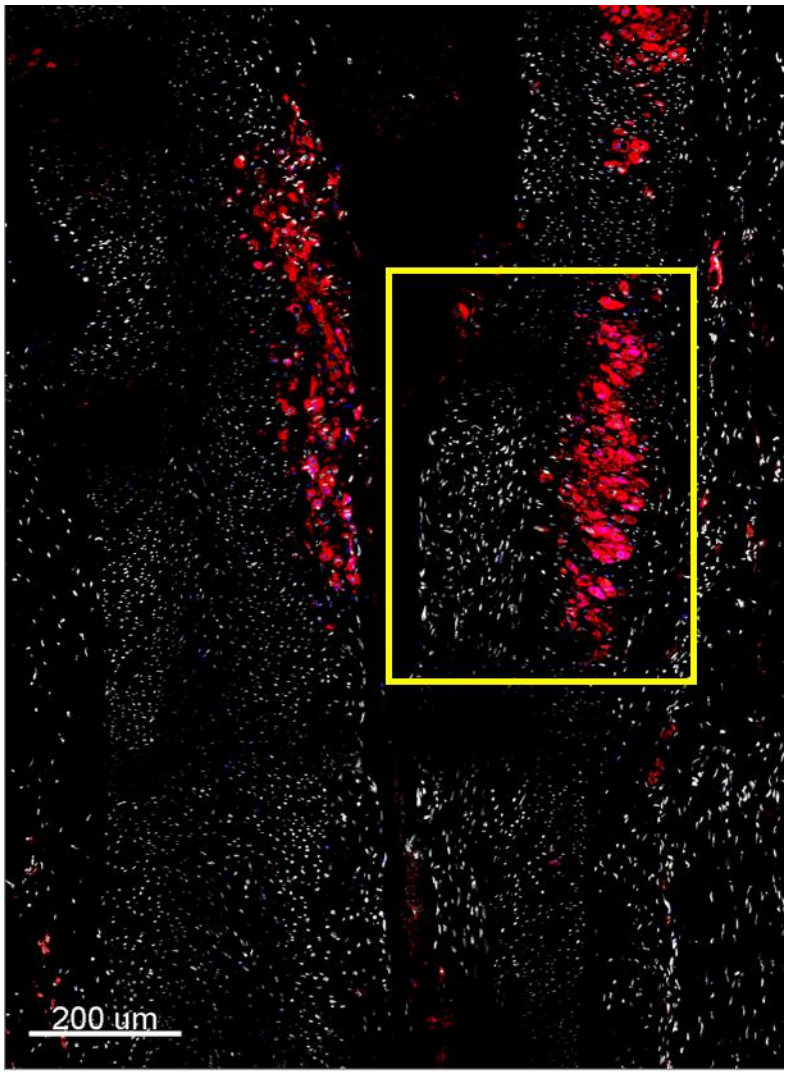

HIF-1α & Ram-11 overlay – area scan

Figure 27 Area scan containing the injured femoral artery depicted in Figure 29 shows the presence of both deep and superficial macrophages in RAM-11 staining which are co-localized to HIF-1α staining. However, only deep macrophage-rich area is pimonidazole positive, as displayed in Figure 4(C). The color code is as follows: DAPI, white; RAM-11, red; HIF-1α, blue.

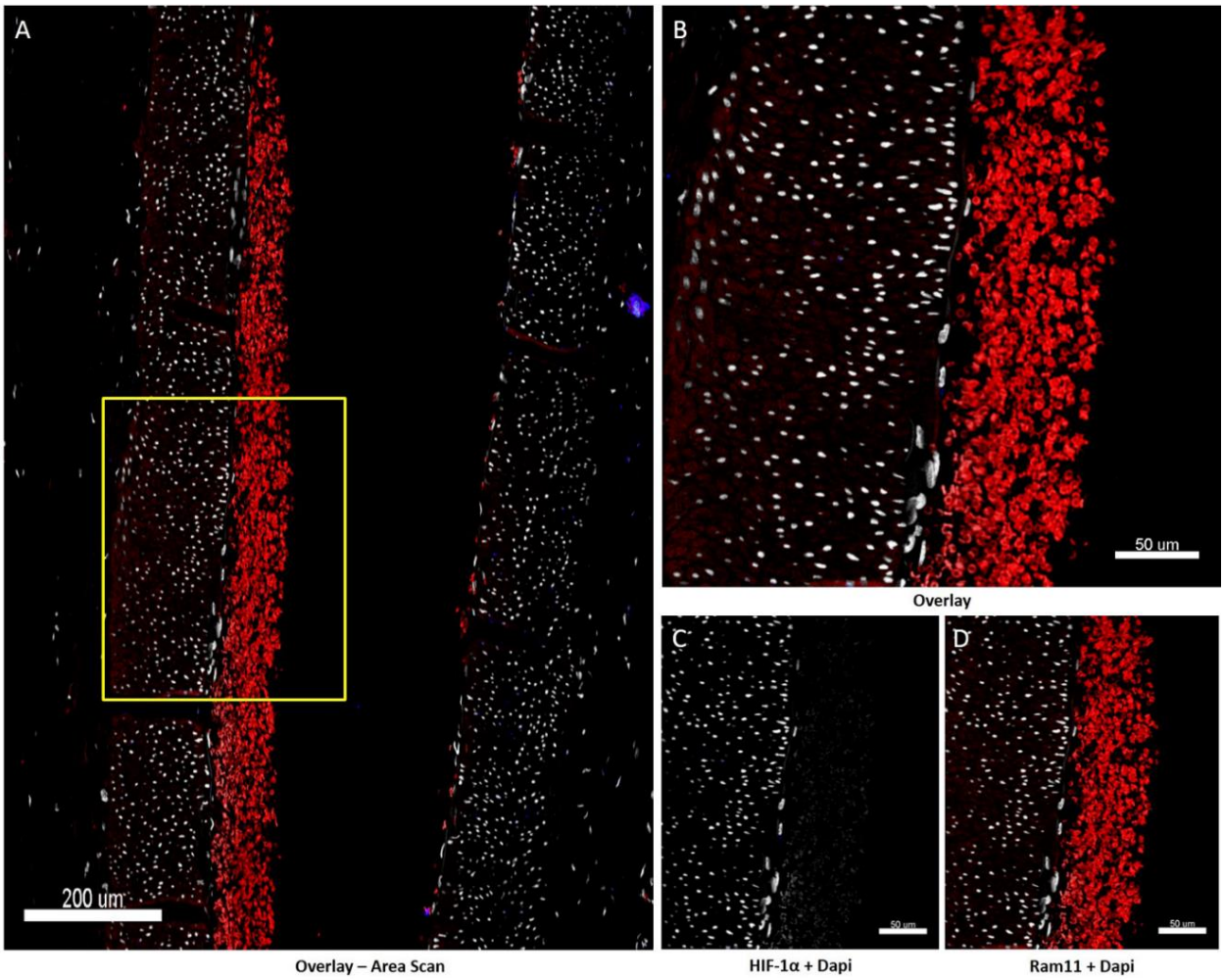

Figure 28 Immunofluorescence images of the sham-operated femoral artery showing that neither Ram-11 nor HIF-1α were positively stained in this region. Red observed is red blood cells (non-nucleated). Images of PIMO staining from the adjacent section (no positive results) were not included in this figure.

3.2.4 ^{64}Cu-ATSM rabbit study: discussion

In this study, we demonstrated the ability of ^{64}Cu-ATSM PET to noninvasively detect hypoxia in advanced atherosclerosis-like lesions in rabbit model. To our knowledge, this study is the first investigation of ^{64}Cu-ATSM as a hypoxic cell PET imaging agent in a non-murine animal model of atherosclerosis, and it suggests that ^{64}Cu-ATSM PET/MR is a promising imaging method for detecting hypoxic and potentially vulnerable atherosclerosis in human subjects.

Although PET/CT as a hybrid scanner has in the past emerged as a valuable modality in clinical use as well as an important research tool, the fully integrated PET/MR scanners provide the

excellent soft tissue contrast and functional imaging capabilities of MR (*135*). The described morphological features of plaque vulnerability can be nicely imaged by MRI (*136*) and the biological features of plaque vulnerability can be visualized by PET with different tracers and targets in a complementary fashion (*137-139*). Thus PET/MR allows for multiparametric profiling of plaque morphology and potentially vulnerability in one imaging session and should facilitate the identification of high-risk plaques in patients with atherosclerotic disease (*135*). These non-oncological applications may further benefit from lower radiation exposure of the patients in PET/MR compared to PET/CT (*140*). In light of these advantages, imaging of atherosclerosis using fully integrated hybrid PET/MR yields an additional diagnostic value both over stand-alone PET and MR scanners and as well as over hybrid PET/CT.

The H&E stain, along with our previous work (*133*), showed that a combination of a cholesterol-enriched diet and air dessication produced a focal thickened neointima in the area of air dessication comprised of foam cells and vascular smooth muscle cells. The duration of cholesterol diet in these animals was too short to see lesions induced in peripheral arteries outside of the region of air dessication, thus allowing us to use the contralateral sham artery as a control. The hypoxia-specific dye PIMO used for histopathologic characterization *ex vivo* is a 2-nitroimidazole containing a basic, piperidine moiety and reduces in cells with low oxygen tension. It is considered as the "gold standard" immunohistochemical hypoxia marker and widely used as a hypoxia-specific dye ($pO_2 \leq 10$ mm Hg). The resulting PIMO derivatives form protein adducts, which can be detected by immunostaining (*24*). This agent has been used primarily in oncologic specimen assessment (*25*) and only recently in assessment of atherosclerosis (*26*). The co-localization of the macrophage marker (RAM-11) and hypoxia indicators (PIMO) suggested the uptake of ^{64}Cu-ATSM was associated with the presence of macrophages. Despite stimuli other than hypoxia that may induced

HIF-1 in normoxia (*141*), a previous study (*119*) demonstrated that nearly all macrophages present in the plaque expressed HIF-1α, and a strong correlation between the hypoxic region (PIMO) and macrophage (RAM-11) density in plaque by immunohistology. Thus, the presence of HIF-1α in the same region as the macrophages in the lesions served as supportive evidence of hypoxia in atherosclerotic macrophages. In addition, the finding that hypoxia was mainly located in the deep, macrophage-rich area within the atheromatous core was consistent with this study (*119*), which suggested that enough oxygen could diffuse from the lumen to nourish the shallow macrophage population but not the deep macrophage-rich core owing to the increased consumption and/or reduced supply of O_2 and nutrients from the lumen and vasa vasorum to those regions. The significantly higher ^{18}F-FDG uptake in the injured femoral artery further helped to confirm the development of advanced plaque and accumulated macrophages in this region. In previous publications, it was shown that macrophages have a high uptake of ^{18}F-FDG (*125*). Moreover, even though we did not assess the biodistribution of ^{64}Cu-ATSM in blood, muscle, and femoral arteries to validate the complete clearance of radiopharmaceuticals at the time periods used for SUV calculation, our methods for SUV comparison – injured femoral to sham femoral SUV ratios – show the absence of radioactivity in the blood pool excluding potential bias that could result from the radioactivity contribution from the blood pool (*125*).

Similar to the ^{64}Cu-ATSM PET imaging study of mice, an important limitation of our study is that the SUVs were not corrected for partial volume effects (PVEs). The quantitative accuracy of PET is reduced by PVEs primarily due to the limited spatial resolution of the scanner leading to underestimation of the SUV with decreasing structural size of plaques (*142, 143*). In practice, PVE is minimal when the dimensions of homogenous uptake region are > 2- to 3-times the spatial resolution of the scanner (*144*). The spatial resolution of the Siemens mMR PET/MR system is

approximately 4.3 mm (*134*, *145*), while the rabbit's femoral artery is 1.5-1.8 mm in diameter (*146*). As a result, quantification of tracer uptake in rabbit atherosclerotic plaque is likely to be significantly affected by PVEs. Therefore, it is necessary to apply PVEs correction techniques to exploit the ability of PET/MR to provide high resolution PET images for improved absolute quantitative assessment of hypoxia in atherosclerotic plaque.

Furthermore, in this project, we used standard multi-contrast MRI sequences to image femoral arterial plaque with the initial intent of identifying plaque components in this rabbit model of atherosclerosis. However, because of the relatively small plaque size, limited MRI spatial resolution, and simple plaque components (smooth muscle cells and foam cells), it was difficult to consistently differentiate plaque components by this approach and to obtain quantitative plaque composition information from MR images to conduct specific studies correlating MRI characteristics of atherosclerosis with PET signal.

3.3 ^{64}Cu-ATSM PET/MR imaging of hypoxic atherosclerosis in human carotid artery

We made significant strides in demonstrating that the hypoxic cell PET imaging agent ^{64}Cu-ATSM could be used for the imaging of hypoxic plaque with animal studies, and collected preliminary data to support further studies to fully validate the feasibility of imaging the extent of hypoxia in patients with carotid atherosclerosis.

PET/MRI of human atherosclerosis in the carotid arteries has so far been focused primarily on FDG (*147*). Several studies have used sequential PET and MRI for imaging atherosclerotic plaques in human carotid arteries (*148-152*). However, we were the first group who used ^{64}Cu-ATSM as the PET contrast agent to target hypoxia in human carotid atherosclerosis.

Our IND (125353) for a pilot clinical trial to determine whether ^{64}Cu-ATSM PET/MR scanning is capable of detecting hypoxic carotid atherosclerosis in human subjects was approved by the FDA for initiation of the human study.

3.3.1 ^{64}Cu-ATSM patient study: materials and methods

9 patients with carotid atherosclerosis with percent stenosis of at least ≥ 50% diameter as diagnosed by Doppler ultrasound were recruited from the vascular surgery clinic of Dr. Mohamed Zayed and his colleagues. ^{64}Cu-ATSM PET imaging with simultaneously-acquired dedicated MR imaging for carotid plaque anatomic characterization was performed in 7 patients (two were claustrophobic and couldn't tolerate the imaging). Of these 7 patients, in 6 patients imaging was of diagnostic quality. Imaging was non-diagnostic in one secondary to patient motion.

I. PET-MRI imaging protocol

^{64}Cu-ATSM was prepared as described previously using commercially available GMP radiopharmaceutical kits. All patients underwent simultaneous PET and MRI examination of the carotid arteries on a PET/MRI systems (mMR, Siemens Medical Solution, Erlangen, Germany) equipped with a state-of-the-art bilateral 4 channel phased-array small field carotid coils (*153*). The coils allowed for sub-millimeter resolution of the carotid lumen, vessel walls and atherosclerotic plaques. The purpose of the MRI scan was to determine various plaque components (lipid core, calcification, intraplaque hemorrhage) with submillimeter spatial resolution that was far better than that of PET imaging which had an in-plane resolution of 4 mm at best. This allowed direct correlation of plaque components to the ^{64}Cu-ATSM signal identified on PET imaging. After the scout imaging to localize the carotid arteries in 3 orthogonal planes, a scan for attenuation correction (AC) was performed. Then a 3D T_2-weighted SPACE sequence was executed to obtain an isotropic 3D data set of dark-blood carotid artery images. This data set was used to determine

the orientation of both right and left carotid arteries in coronal orientation. The imaging parameters was: TR/TE=1500 ms/236 ms, bandwidth = 574 Hz/pixel, flip angle = 120^{o}, FOV = 180×134 mm^2, matrix size = 256×192, total 56 slices, average number = 2, slice thickness = 0.7 mm, coronal plane, and scan time = 7 min.

After localizing the carotid arteries, 18-20 mCi of ^{64}Cu-ATSM was injected intravenously. The following MR scans were performed simultaneously with the PET acquisition. To insure that the ^{64}Cu-ATSM uptake was optimally imaged, PET imaging was acquired in list mode over the entire 60-min MR acquisition period. If additional time was needed to achieve optimum radiotracer distribution, patients would be rescanned at 90 minutes post injection. All MRI techniques were well established and had been used extensively by our group (*154*). These included:

1. Dark Blood T_1-weighted: The MRI sequence was TSE sequence with echo sharing and no ECG triggering. Superior and inferior pre-saturation bands was used to suppress blood signal. Imaging parameters were: TR/TE=700-800 ms/8 ms, FOV=140× 140 mm^2, matrix size = 256×256 and was interpolated to 512×512, pixel size = 0.27×0.27 mm^2, bandwidth = 345 Hz/pixel, echo train length = 13, signal average = 2, 18 slices, no slice gap, and slice thickness = 3 mm. These image resolution and volume coverage were exactly the same as following scans.
2. Dark Blood T_2, Proton Density-weighted: TR/TE1/TE2= 2000 ms/8 ms/45 ms, signal average = 2.
3. Bright blood 3D gradient-echo (GRE) T_1-weighted time of flight (TOF): TR/TE = 25/3.5 msec, flip angle = 25^{o}, signal average = 2.

II. PET/MR data analysis

PET data demonstrating plaque wall radiotracer activity would then be summed over the appropriate time frames during reconstruction. The 30-60 min data from each PET scan was used for *high-definition* (HD) PET imaging reconstruction, performed on the Siemens e7-tools software using point spread function corrected ordinary Poisson *ordered subsets expectation maximization* (PSF-OP–OSEM, or simply PSF-OSEM) algorithm with 21 subsets, 8 iterations, and a 2-mm full width at half maximum (FWHM) Gaussian smoothing filter. The size of the image matrices were 344×344×127 resulting in a pixel size of 1.04 mm and a slice thickness of 2.03 mm. MR-based 2-point Dixon attenuation correction for the PET image was also performed. Dynamic images were decay corrected to the injection time. MR image was fused with reconstructed PET image on Inveon Research Workplace (IRW; Siemens Medical Solutions USA, Inc., Malvern, PA). All 2D MRI images were used for determining location and extension of the plaque components. Carotid PET images were assessed for visual uptake of ^{64}Cu-ATSM and SUV and plaque-to-background SUV ratios.

III. K^{trans} measurement

a. DCE-MR imaging protocol

For two of the patients who agreed to undertake dynamic contrast enhancement magnetic resonance imaging (DCE-MRI), simultaneous to the ^{64}Cu-ATSM PET scanning, DCE-MR imaging was performed between acquisition of pre- and post-contrast TSE imaging sections. Three-dimensional DCE T_1-weighted fast field-echo images were acquired by obtaining 14 transverse over-contiguous sections for 20 time frames with a separation of 12.5 seconds between frames. Total imaging time was approximately 4 minutes (250 seconds). Contrast material was intravenously injected at the beginning of the third time frame with use of a power injector. Contrast material was injected at a rate of 0.5 mL/sec, followed by injection of a 20-mL saline

flush at the same rate. Relevant imaging parameters were as follows: spatial resolution, 0.703×0.703 mm^2; section thickness, 3.0 mm; field of view, 18×18 cm; and matrix size, 256×256. A spatial saturation slab at the caudal position parallel to the imaging plane was added to reduce inflow artifacts.

b. Pharmacokinetic Modeling

The contrast agent dynamics was quantified using the standard Patlak kinetic model for the DCE-MR images. This pharmacokinetic model is based on the two-compartment model (Fig. 29) and model assumes that a well-mixed tracer exists in each of the compartment in a uniform concentration. A third (intracellular) compartment is assumed to exhibit no uptake of contrast agent.

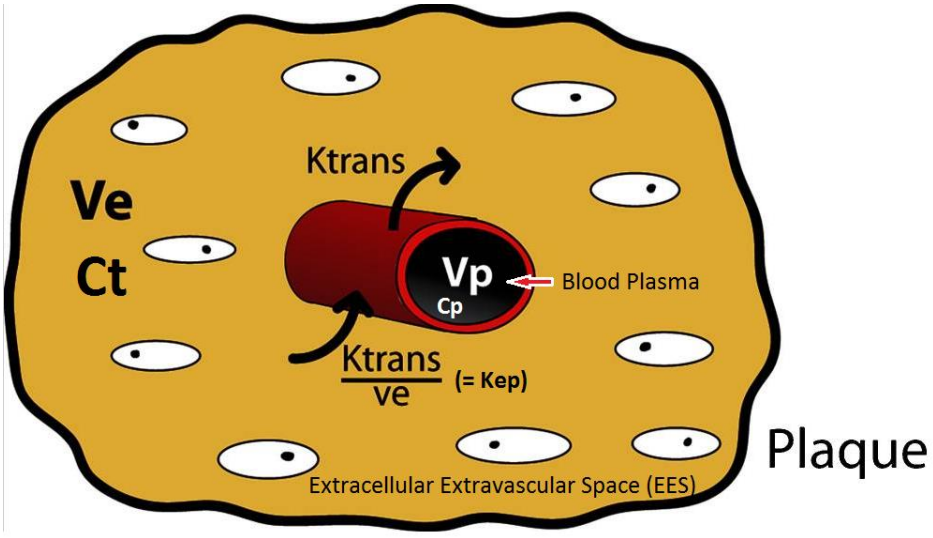

Figure 29 Schematic illustration of pharmacokinetic parameters used in two-compartment models to describe the microvasculature in atherosclerotic plaque microvasculature. v_p represents the fractional blood volume; v_e represents the fraction of the extracellular extravascular space (EES); K^{trans} is the contrast medium transfer rate from the microvasculature to the EES, while K^{trans}/v_e describes the reflux. (Adapted and modified from "Dynamic Contrast-Enhanced MRI to Study Atherosclerotic Plaque Microvasculature," by Raf H. M. van Hoof, Sylvia Heeneman, Joachim E. Wildberger, and M. Eline Kooicorresponding, 2016, *Curr Atheroscler Rep*, Volume 18, p33. Copyright (2016) by title of publisher and is distributed under the terms of the Creative Commons Attribution 4.0 International License.)

The DCE-MR images were analyzed to generate signal enhancement curves of discrete data points for each of the pixels in the images (raw data, C_t), including the carotid plaques and blood vessel walls. C_p was determined by curve fitting the arterial or vascular input function (AIF/VIF) with data points from a 3-mm-diameter circular ROI in the center of the jugular vein at the most caudal section, using a slightly adapted equation introduced by Parker et al (*155*), as follows:

$$C_p(t) = \frac{A}{\sigma\sqrt{2\pi}} e^{-\frac{(t-T)^2}{2\sigma^2}} + \frac{\alpha e^{-\beta t}}{1+e^{-s(t-\tau)}}, \quad (2)$$

where A, σ, and T are the scaling constant, width, and center of the Gaussian, respectively; α and β the amplitude and decay constant of the exponential function, respectively; and s and τ the width and center of the sigmoid, respectively.

Measurements of C_t and C_p over time—assumed to be linearly proportional to the change in signal intensity of the contrast agent in the tissue and blood (*156*) —are sufficient to solve for K_{trans} and v_p by for each voxel separately by curve fitting the equation $C_t(t) = v_p C_p(t) + K^{trans} \int_0^t C_p(\tau)\, d\tau$. The maps of K^{trans} and v_p values on a pixel-by-pixel basis were created accordingly.

The curve fitting process was performed by the least-squares curve-fitting routine lsqcurvefit.m MATLAB (MathWorks) function with Gauss-Newton optimization. To exclude nonphysical solutions, the values of K^{trans} were constrained to the maximum of 1 and minimum of 0. This enabled generation of the maps of K^{trans} and v_p values on a pixel-by-pixel basis with which to assess plaque heterogeneity. The relative fit errors (RFE) errors that indicated the ability of the model to describe the data was calculated as follows:

$$REF = \sqrt{\frac{\sum(C_{t,fit} - C_t)^2}{\sum C_t^2}}, \quad (3)$$

where $C_{t,fit}$ is the fitted tissue concentration and C_t is the measured tissue concentration at the sampled time points. The mean and standard deviation REF was calculated over all voxels.

III. Immunohistochemistry analysis

One of the 6 patients with diagnostic PET/MRI images underwent endarterectomy surgery. This patient was administered PIMO (0.5 g/m^2) orally 2 h prior to the scheduled standard of care endarterectomy. At the time of surgery, a research coordinator/assistant was sent to the operating room to collect each endarterectomy specimen in normal saline. Specimens were refrigerated immediately at 4ºC and was processed within 4 hrs. Because PIMO has been shown to detect hypoxia in normal skin, we also asked the surgeon to provide us a small specimen of normal skin taken at the site of surgery as a positive PIMO control.

The carotid endarterectomy specimen as well as autopsy specimens from ~5 normal subjects as controls were processed, decalcified (when necessary), embedded in paraffin and sectioned transversely. Serial 5-μm sections from every 4 mm intervals was placed on slides for IHC ~~and~~ The endarterectomy specimen and skin specimen (but not autopsy controls who had received no prior oral administration of PIMO) were stained for the presence of hypoxia using the antiPIMO antibody (Natural Pharmacia Inc., Belmont, MA). Sections were also stained with primary antibodies against HIF-1α (clone H1α67, Novus Biologicals, Littleton, CO) and macrophages (CD68) and hypoxia was co-localized to the presence of HIF-1α and CD68. IHC slides were imaged with use of a Leica TCS SP5 confocal laser scanning microscope. Standard hematoxylin

and eosin (H&E) and/or Verhoeff Van Gieson (VVG) staining was also performed in both the endarterectomy specimen and in the autopsy controls.

3.3.2 ^{64}Cu-ATSM patient study: results

For 6 of the 7 patients with acceptable image quality, all were asymptomatic but showed plaques in either carotid artery or vertebral artery. Two patients had uptake of ^{64}Cu-ATSM in carotid plaques (Fig. 30), while 3 had uptake in vertebral plaques (Fig. 31, Table 2). The 30-60 minute target-to-background (T/B) ^{64}Cu-ATSM SUV ratio was 2.03 ± 0.18.

Table 2 Summary of ^{64}Cu-ATSM PET/MR detection of plaques in the carotid artery and vertebral artery of the patients. "+" stands for positive detection in the corresponding image modality, while "-" stands for a negative imaging result.

Patient #	**Carotid artery**				**Vertebral artery**			
	Left		Right		Left		Right	
	MR	PET	MR	PET	MR	PET	MR	PET
1	-	-	+	-	+	+	-	-
4	+	-	+	-	+	+	-	-
5	-	-	+ (little)	-	+	+	+	+
6	-	-	-	-	+	-	(blurred)	-
7	+	+	-	-	+	-	-	-
8	+	+	-	-	+	-	-	-

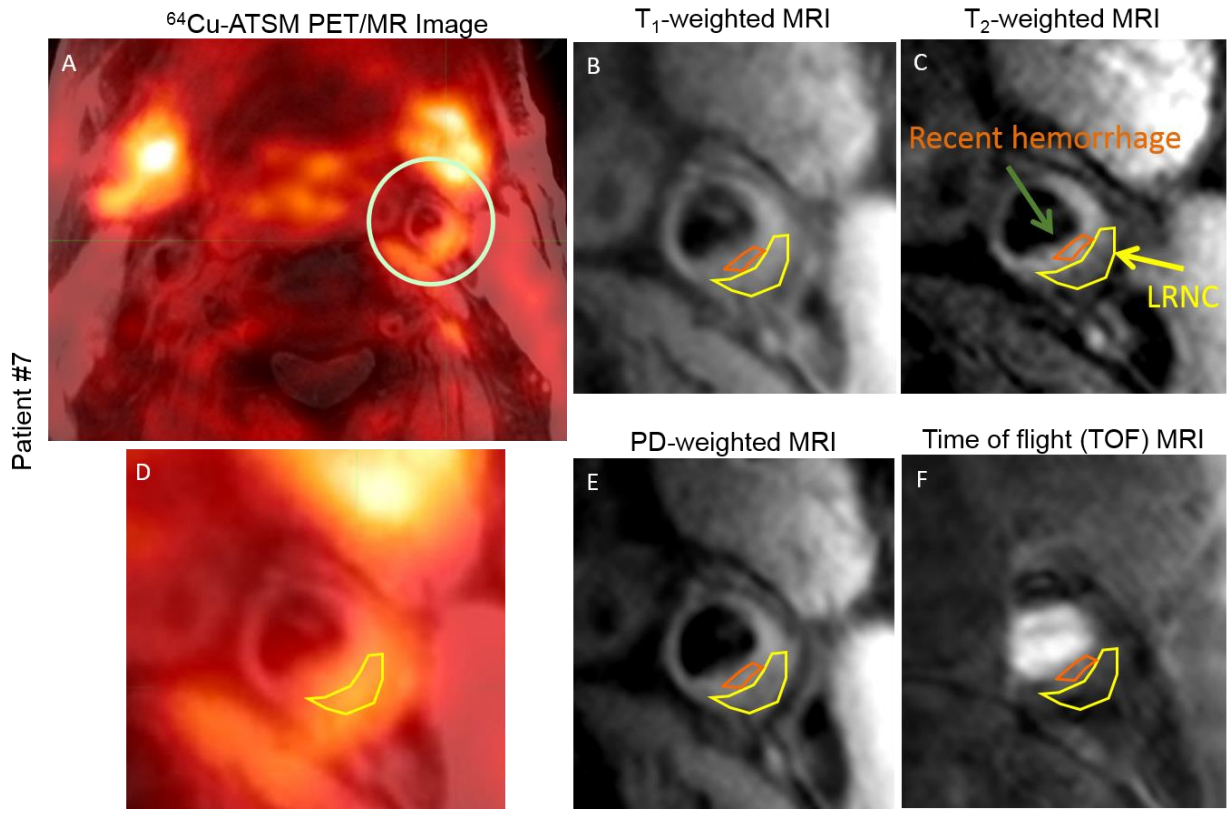

Figure 30 ^{64}Cu-ATSM uptake in lipid-rich necrotic core (LRNC) of the plaque in the left carotid artery as shown in the transverse view of (A) ^{64}Cu-ATSM PET/T_1-weighted MR image and (D) zoomed-in PET/MR image with the region of interest in the carotid artery of a representative patient. Plaque components of LRNC and recent hemorrhage were visible in the corresponding (B) T_1-weighted MRI, (C) T_2-weighted MRI, (D) PD-weighted MRI, (F) Time of flight MRI.

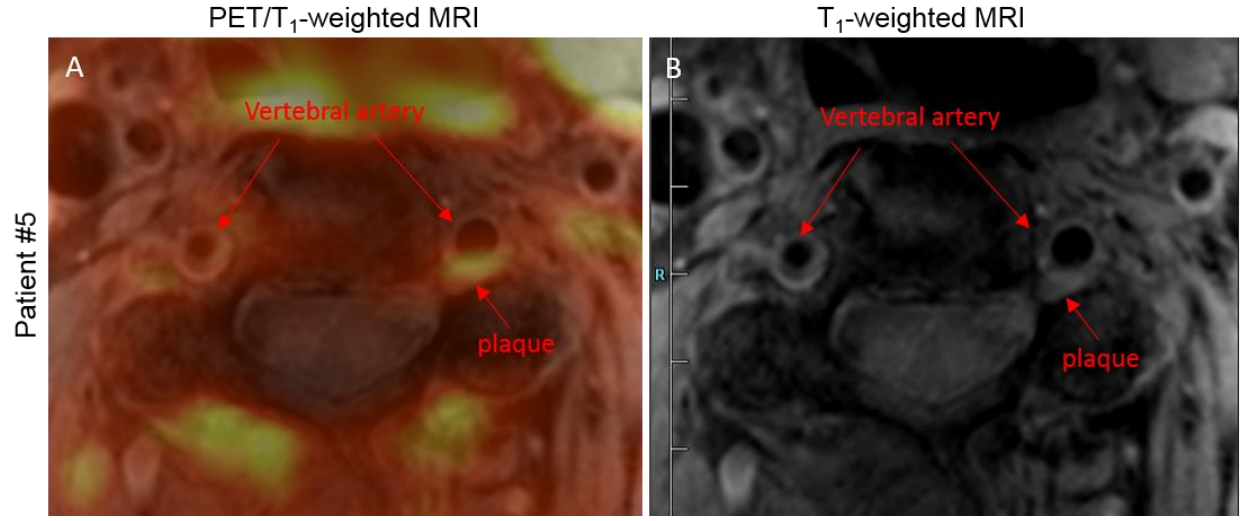

Figure 31 ^{64}Cu-ATSM uptake in plaques of vertebral artery as shown in the transverse view of (A) ^{64}Cu-ATSM PET/T_1-weighted MR images and (B) T_1-weighted MR images of a representative patient.

DCE MR imaging exhibited an initial and abrupt increase in signal intensity (contrast agent concentration) in the jugular vein after contrast material administration, while the signal intensity in the internal carotid artery was roughly a continued slower rise (Fig 32). Contrast agent concentration–time curve for each pixel in the region of interests that included the carotid plaques and surrounding tissues were plotted by curve fitting the Patlak model (Fig. 33). The RFE to fit this pharmacokinetic model was 28.6% ± 7.9% which was comparable to the values reported in literature *(4)*. Qualitative evaluation of K^{trans} map showed that the highest K^{trans} values were at the rims of carotid plaque (Fig. 34). This finding was consistent with literature that the necrotic core exhibited low K^{trans} values at center of plaque, while the highly vascularized adventitia at the outer rim and the region near inner rim of the plaque have high K^{trans} values (4).

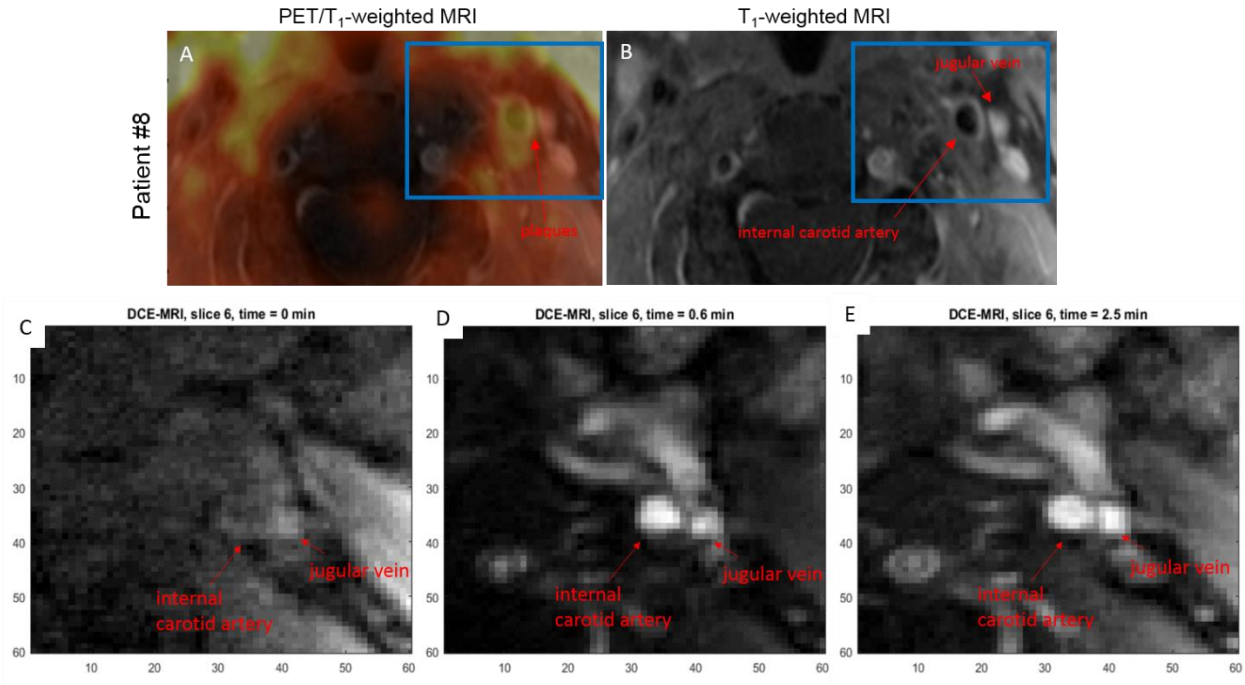

Figure 32 Representative DCE-MR images of one patient with ^{64}Cu-ATSM uptake in internal carotid artery plaque. (A) PET/T1-weighted MR image, (B) T1-weighted MR image.DCE-MR images (*157*) (targeting the region in images A and B identified by the blue box) (C) before contrast material administration, (D) 0.6 minutes after injection (bolus arrival), and (E) 2.5 minutes after injection, respectively

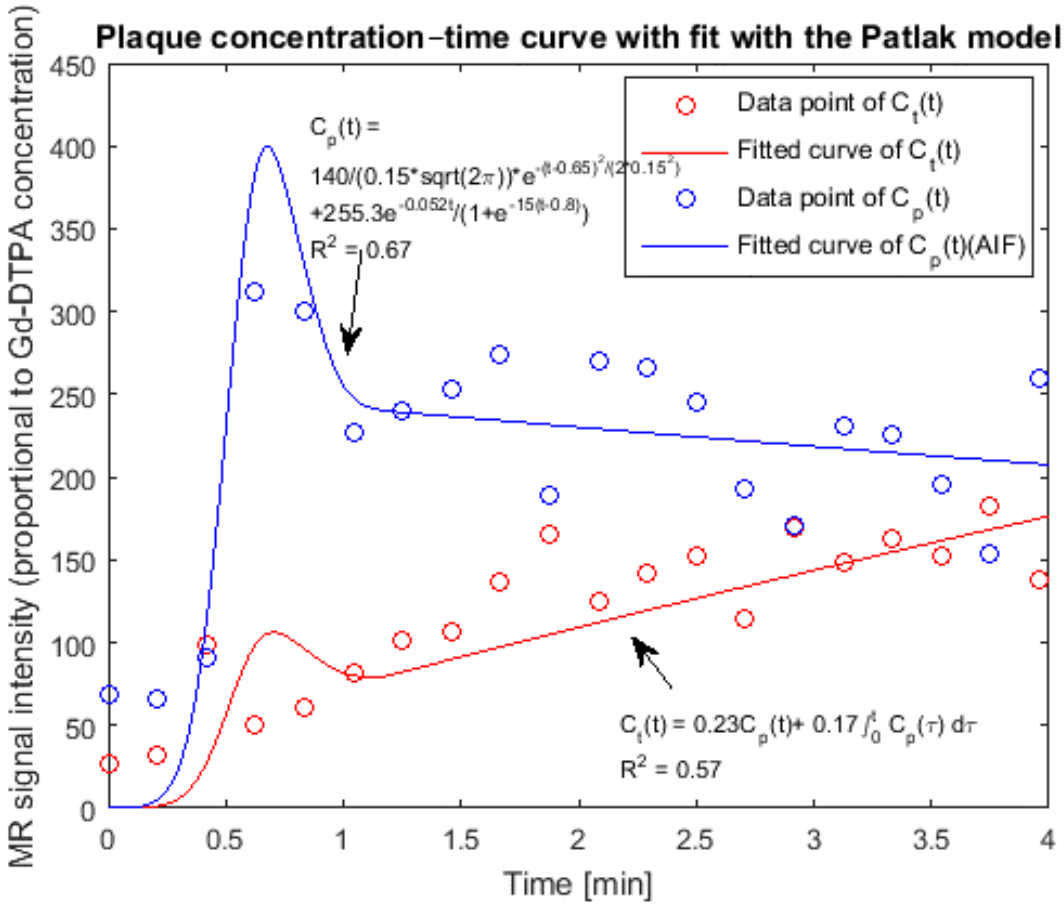

Figure 33 Plaque concentration–time curve fit to the Patlak model. AIF (C_p) concentration-time curves were fit using a slightly adapted formula introduced by Parker et al (*155*). Mean parameters used to construct the general VIF were as follows: scaling constant of Gaussian = 140 SI· min, center of Gaussian = 0.65 minutes, width of Gaussian = 0.15 minutes, amplitude = 255.3 SI, decay constant = 0.052 min^{-1}, width of sigmoid = 15 min^{-1}, and center of sigmoid = 0.8 minutes. SI = MR signal intensity which was assumed to be proportional to contrast agent (Gd-DTPA) concentration in mmol.

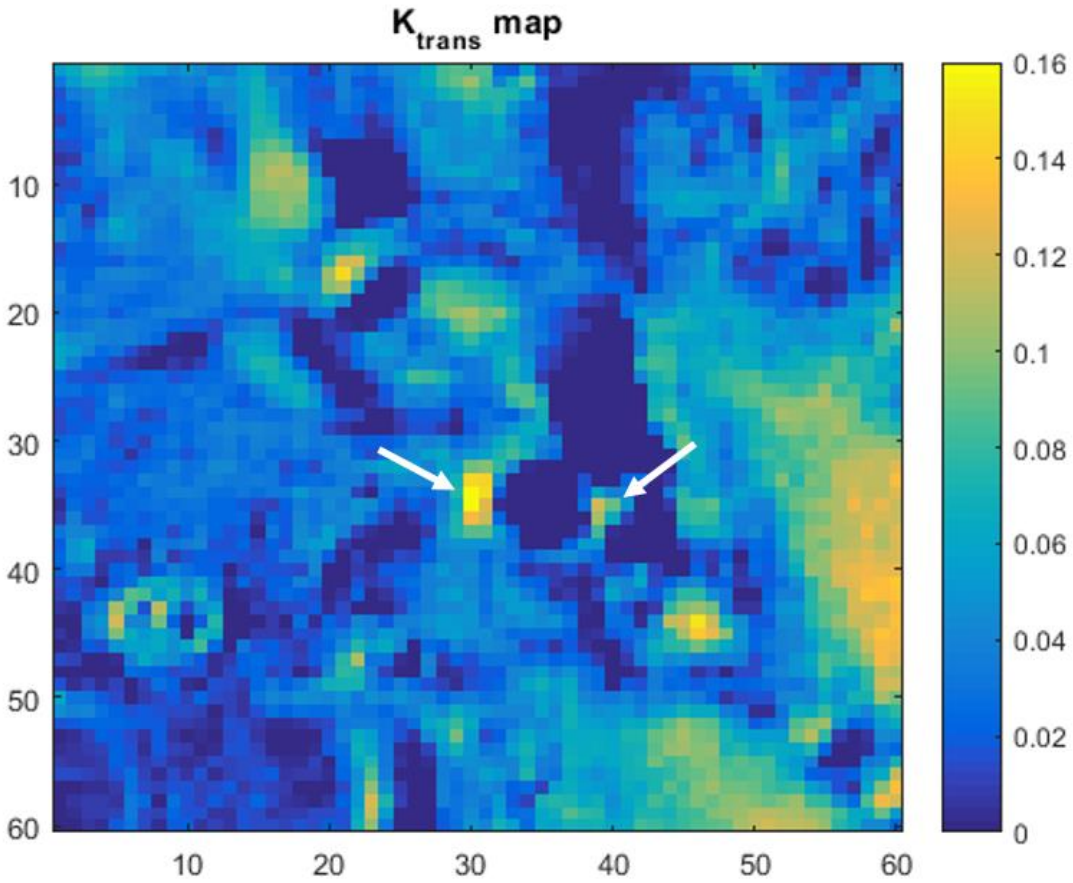

Figure 34 K^{trans} parametric map. Voxel-wise determined K^{trans} values are color encoded from 0 to 0.16 min^{-1}. Highest K^{trans} values (white arrows) were observed at the outer rim of the carotid plaque.

No positive IHC stains of PIMO or HIF-1α/macrophage were found in the collected carotid endarterectomy specimen, and the results could be treated as a negative control. However, we were able to co-localize HIF-1α and CD68 using an ex vivo CEA specimen from a different study in which the patient was not administered with PIMO (Fig. 35), suggesting the presence of hypoxic macrophages in human carotid atherosclerosis.

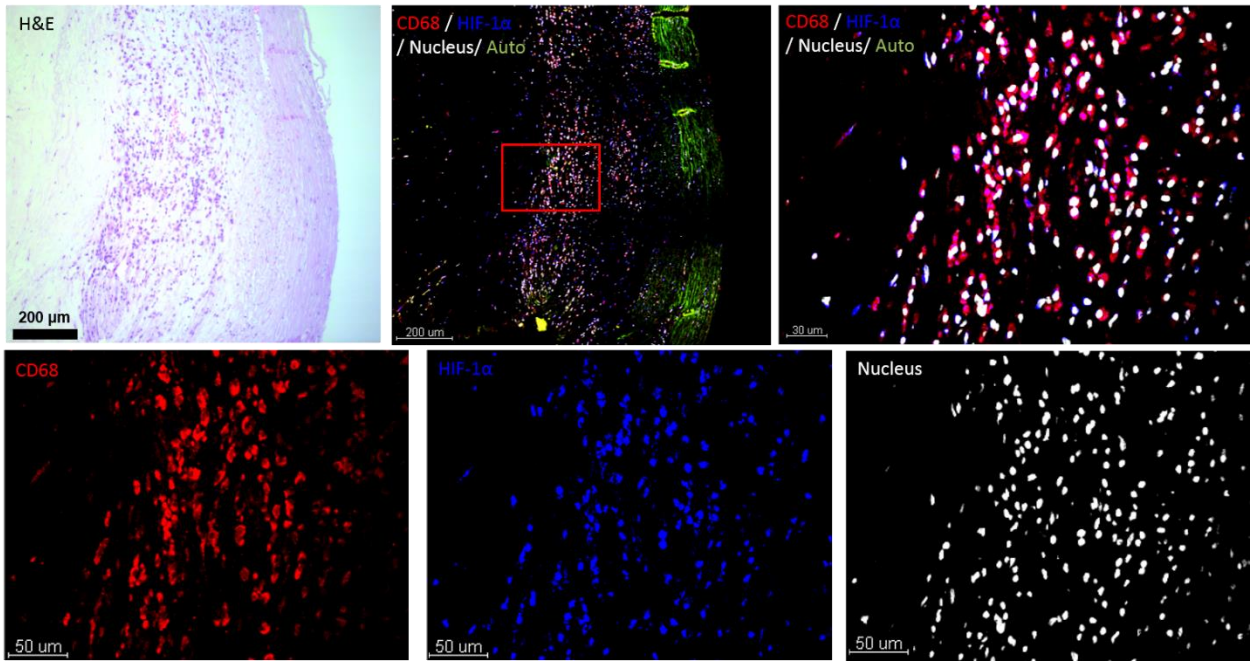

Figure 35 IHC results of a CEA specimen from a patient who did not receive PIMO. H&E staining shows white blood cell present in the deep intima of the plaque specimen. CD68 (identifying macrophages) and HIF-1α (identifying hypoxic cells) are co-localized as shown in the co-registered image (top line, middle), and the zoomed in figure (top row, middle and right) with the focus of interest in the red square. The zoomed in figures of individual stains of CD68, HIF-1α and nulceus are displayed in the bottom row.

3.3.3 ^{64}Cu-ATSM patient study: discussion

In this pilot clinical trial, we were able to obtain good quality analyzable ^{64}Cu-ATSM PET/MR imaging data sets from 6 asymptomatic patients with carotid atherosclerosis. A 2-fold target-to-background SUV ratio was observed in the patients with ^{64}Cu-ATSM uptake in carotid plaques and/or vertebral plaques. IHC staining with PIMO and HIF-1α were each negative in the carotid endarterectomy specimen we were able to obtain from one of our patients with PET/MR imaging. This result is expected given that this CEA specimen was obtained from a patient (patient #1) without ^{64}Cu-ATSM carotid uptake on PET imaging. The team will continue to recruit more patients upon receipt of additional funding in an attempt to collect more data to reach statistically significant conclusions.

DCE-MR imaging performed on two of the patients allowed study of the microcirculation of carotid plaques (*158*). The high rate of oxygen consumption by plaque macrophages causes hypoxia within the plaque, which triggers the increase of plaque microvasculature (*26*). Abundant microvasculature has been identified as an important aspect contributing to plaque vulnerability (*159, 160*). Although the microvasculature in plaques are very small (up to ~100 μm in diameter), the microvessel density and permeability are able to be determined noninvasively by DCE-MRI (*161-164*). In recent years, a number of studies have applied DCE-MRI to study atherosclerotic plaque microvasculature in animals (*165-167*) and patients (*168-172*). Kerwin and colleagues (*161-163*) performed several DCE-MRI studies in carotid atherosclerotic plaques and showed correlations between K^{trans} and microvessel density and macrophage content. A typical DCE-MRI experiment to study atherosclerotic plaque microvasculature consists of repeated imaging with a rapid T_1-weighted sequence to measure changes in signal intensity as a bolus of low molecular weight non-specific Gadolinium-based contrast material is intravenously injected and diffuses into the tissue. The distribution of contrast medium results in signal enhancement of the blood vessel lumen, vessel wall due to leakage of the contrast medium through damaged endothelial, and other tissues, such as skeletal muscle (*149*). The signal enhancement in the vessel wall depends on flow, microvascular density, the ability of the contrast medium to leak from the microvasculature into the extravascular extracellular space, and reflux. After analysis of the resulting DCE-MR images, pharmacokinetic parameters that are related to the local leaky plaque microvasculature can be calculated.

The quantification of contrast medium distribution over a tissue of interest can be assessed by pharmacokinetic modeling, with the main advantage of deriving parameters of the in vivo physical quantities of the amount, flow, and leakiness of the microvasculature (*173*). A number of

quantitative DCE-MRI models have been proposed in the evaluation of atherosclerotic plaque microvasculature (Table 3). These pharmacokinetic models all describe the relationship between the concentration of the (extracellular) contrast medium in the blood plasma (C_p) and the extracellular extravascular space (C_e) according to the two-compartment model (Fig. 32) and using the parameters K^{trans}, and/or v_e and/or v_p. K^{trans}, the transfer constant of contrast medium from plasma to the tissue compartment, plays as an indicator of blood supply and vessel permeability within the atherosclerotic tissue. The parameters v_e and v_p represent the extravascular extracellular space and the plasma fractional volume, respectively (Table 4). The modified/extended Tofts model is a commonly employed analytical solution for the two-compartment model, estimating all three pharmacokinetic parameters (K^{trans}, v_e and v_p) (*156, 174*). The original Tofts model, which was proposed for the study of multiple sclerosis (*175*), does not take vascular contribution into account (i.e., v_p is assumed to be negligible). The Patlak model assumes that reflux, i.e., transfer of contrast medium from the tissue compartment back to the blood plasma (K^{trans}/v_e), is negligible (*176*). The extended graphical model was introduced as an intermediate solution between the modified Tofts and the Patlak model (*177*). This model uses the first-order term of a Taylor series from the modified Tofts model to estimate v_e.

The Patlak model chosen in our study to quantified contrast agent dynamics for DCE-MRI was found to be most suited for describing carotid plaque enhancement among these four pharmacokinetic models in terms of reproducibility, fit error, parameter uncertainty, and correlation with histology of carotid plaque (*178*). The Parker formula applied to estimate C_p uses a mixture of two Gaussian functions that was able describe the first and second pass peak of contrast material. The vascular input function (VIF) in this formula was created from the DEC-MR images of each patient. However, a generalized VIF, which is obtained from a separate study

cohort where acquisition is performed with a higher temporal resolution and a lower spatial resolution (*173*), is the most commonly chosen method in clinical studies of atherosclerotic plaque microvasculature. Moreover, there are a lot of undermined parameters in the Parker formula which are subject to estimation on a case-by-case basis.

We applied a slower injection rate of contrast agent (0.5 ml/s). This is different from DCE-MRI studies of brain and tumor perfusion that mostly use a contrast medium injection rate of 2 ml/s (typically 0.1 mmol/kg) because a high injection rate is most beneficial for high K^{trans} values (> 0.2 min^{-1}) (*179*) while typically the mean K^{trans} values are below 0.15 min^{-1} (*180*) within the atherosclerotic lesion, which is consistent with our own measurement.

Table 3 Overview of pharmacokinetic two-compartment model and model solutions (*173*).

	Mathematic Description	Parameters		
Two-compartment model	$\frac{dC_e(t)}{dt} = \frac{K_{trans}}{V_e}\left[C_p(t) - C_e(t)\right]$ $C_t(t) = v_p C_p(t) + v_e C_e(t)$			
Model solutions		K^{trans}	v_e	v_p
Tofts (*156*, *174*)	$C_t(t) = K^{trans}\int_0^t C_p(\tau)\cdot e^{-(\frac{K^{trans}}{v_e})(t-\tau)}d\tau$	×	×	
Modified/extended Tofts (*156*, *174*)	$C_t(t) = v_p C_p(\mathrm{t}) + K^{trans}\int_0^t C_p(\tau)\cdot e^{-(\frac{K^{trans}}{v_e})(t-\tau)}d\tau$	×	×	×
Patlak (*176*)	$C_t(t) = v_p C_p(t) + K_{trans}\int_0^t C_p(\tau)\,d\tau$	×		×
Extended Graphical (*177*)	$C_t(t) = v_p C_p(\mathrm{t}) + K^{trans}\int_0^t C_p(\tau)d\tau -$ $\frac{K^{trans^2}}{v_e}\int_0^t\int_0^{\tau_1} C_p(\tau_2)d\tau_2 d\tau_1$	×	×	×

Table 4 Description of the parameters used in DCE-MRI pharmacokinetic models (*173*).

Quantity	Definition	Unit
$C_p(t)$	Blood plasma concentration of Gd-DTPA as a function of time (Jugular vein was chosen)	HU or mM
$C_e(t)$	Extracellular extravascular space (EES) concentration of Gd-DTPA as a function of time	HU or mM
$C_t(t)$	Tissue concentration of Gd-DTPA as a function of time	HU or mM
K^{trans}	Transfer constant from the blood plasma into the EES	mL/g/min
K_{ep}	Transfer constant from the EES back to the blood plasma	1/min
t	Onset time of arterial contrast uptake	sec
v_p	Blood plasma volume per unit of tissue	mL/g
v_e	Total EES volume ($v_e = K^{trans}/K_{ep}$) per unit of tissue	mL/g

The most widely used DCE-MRI pharmacokinetic parameter is the transfer constant K^{trans} that describes the relationship between the arterial input function (C_p) and increasing contrast concentration in tissue (C_t). Put simply, K^{trans} provides a quantitative measurement of enhancement and is limited by either the vascular blood flow or permeability (*158*). As mentioned in Chapter 2, in atherosclerotic plaques, hypoxia-induced increases in VEGF may contribute to the development of unstable lesions by promoting angiogenesis (*26*). Hypoxia continually up-regulate this HIF-1-regulated angiogenic factor, VEGF, to meet metabolic demands; however, the angiogenic vessels are structurally defective and fail to support adequate blood supply that further worsens local hypoxia, ensuring a vicious cycle (*59*). The overexpression of VEGF leads to leaky vasculature and high vessel permeability, facilitating both intravasation and extravastion of Gd-DTPA contrast agent. Significant positive correlations were found between K^{trans} and the endothelial microvessel content determined on histologic studies (*149*). Therefore, the (leakage) volume transfer constant K^{trans} used for quantifying neovascularization, together with the ^{64}Cu-ATSM image to identify

hypoxic plaques, is a promising method to diagnose and predict patients with vulnerable plaques who might be benefit from taking the risk of more aggressive treatments for carotid atherosclerosis (e.g. carotid endarterectomy). Truijman et al (*172*) demonstrated that there is a weak but significant positive correlation between inflammation on ^{18}F-FDG PET/CT and neovascularization (K^{trans}) as assessed with DCE-MRI. Wang et al further showed that the correlation between ^{18}F-FDG PET uptake and K^{trans} varied with clinical conditions, pointing to a complex interplay between macrophages and neovessels under different pathophysiological conditions. Nevertheless, as the ^{64}Cu-ATSM PET and DCE-MR imaging modalities are not interchangeable, the combination may increase the chance to predict the vulnerability of plaques.

There are some limitations in our ^{64}Cu-ATSM PET/MR imaging study of carotid atherosclerotic patients. First, it was difficult to recruit enough patients for this clinical trial. Although we initially recruited up to 20 patients, only 7 of them eventually agreed to complete the scanning, of whom 6 had acceptable image quality, two performed DCE-MRI scanning, and only one underwent carotid endarterectomy (CEA; different from the ones who underwent DEC-MRI), because only symptomatic patients with severe ipsilateral stenosis is more likely to have developed advanced atherosclerosis plaques and may benefit the most from CEA (*181*). Therefore, we were unable to collect enough data and from either the PET/MR images or the IHC stains to demonstrate our hypothesis on a statistically significant level.

Future plans for the remainder of the research team is to continue to recruit patients with carotid atherosclerosis scheduled for carotid endarterectomy into this trial. , We will measure and compare the SUVs of plaques and plaque-to-background SUV ratios on ^{64}Cu-ATSM PET images of the patients with and without atherosclerosis visualized on MRI. Common carotid images from the mandibular angle to the base of the neck will be presented to a single blinded reader who will

grade transverse images of the carotids at each 4 mm interval for the presence or absence of atherosclerosis. If atherosclerosis is present on that image, the reader will grade the presence or absence of lipid core and presence or absence of hemorrhage and correlate the findings to ^{64}Cu-ATSM uptake.

IHC staining serve as a "gold standard" to support any of our conclusions regarding ^{64}Cu-ATSM uptake and K^{trans} values about human carotid atherosclerosis. We will need to collect at least 3 carotid endarterectomy specimens that all show ^{64}Cu-ATSM uptake as well as positive PIMO and macrophage staining results. The correlation between K^{trans} values with histologic findings will be investigated as well once we have enough patients undertake DEC-MR imaging. For further studies, the CEA specimen will also be treated with HIF-2α, VEGF, hematoxylin and eosin (H&E) and/or Verhoeff Van Gieson (VVG) stains. The immunoreactivity for hypoxia in the plaques as well as HIF-1α,-HIF-2α, VEGF and CD68 will be scored by one observer, a histopathologist, on a scale from 0-3, with 0 = none; 1= mild; 2 = moderate and 3 = extensive. H&E and VVG-stained specimens will be used to grade plaque severity using the American Heart Association (AHA) classification for atherosclerosis (*109*). Sections will be graded by a separate observer, a vascular biologist, blinded to the IHC. Briefly, AHA grades for atherosclerosis disease progression are I) intimal thickening, II) fatty streak, III) preatheroma, IV) atheroma, V) fibroatheroma, and IV) complicated lesion due to fissure, hemorrhage, or thrombus. Then we will be able to investigate the uptake of ^{64}Cu-ATSM on the plaque component and severity level.

The ultimate goal of this clinical trial is to make ^{64}Cu-ATSM PET/MR imaging an FDA approved standard of care for diagnosing vulnerable carotid atherosclerosis, in order to aid physicians in determining whether the patient will benefit from the more risky carotid endarterectomy surgery.

Chapter 4: Improving ^{64}Cu-ATSM PET image quality

In this chapter, we will discuss the strategies we have employed to improve the ^{64}Cu-ATSM PET image quality via correction for partial volume effects using Siemens HD PET software during image reconstruction and post-reconstruction image processing techniques. We also evaluated the accuracy of attenuation correction effects from the carotid surface coils and the thermoplastic holder.

4.1 Correction for partial volume effects

The partial volume effects (PVE) originally referred to the loss of signal for structures partially occupying the PSF of the scanner (*142, 182*). PVEs now usually incorporate both spill-out and spill-in effects. The loss of signal in the object will be distributed across adjacent voxels, which are considered outside the object, resulting in increase in signal in these voxels (spill-out effects). The reciprocal effect of poor spatial resolution is the contamination of signal from neighboring tissue or spill-in effects (*182, 183*). PVEs in MR or CT are typically meant by blurred anatomical details smaller than the chosen pixel size, while the dominant PVE cause in PET usually refers to that anatomical details smaller than 3 times the FWHM of the PSF appear smeared out. In quantitative studies of PET images, PVEs introduce distortions both in the targeted region and in adjacent tissue, depending on tracer distribution (*184, 185*). As a result both the magnitude and the shape of the time activity curves (TACs) can be changed. An error of 50% was observed in estimated rate constants for metabolism and transfer of tracer between compartments (*186*).

In terms of PVEs in human carotid atherosclerosis PET imaging, the diameter of carotid arteries are on average 6 mm with atherosclerotic wall thickness of a few millimeters (*187*), we can expect

important PVE in the measurement accumulated ^{64}Cu-ATSM uptake to a particular plaque component (lipid/necrotic pool, fibrous cap, blood vessel wall, etc.).

In this section, I will discuss my work on partial volume effects correction (PVC) through applying the HD PET reconstruction software and implementing PVC techniques in the image space post image reconstruction.

4.1.1 Partial volume effects in PET

It is understood that the physical size width of the detection element (also known as crystal size) plays an important role in determining the spatial resolution in positron emission tomography (PET), while the combined contribution from acollinearity, positron range, decoding errors in the detector modules, and penetration into the detector ring often combine to be of similar size (*188-190*) (Fig. 36). The sampling geometry, which is also related to the crystal size, and statistical noise further degrade the effective resolution (*190*).

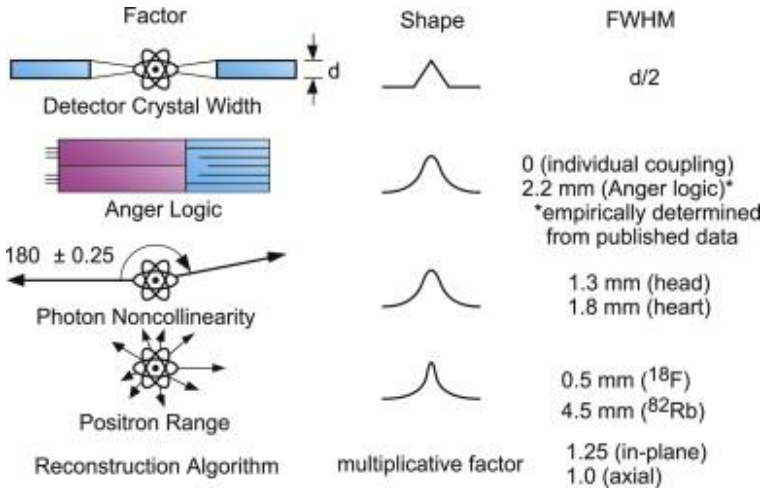

Figure 36 Diagrammatical and quantitative interpretation of the contributions to spatial resolution in PET. (Adapted from "Fundamental limits of spatial resolution in PET," by William W. Moses, 2010, NIMA_4th International Conference on Imaging techniques in Subatomic Physics, Astrophysics, Medicine, Biology and Industry, Volume 648(1), p S236-S240. Copyright (2010) by title of publisher.)

The empirical formula for the reconstructed spatial resolution Γ for a point source located at radius r from the center of the camera ring is given by

$$\Gamma = 1.25\sqrt{(d/2)^2 + s^2 + (0.0044R)^2 + b^2 + \frac{(12.5r)^2}{r^2+R^2}}, \quad (4)$$

where d is the crystal width, s is the positron range, b is the crystal decoding error factor (d/3 for detector designs that utilize optical decoding, zero otherwise) (*190*), and R is the detector ring radius. The factors in the quadrature sum in the above equation, going from left to right, are due to the detector size, the positron range, acollinearity, decoding error, and penetration, and the multiplicative factor of 1.25 is due to the reconstruction algorithm (*190*).

The "fundamental" effects can be reduced to detector width, positron range, and acollinearity through careful camera design. Thus, Γ for this "ultimate" design is given by:

$$\Gamma = \sqrt{\left(\frac{d}{2}\right)^2 + s^2 + (0.0044R)^2}\ (mm\ fwhm), \quad (5)$$

where d is the crystal width, s is the positron range, and R is the detector ring radius.

Accordingly, given the minimum mean positron range among the common positron emitting isotopes is 0.6 mm for ^{18}F, the fundamental limit for clinical and pre-clinical PET cameras will be 1.83mm FWHM and 0.67 mm FWHM, respectively. However, practically clinical and pre-clinical PET cameras can achieve 2.36 mm FWHM and 0.83 mm FWHM reconstructed spatial resolution, respectively (*190*).

The spatial resolution is usually characterized by the PSF, which essentially corresponds to the system response in accounting for all the "fundamental" effects to a point source. In general the PSF in PET images is spatially variant. The distribution of values depends on the location of the

source in the FOV of the scanner. However, it is reasonable to assume that the PSF is position-invariant (*191*) in the central portion of the scanner (~15-20 cm diameter). It is widely accepted that PET PSF can be approximated as an anisotropic 3D Gaussian function that is written as:

$$h(r) = \frac{1}{(2\pi)^{\frac{3}{2}}\sigma_x\sigma_y\sigma_z} exp\left(-\frac{1}{2}\left[\frac{x^2}{\sigma_x^2} + \frac{y^2}{\sigma_y^2} + \frac{z^2}{\sigma_z^2}\right]\right), \quad (6)$$

where $\sigma = [\sigma_x, \sigma_y, \sigma_z]$ is the standard deviation in the transverse, radial and axial directions. The PSF can be measured by fitting the Gaussian function of the PET image of a point radioactivity, and FWHM is related to the standard deviation as $\sigma = FWHM/2\sqrt{2\ln 2}$.

The reconstructed PET image can be viewed as a convolution of the true activity distribution with the PSF. The Fourier transform of the PSF, known as the modulation transfer function (MTF), contains the same information as the PSF. Therefore, a PET image can be described in the frequency domain as the product of the Fourier transform of the true activity distribution and the MTF of the system. This means that image components corresponding to mid-range frequencies, despite attenuation, may still be present in the data and could in principle be restored by an inverse filtering operation. Nevertheless, image components at higher frequencies will not be sufficiently sampled by the 4 mm-width PET detector crystals and therefore the MTF will be essentially zero. These image components will not be measured adequately and attempts to restore them usually lead to noise-amplification or image artifacts. Pre-clinical PET systems improves this limitation of clinical PET scanners with the use of smaller PET detector crystals and smaller ring radius.

An important intrinsic limitation in the PET application for the accuracy of quantitative studies is represented by the relatively poor spatial resolution of the scanner – leading to partial volume effects. The direct consequence of limited resolution is the loss of spectral signal for structures

partially occupying the PSF of the scanner (*142, 192*). If the dimensions of object or structures to be imaged is less than 3-4 times the instrument resolution (FWHW) of the imaging system, the resultant activity will be underestimated. Depression of apparent isotope concentration in an image for objects equal in size to the FWHM can be significant (*144, 183, 193*).

Once the PSF is known, it can be used to compensate for the PVEs, basically based on two different approaches: during reconstruction (*194-196*), in which approach the spatial resolution degradation is considered to originate at raw data level and deconvolution is achieved by incorporating PSF in the system matrix or equivalently by blurring each image estimate prior to forward projection during iterative image reconstruction (see section 4.1.2) or in the image space (*197, 198*), which assumes an effective resolution degradation happening at the image level (see section 4.1.3). Both methods can only approximate the actual resolution model due to the complexity of superposing several different effects. All PVC methods have limitations and can lead to noise-amplification or image artifacts, such as Gibbs artifacts (ringing in the vicinity of sharp boundaries). Because of the ill-conditioned nature of the restoration problem, some form of regularization is needed. Multiple regularization techniques are achieved by incorporating anatomical information and tissue homogeneity constraints. For example, Strul and Bendriem used an anatomically based PVC method that utilize structural information from other imaging modalities as a priori information to stabilize the solution (*199*). Wang and Fei (*200*) further developed an image-guided, voxel-based PVC method that correct PET images by iterative deconvolution withy an edge preserving smoothing constraint regularization. The constraint can restore discontinuities extracted from coregistered MR images but maintains the smoothness in radioactivity distribution.

4.1.2 PVC during image reconstruction

The PET list-mode data acquired from the Siemens PET/MR scanner can be reconstructed using the HD (High Definition) PET that relies on Point Spread Function corrected ordinary Poisson Ordered Subset Expectation Maximization (PSF-OSEM) reconstruction algorithm that incorporates a spatially invariant effective, image based, PSF in the reconstruction algorithm. HD has recently been introduced for the Siemens mMR. In summary, using measured PSFs, HD PET reduces blurring and distortion in the final image, therefore delivering superior detection of small lesions. It provides twice the signal-to-noise ratio (SNR) and near uniform spatial resolution throughout the FOV with 2 mm spatial resolution improvement (*201*), as compared to the usual > 4.5 mm spatial resolution in Siemens Biograph mMR PET/MR scanner (*202*).

4.1.2.1 PVC during image reconstruction: introduction

Generally, PET image reconstruction methods are divided to analytic methods, e.g. Filtered Back-Projection (FBP), and iterative methods, e.g. OSEM and maximum likelihood expectation maximization (ML-EM). FBP is a back-projected image after filtering of the sinogram. OSEM is developed for improving the disadvantages of ML-EM method (*203*), such as its long calculation time. The quality of OSEM image is superior to that of FBP images because iterative approaches can potentially increase the accuracy of images compared to analytic method although noise increases with an increasing number of iterations (*204-206*). Post-reconstruction imaging filtering methods, such as the popular Gaussian smoothing filtering, are used to reduced background noise and improve signal-to-noise ratio (SNR) of image with better contrast (*207*). However, Gaussian filtering also results in image distortion (*203*), depending on the size of filter. It will be necessary to compare various combinations of reconstruction algorithms with number of iterations and Gaussian filter size to investigate the optimal effective spatial resolution so as to make the most accurately quantitative analysis with the PET images.

Provided that the detection of each decay event by the PET system (photon pairs produced through annihilation of positrons emitted from the PET tracer) is independent and can be modelled as a Bernoulli process, the sinogram data can then be view as a collection of independent Poisson random variables and estimated by ML function that maximizes the probability of the observed data assuming no prior statistical model on the tracer distribution (*208*).

Let $\bar{\boldsymbol{y}} = \{\bar{y}_{i,} i = 1, \dots, M\}$ denote mean of the data, where *M* is the number of detector bins in the PET system. The relationship between $\bar{\boldsymbol{y}}$ and the unknown tracer distribution $f(x)$ is described as follows (*208*):

$$\bar{y}_{i,} = E[y_i] = \int f(x)c(i,x)\,\mathrm{d}x + r_i + s_i, \qquad i = 1, \dots, M \tag{7}$$

where $c(i,x)$ is the detection response function for the *i*th measurement or line of response (LOR), *r* and *s* represent the expectations of random events and scattered events, respectively.

Equation (7) can be approximated as the affine transform as follows (*208*):

$$\bar{\boldsymbol{y}} = E[\boldsymbol{y}] = \boldsymbol{P}\boldsymbol{f} + \boldsymbol{r} + \boldsymbol{s}, \tag{8}$$

where $\boldsymbol{P} \in \mathbb{R}^{M \times N}$ is the projection or system matrix. The element, $p_{ij} = \int c(i,x)\phi_j(x)\mathrm{d}x$, in which $\phi_j(x)$ denotes the *j*th voxel basis function, is the average probability of detecting an emission from voxel *j* at LOR *i*.

The conditional probability, or likelihood function, for the measured data, $\boldsymbol{y} = \{y_{i,} i = 1, \dots, M\}$, given the tracer distribution $\boldsymbol{f}$, is expressed as the independent Poisson distribution (*208*):

$$p(\boldsymbol{y}|\boldsymbol{f}) = \prod_i e^{-\bar{y}_i} \frac{\bar{y}_i^{y_i}}{y_i!}. \tag{9}$$

Since log is a monotonic function, the ML estimates of $\boldsymbol{f}$ can be computed by maximizing either Equation (9) or the log of the likelihood function, defined as (*208*):

$$L(\boldsymbol{y}|\boldsymbol{f}) = \sum_{i=1}^{M} y_i \log(\overline{y_i}) - \overline{y_i} - \log(\overline{y_i}!). \quad (10)$$

The solution of the ML estimate is expressed as (*209, 210*):

$$f_j^{k+1} = f_j^k \cdot \frac{1}{\sum_i p_{i,j}} \sum_i \left[p_{i,j} \cdot \frac{y_i}{\sum_i p_{i,j} \cdot f_j^k + r_i + s_i} \right], \quad (11)$$

where f_j^{k+1} and f_j^k are the updated and old images voxel j.

When EM iterative image reconstruction is accelerated through updating the image using a subset of angles, it is then called ordered subset expectation–maximization (OSEM) algorithm or ordinary Poisson (OP)-OSEM algorithm (*211*). If system matrix is derived from point source measurement and the point spread function is incorporated into the system matrix for 3D PET reconstruction, OP-OSEM becomes PSF-OSEM (*196*).

Many statistically based 3D reconstruction methods are based on the EM or OSEM algorithm (*212*). Both approaches can exhibit high-variance behavior at high iteration numbers and are regularized through early termination of the algorithm or by subsequent smoothing of the reconstructed images (*191, 212*). A maximum *a posteriori* (MAP) formulation, which is used in small animal PET scanner for image reconstruction, controls the variance and resolution of the reconstruction through the regularizing influence of a smoothness prior (*191*). Therefore the MAP methods allow solutions with a low degree of variability between adjacent voxels, and prevent the instabilities at higher iterations encountered using EM and OSEM (*212*). The MAP solution can be computed using a 3D extension of the pre-conditioned conjugate gradient algorithm (*213*).

4.1.2.2 Evaluation of effective spatial resolution: materials and methods

We used a phantom to evaluate the effective spatial resolution of HD PET (PSF-OSEM reconstruction algorithm), ordinary Poisson OSEM (OP-OSEM) reconstruction algorithm and the FBP reconstruction algorithm which was used as reference.

Thin-wall hot-spot spheres (diameter = 7.7, 9.8, 15.8 mm) in a cylindrical phantom that mimicked neck were filled with 6.3-times higher radioactivity (^{18}F-FDG) concentration than background (Fig. 37). The total volume of the spheres and the total volume outside the spheres in the cylindrical phantom were measured by weighting the correspond parts with and without water filling. Their activity ratio was calculate by multiplying their pseudo-concentrations (6.3 and 1, respective) by their measured volume, and the total activity (1 mCi ^{18}F) will be distributed accordingly. After mixing the activity with the measured volume of water, the diluted activity in correct radioactivity concentrations will be injected into the spheres and cylindrical phantom by a syringe.

The ratio radioactivity 6.3 was based on the average aortic arch-to-background SUV ratio of the ^{64}Cu-ATSM ApoE$^{-/-}$ mouse study. Circular ROIs were used to measure the spatial resolution.

Static PET/CT scanning was performed. Three PET image reconstruction schemes were performed using Siemens e7-tools: OP–OSEM), PSF–OSEM and FBP. The e7-tools is a research package provided by Siemens that allow the processing and reconstruction of Siemens PET emission data. It is identical to the reconstruction software on the Siemens mMR console. The reconstructed PET images with a dimension of 256×256×127 and a voxel size of 0.7×0.7×2.03 mm was interpolated to a dimension of 256×256×256 and a voxel size of 0.7×0.7×1.01.

For both OP-OSEM and PSF-OSEM, 16 subsets, 2-8 iterations, and 1-6 mm post-reconstruction Gaussian smoothing filtering was used.

Figure 37 Thin-wall hot-spot spheres (diameter = 7.7, 9.8, 15.8 mm) placed in a cylindrical phantom of ~10 cm in diameter.

The object function, O, was denoted by a digital mask created on MATLAB based on caliper's measurement of the phantom dimensions and the CT images. A digital representation of the phantom was created for which all pixels within the ROIs were assigned a value 6.3, elsewhere within the phantom 1, and 0 outside the phantom. The digital image was constructed with the same matrix size and voxel size as the object function as the CT image. The measured image I(x,y) is related to the object image O(x,y) by the PSF with:

$$I(x,y) = O(x,y) \otimes PSF(x,y), \tag{12}$$

where $\otimes$ indicates 2-dimentional convolution.

To measure PSF, each slice of the object and original image volumes was transformed by 2D Fourier transform, and data from corresponding slices of I was divided by O in the Fourier domain. The resulting data was inverse Fourier transformed to result in a PSF in physical space:

$$PSF(x,y) = F^{-1}\left[\frac{F[I]}{F[O]}\right], \tag{13}$$

where F indicates the 2D Fourier transform and F^{-1} indicates the inverse 2D Fourier transforms. Spatial resolution (FWHM) was characterized by fitting a 2D Gaussian function or 1D Gaussian funciton in x and y profiles to the the PSF image. The method was made particularly robust with respect ot noise by averaging the PSF images for all slices before performing the Gaussian fit. This approach not only reduced statistical noise but also effectively suppressed parallel line artifacts that occationally apeared in the PSF images due to dividing noisy data in Fourier space (*214*).

In order to validate the measurement PSF of the PET scanner, we created a simulated PET image by convolving the object function with a 3D Gaussian function using the measured FWHM and compared the recovery coefficients (RC) of hot spheres in original PET image with simulated PET images. RC was calculted by the following equation:

$$\text{RC (recovery coefficent)} = \frac{\text{Measured hot sphere} - \text{Measured back ground}}{\text{True hot sphere} - \text{True background}}. \quad (14)$$

4.1.2.3 Evaluation of effective spatial resolution: results

The quality to OSEM reconstructed PET images are superiors to that of FBP reconstructed PET images. The PSF-OSEM (HD PET) algorithm reconstructed PET images had improved spatial resolution, higher contrast and lower noise compared with the corresponding images obtained using the standard OP-OSEM algorithm and FBP algorithm (Fig. 38). PSF-OSEM performed a little better than OP-OSEM in term of its spatial resolution at the same number of iterations and Gaussian smoothing level. For both OSEM algorithms, the spatial resolution was improved with respect to increasing number of iterations and decreasing size of Gaussian smoothing filter. The optimal resolution was achieved with minimal post-filtering and maximal number of iterations. The measured spatial resolution of the PET scanner in Siemens PET/MR system with HD PET

reconstruction was consistent with literature (~4.3mm), but not as good as the valued claimed by the manufacturer (~3mm) (Fig. 39)

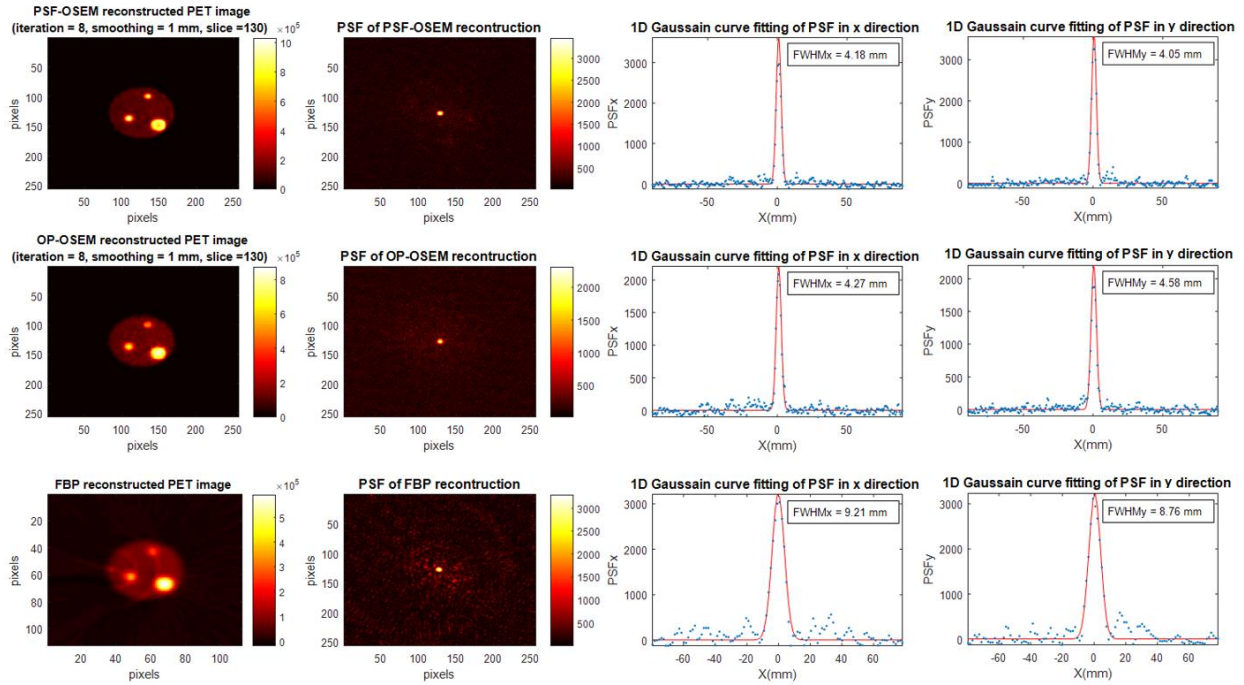

Figure 38 PET images reconstructioned by PSF-OSEM, OP-OSEM and FBP algorithms, the cerresponding averaged PSF images, and profiles through the PSF images showing the results of 1D Gaussian fits in x and y directions (red line).

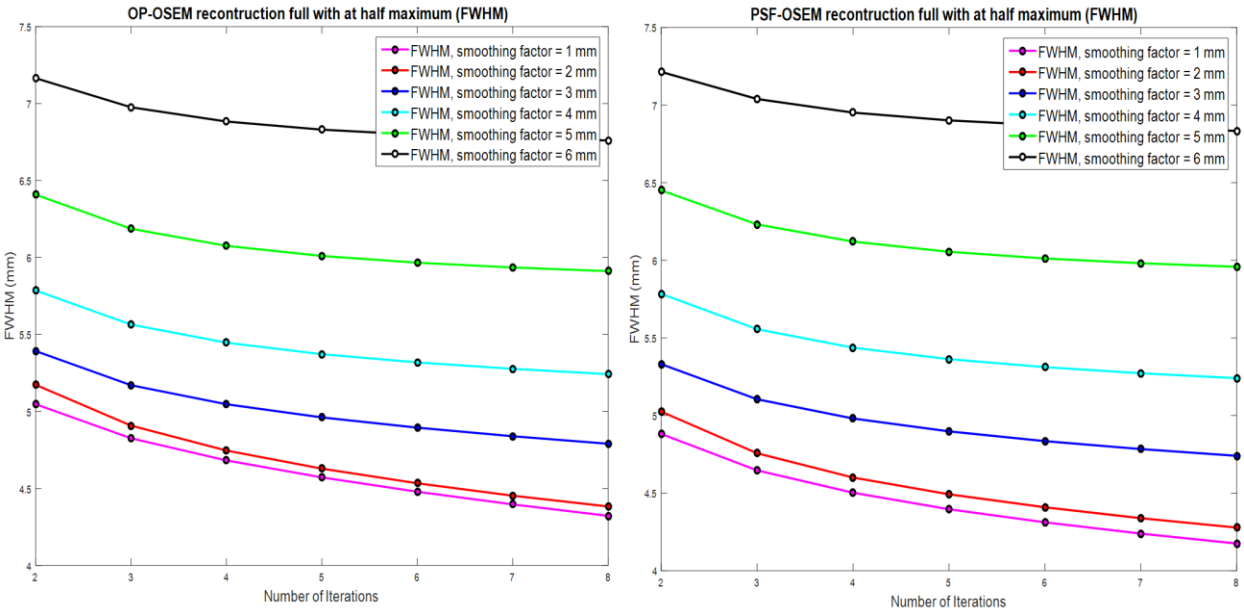

Figure 39 FWHMs of the PET images reconstructioned by PSF-OSEM and OP-OSEM algorithms using 2-8 iterations and 1-6 mm Gaussian smooting filtering. The smallest FWHM (best resolution) was observed at 8 iterations and 1 mm Gaussian smooting filtering for both reconstruction algorithms.

With acceptable differences, the signal intensity profile across spheres and recovery coefficients of spheres in the Gaussian kernel filtered digital mask matched with the PSF-OSEM and OP-OSEM reconstructed PET images, especially at higher iteration numbers, demonstrating that the results of this PET spatial resolution measurement is reasonable (Fig. 40, Fig. 41). The match is greater on smaller spheres using the PSF-OSEM reconstruction algorithm, while is greater on larger spheres using the OP-OSEM reconstruction algorithm. However, increasing the number of iterations resulted in longer processing time and, more importantly, increased noise. The balance between an optimal effective image resolution and an acceptable noise level was determined by practice.

We then investigated the relationship between image noise and number of iterations using PSF-OSEM reconstruction algorithm with different Gaussian smoothing filters. The noise level of image was calculated as the variance of the background. The plot demonstrated that image noise level is increased with respect to increased number of iterations and reduced Gaussian filtering size (Fig. 42). As a consequence, the spatial resolution of the reconstructed PET image and the recovery coefficients of the spherical objects were improved with increasing noise level (Fig. 43). However, at 8 iterations, the image quality has not been dramatically deteriorated by the noise, so can we will be benefit from selecting this number of iterations to achieve a higher effective spatial resolution.

(A)

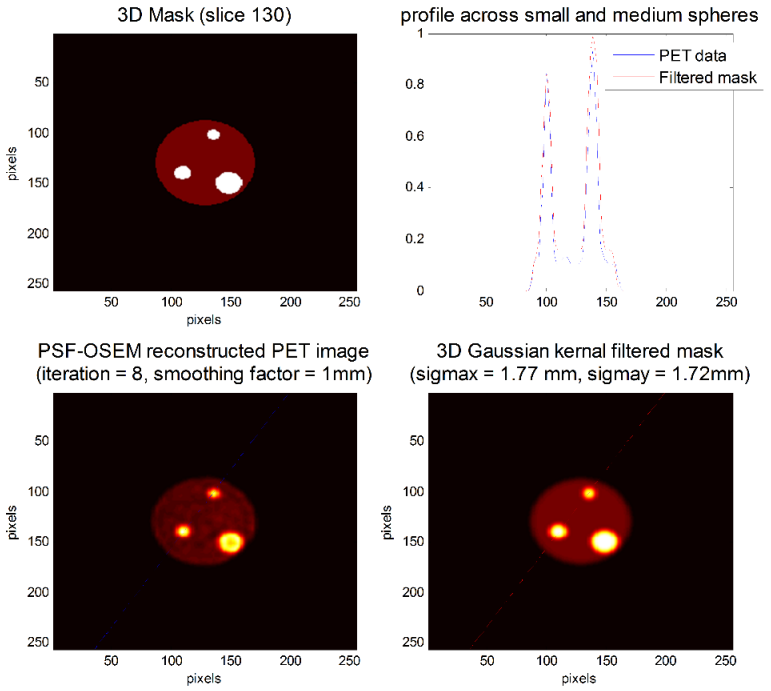

(B)

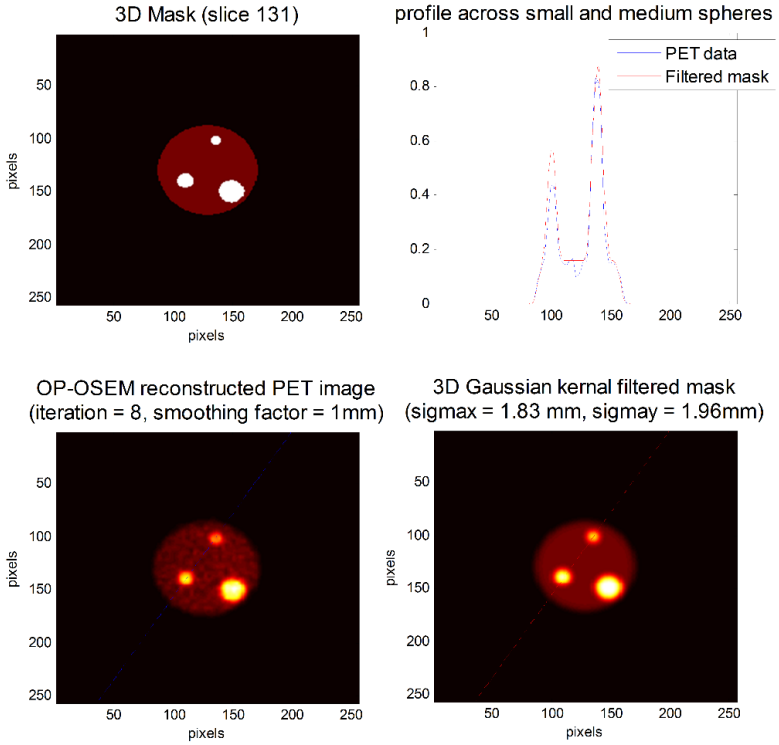

Figure 40 The transverse veiws of all three spheres on the 3D digital mask, (A) PSF-OSEM and (B) OP-OSEM reconstructed PET images using the combination of the reconstruction parameters that provided the best spatial resolution as measured, and the 3D Gaussian kernal filtered digital mask using the measured PSF of the correspongding reconstructed PET image. The signal intensity profile across the small and medium spheres on the PET image and Gaussian kernel filtered digital mask generally overlapped with acceptable differences.

(A)

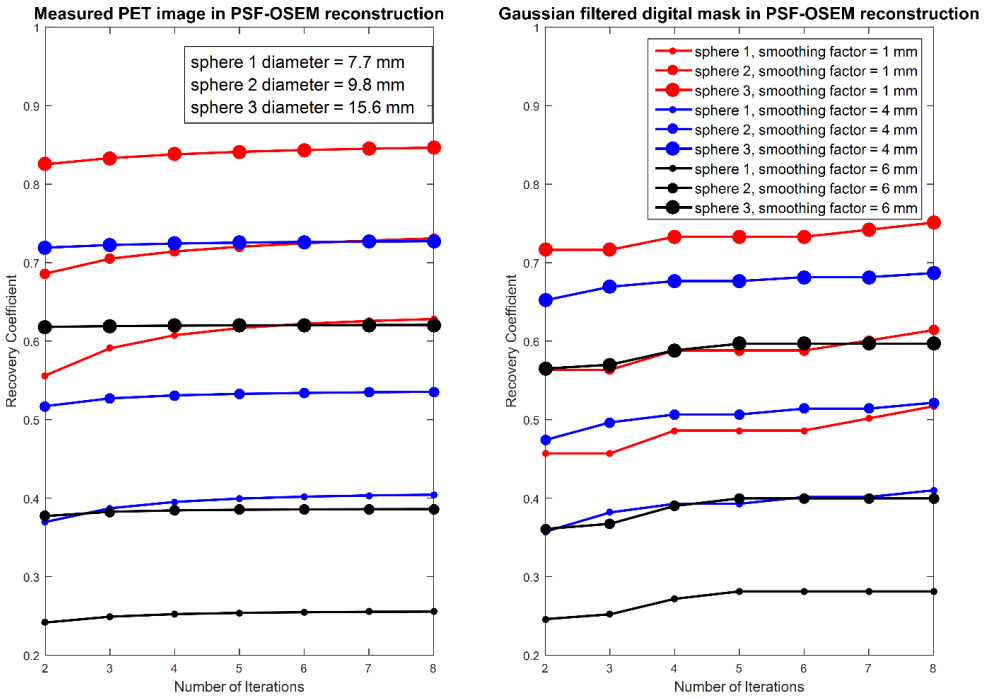

(B)

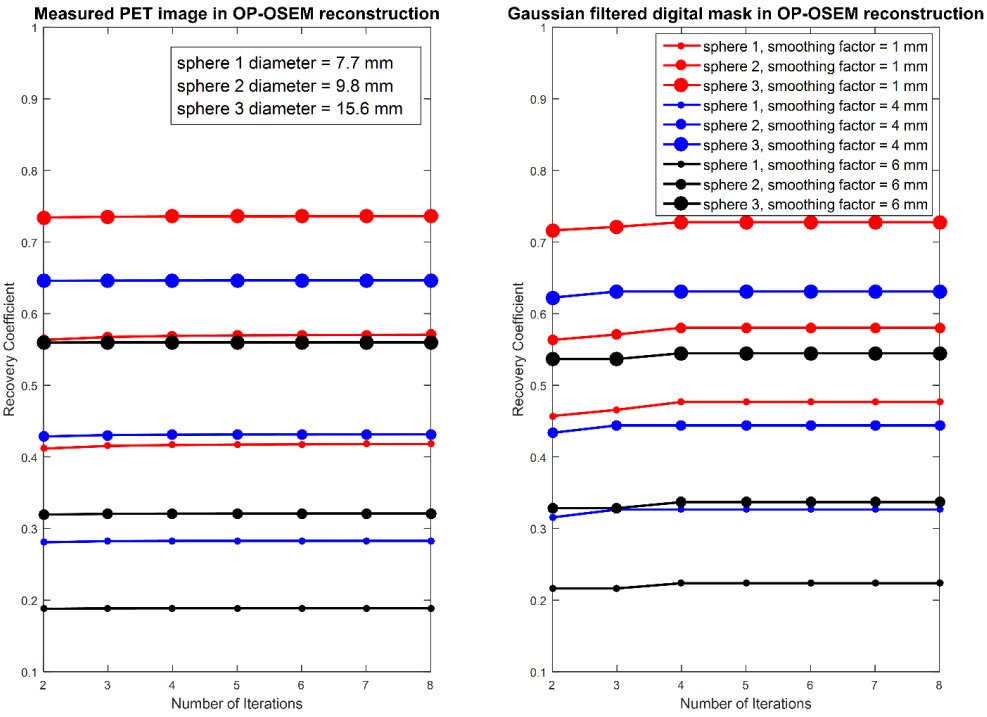

Figure 41 The recovery coefficients of the three spheres measured on the (A) PSF-OSEM and (B) OP-OSEM reconstructed PET images with various number of iterations and Gaussian smoothing filtering levels, and the 3D Gaussian kernal convoled digital mask using the measured PSF of the correspongding reconstructed PET image. The recovery coefficients of the PET image and Gaussian kernel filtered digital mask generally matched with acceptable differences, especially at higher iterations.

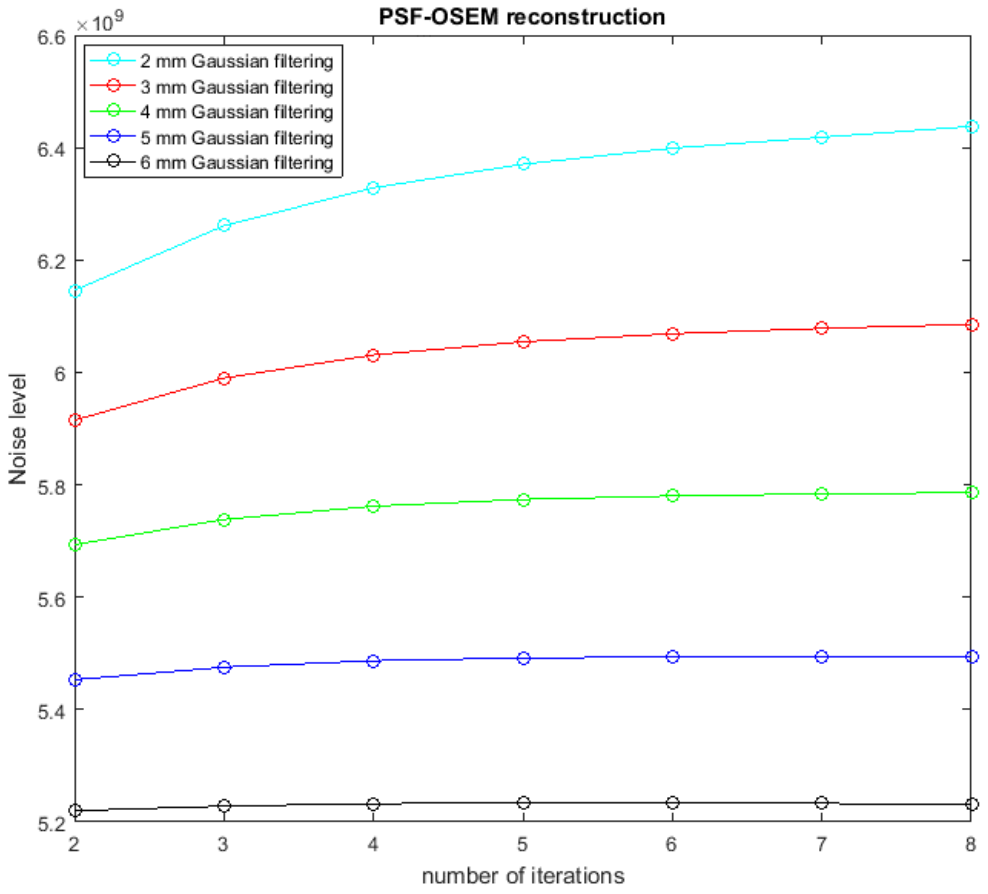

Figure 42 Relationship between image noise and number of iterations in PSF-OSEM reconstructed PET images using different Gaussian filtering.

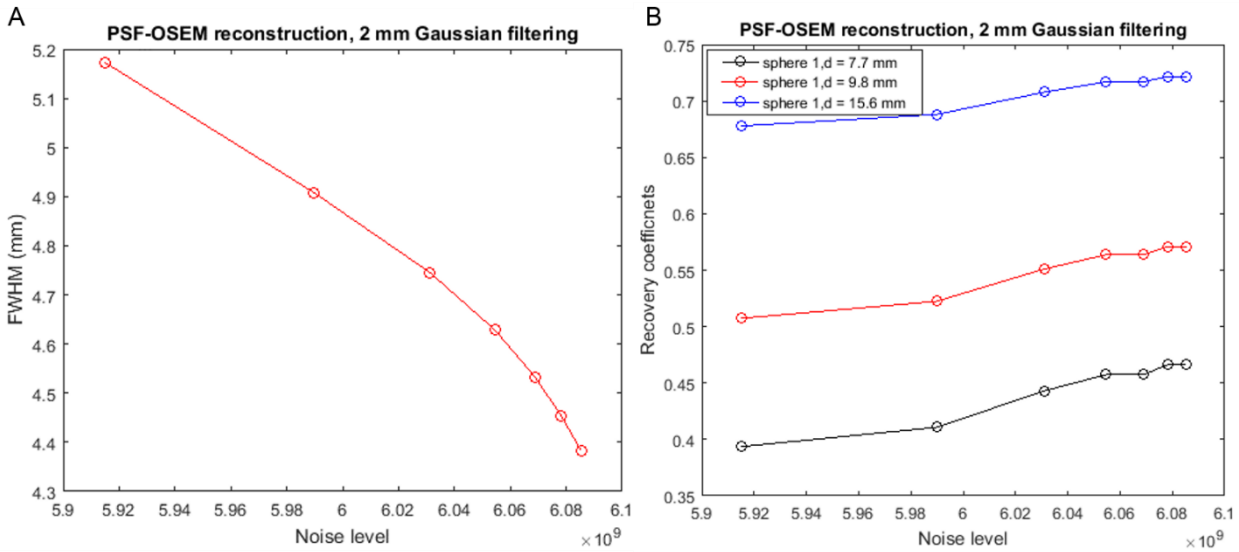

Figure 43 Relationship between (A) resolution (FWHM) and image noise, and (B) recovery coefficients of spheres in different sizes and noise in PSF-OSEM reconstructed PET images using 2 mm Gaussian filtering.

We investigated the effects of sphere-to-background radioactivity (^{18}F-FDG) ratios (contrast ratios), we compared the recovery coefficients of the thin-wall hot spheres with different sizes imaged with the Siemens small animal PET scanner and reconstructed using the MAP algorithm with the same Gaussian smoothing filtering but different number of iterations. It shows that when the contrast ratio is high enough, say greater than 6-to-1, the recovery coefficients are general the same for increasing contrast ratios. In high contrast ratios, the recovery of larger spheres (diameter > 4.8 mm) are equal for both 3 and 8 iterations, but the recovery coefficients of smaller spheres (diameter < 2.98 mm) using 8 iterations is higher than that using 3 iterations (Fig. 44).

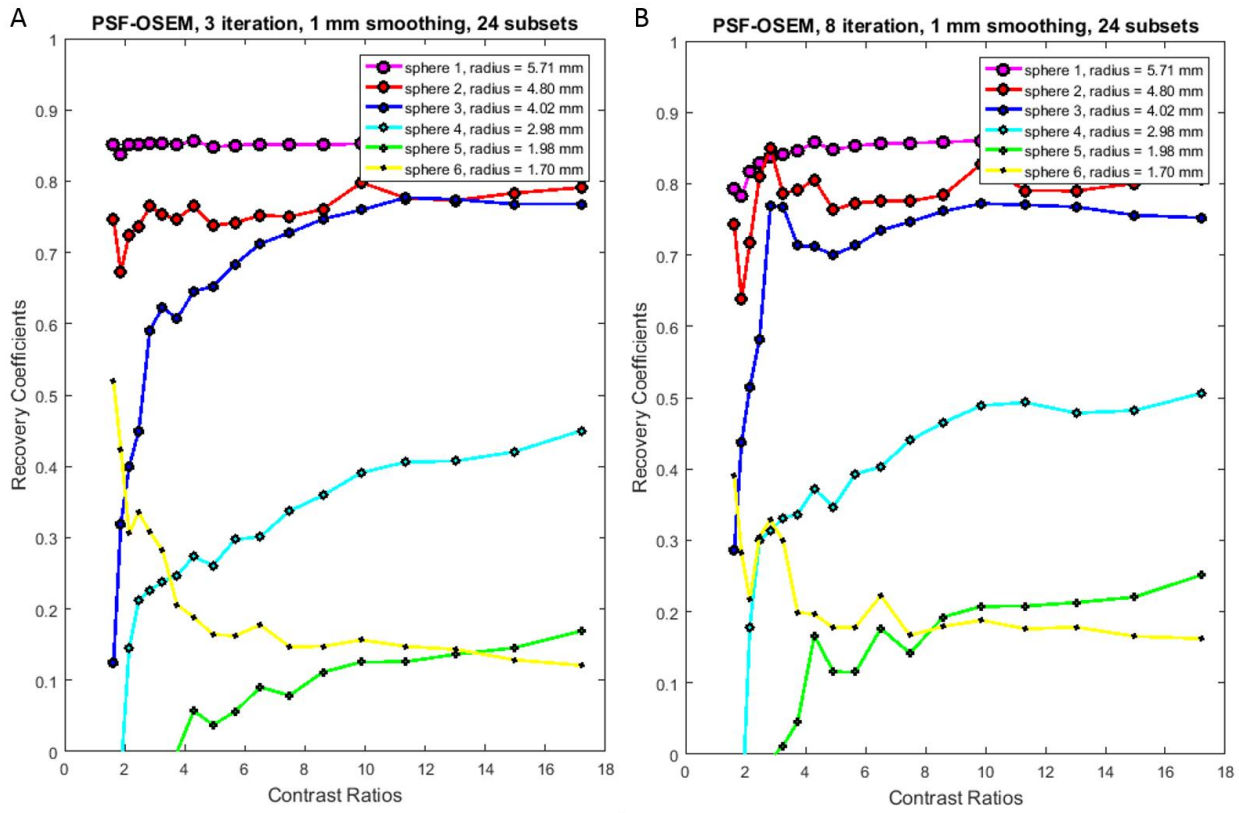

Figure 44 Recovery coefficients of spheres with different sizes versus sphere-to-background contrast ratios. List-mode PET data was acquired from ^{18}F-FDG PET imaging using the Siemens small animal PET scanner, and reconstructed using the PSF-OSEM algorithms with 1 mm Gaussian smoothing filtering, 24 subsets, and (A) 3 iterations, or (B) 8 iterations.

4.1.2.4 PVC during image reconstruction: discussion

The PSF-OSEM reconstruction algorithm that accounts for the PSF during image reconstruction works to improve the spatial resolution of PET images as compared to the OP-OSEM algorithm, however it did not achieve the manufacturer claimed resolution of ~3 mm. This might be attributed to that the PSF-OSEM algorithm can only partially corrected for PVEs, or the 3 mm optimal resolution was measured from a point source by the manufacturer, but we used distributed objects. Since the human carotid atherosclerosis are on the dimension of a few mm, they would still be dramatically affected by partial volume effects and further post-reconstruction partial volume correction might help.

Due to the loss of high frequency information in the object and the nonlinear nature of the reconstruction, PVEs are at best reduced in magnitude provided a sufficient number of iterations are performed, but quantitative recovery is not complete. Better results could be achieved with reconstruction algorithms involving anatomical information assuming the control of noise and inclusion of edges between functional structures. However, although visually these techniques can produce very striking image contrast, there is rather limited reference to the effectiveness of these techniques in achieving quantitative PVC (*191*).

In iterative image reconstructions increasing the number of iterations requires more time. Moreover, along with image resolution, noise also increases with an increasing number of iterations, which is also established in literature (*205, 206*). At high iterations, with or without filtering, noise blows up and the image will be useless. Unfortunately, the relative trade-offs for both visualization and measurement tasks are unclear and the selection of the number of iteration is a practical problem in every laboratory using PET (*203*). Since the incremental changes in spatial resolution is insignificant beyond 8 iterations, and the noise at this number of iterations does not

significantly affect the image visualization, we are likely to choose 8 iteration and 1 mm Gaussian smoothing filtering for ^{64}Cu-ATSM image reconstruction using PSF-OSEM algorithms for best effective spatial resolution.

4.1.3 PVC via post-reconstruction image processing

Alternatively, PVC can be performed by image restoration in image space. Image restoration is a wide field of study which has been applied to numerous applications. Numerous approach and variant of those approaches exists in the literature. We investigated 4 image based PVC methods. We first applied these technique to a digital simulated phantom, then to PET images of a homemade phantom mimicking human carotid plaque and to clinical human carotid plaque ^{64}Cu-ATSM PET/MR images. The PVC approaches studies included the region-based geometric transfer matrix (GTM) method, the voxel-based iterative deconvolution method (Richardson-Lucy), as well as regularized iterative deconvolution methods (RL deconvolution with total variation regularization and anatomy image (MR, CT, etc.)-guided, image restoration.

4.1.3.1 Image-based PVC methods

I. Region-based geometric transfer matrix (GTM) method

The GTM method, initially introduced by Rousset et al. (*186*), is based on the principles of linear systems and pairwise interaction between identifiable regions containing homogeneous radioactivity concentration. It is based on the fact that the PET image is the convolution of the activity distribution present in the FOV by the response function of the PET system in terms of its PSF. Then the true activity distribution is composed of the linear superposition of substructures of activity T_i with mean observed value within ROI_j:

$$t_j = \sum_{i=1}^{N} w_{ij} T_i, \quad (15)$$

where w_{ij} represents the contribution of each substructure to any ROI_j in the image and computed for each component of nonzero activity to generate the matrix of regional transfer coefficients, known as the geometric transfer matrix (GTM):

$$\begin{bmatrix} t_1 \\ t_2 \\ \vdots \\ t_N \end{bmatrix} = \begin{bmatrix} w_{11} & w_{21} & \cdots & w_{N1} \\ w_{12} & w_{22} & \cdots & \vdots \\ \vdots & & \ddots & \vdots \\ w_{1N} & w_{2N} & \cdots & w_{NN} \end{bmatrix} \times \begin{bmatrix} T_1 \\ T_2 \\ \vdots \\ T_N \end{bmatrix}, \tag{16}$$

where the diagonal terms represent tissue self-interaction (regional recovery coefficients) and off-diagonal terms express the fraction of true activity T_i spilled over from domain D_i and integrated in ROI_j.

The regional values actually observed with PET, t_j, and the GTM represent a system of linear equations that can be solved for the true values T_i.

II. Richardson-Lucy deconvolution

The Richardson-Lucy (RL) deconvolution named after William Richardson and Leon Lucy (*215, 216*), is a Bayesian-based derivation of iterative expectation-maximization (EM) algorithm (5, 13) for recovering a latent image that has been blurred by a known PSF. It's often chosen for its simplicity and performance (*191*).

The RL algorithm is based on the following mathematical image formation model:

$$i(r) = P\big(o(r) \otimes h(r)\big), \tag{17}$$

where r is a three-element vector ($[x, y, z]^T$) representing a point in a three-dimensional space or two-element vector ($[x, y]^T$) in two dimensions, $i(r)$ represent the recorded image represented as 3D array, where each item value corresponds to the intensity of a measured voxel, $o(r)$ is the object, $h(r)$ is the PSF, $\otimes$ denotes convolution operator, P represents Poisson noise originating from counting photons.

The RL algorithm seeks to determine$o(r)$, from the observation $i(r)$, knowing the PSF $h(r)$, by maximizing the likelihood distribution with respect to $o(r)$ (expectation-maximization, or by minimizing the functional$-\log p(i|o)$, which is equivalent to minimize $J_1(o)$:

$$J_1(o) = \sum_s(-i(r)\log[(o\otimes h)(r)] + (o\otimes h)(r)), \tag{18}$$

and it is equivalent to searching for a zero of the gradient of $J_1(o)$ which results in solving:

$$\left[\frac{i(r)}{(o_k * h)(r)}\right] * h(-r) = 1. \tag{19}$$

Let $o_k(r)$ be the estimate of $o(r)$ at iteration k. Then one iteration of the RL deconvolution is given by:

$$o_{k+1}(r) = \left\{\left[\frac{i(r)}{(o_k * h)(r)}\right] * h(-r)\right\} o_k(r). \tag{20}$$

III. RL deconvolution with total variation (TV) regularization

RL deconvolution tends to amplify noise, but regularization constraints based on some prior knowledge on the data can be applied to stabilize the solution. Thus TV regularization is added to the RL deconvolution to suppress unstable oscillation artifacts while preserving object edges (*217*).

This turns out to be a minimization problem of the resultant equation that expresses the model with maximum likelihood approach and TV regularization:

$$J_1(o) + J_{reg}(o) = \sum_r\big(-i(r)\log[(o * h)(r)] + (o * h)(r)\big) + \lambda_{TV}\sum_r|\nabla o(r)|, \qquad (21)$$

which is equivalent to solving the following equation:

$$1 - \frac{i}{(o\otimes h)(r)}\otimes h(-r) - \lambda_{TV} div\left(\frac{\nabla o(r)}{|\nabla o(r)|}\right) = 0, \qquad (22)$$

in which the derivative J_{reg} with respect to $o(r)$ is a nonlinear term:

$$\frac{\partial}{\partial_o} J_{reg} = -\lambda_{TV} div(\frac{\nabla o(r)}{|\nabla o(r)|}). \qquad (23)$$

Then one iteration of a multiplicative gradient type algorithm (RL-TV deconvolution) is defined by:

$$o_{k+1}(r) = \left\{\left[\frac{i(o)}{(o_k * h)(r)}\right] * h(-r)\right\}\frac{o_k(r)}{1-\lambda_{TV} div(\frac{\nabla o_k(r)}{|\nabla o_k(r)|})}, \qquad (24)$$

where λ_{TV} is the regularization parameter. When $\lambda_{TV} < 10^{-6}$, RL-TV deconvolution is dominated by the data model; when λ_{TV} approaches 1, RL-TV deconvolution is dominated by the regularization term.

IV. Anatomy image-guided image restoration

In this method proposed by Wang and Fei (*200*), PVC is considered as a least square minimization to restore the true radioactivity $o(r)$ from an observed PET $i(r)$ and a known PSF $h(r)$:

$$J^{deconvolution} = \sum_r\big(i(r) - o(r)\otimes h(r)\big)^2. \qquad (25)$$

It also leads to noise amplification and severe ring artifacts, therefore prior knowledge about $o(r)$ is required to regularize the minimization. Then $o(r)$ is restored by minimizing of the cost function consisting of the term describing the sum of squared difference (data fidelity term) and a second term expressing the edge constraint:

$$o = arg\min_{o} J(o) = arg\min_{o}[\sum_r (i(r) - o(r) \otimes h(r))^2 + \lambda \sum_r \sum_{k \in N(r)} \frac{w_{rk}}{d_{rk}} (o(r) - o(k))^2]. \tag{26}$$

The minimization is here calculated by the conjugate gradient (CG) method. The CG scheme guarantees descent. The CG minimization requires analytical derivatives of the cost function with respect to the true radioactivity in each pixel, which is given as:

$$\frac{\partial J}{\partial o(r)} = 2\left(\Big(o(r) \otimes h(r) - i(r)\Big) * h(r) + 4\lambda \sum_{k \in N(r)} \frac{w_{rk}}{d_{rk}} \big(o(r) - o(k)\big)\right), \tag{27}$$

, where $*$ denotes the correlation operator (because the PSF h is a symmetric Gaussian function, the correlation is equivalent to a convolution operation here), $\otimes$ denotes the convolution operator, λ denotes the balance parameter, w_{rk} is the weighting coefficient that determines the weight to enforce the regularization:

$$\mathrm{w_{rk}} = \exp\left(-\left(\frac{\Delta \mathrm{o_{rk}}}{\mu}\right)^2\right) + [1 - \exp(-\left(\frac{\Delta \mathrm{o_{rk}}}{\mu}\right)^2).,] \exp\left(-\left(\frac{\Delta \mathrm{o_{rk}}}{\nu}\right)^2\right) \exp\left(-\left(\frac{\Delta \mathrm{l_{rk}}}{\kappa}\right)^2\right) \approx$$

$$\begin{cases} 1 & |\Delta\, \mathrm{o_{rk}}| \ll \mu \\ 0 & |\Delta\, \mathrm{o_{rk}}| \gg \nu \\ 1 & \mu < |\Delta\, \mathrm{o_{rk}}| < \nu \text{ and } |\Delta\, \mathrm{l_{rk}}| \ll \kappa \\ 0 & \mu < |\Delta\, \mathrm{o_{rk}}| < \nu \text{ and } |\Delta\, \mathrm{l_{rk}}| \gg \kappa \end{cases} \tag{28}$$

, where $\Delta o_{rk} = o_r - o_k$ and $\Delta l_{rk} = MRI_r - MRI_k$, μ and ν are the radioactivity thresholds with $\mu < \nu$, κ is threshold to determine an edge present in MRI, by which an edge is considered to appear if the intensity difference between the neighboring voxels is greater than κ. If $|\Delta o_{rk}|$ is smaller than μ which indicates substantial smoothness between voxel r and k at PET, $w_{rk} \approx 1$, and the constraint for PET activity continuity is switched on. In contrast, when $|\Delta o_{rk}|$is greater than ν which denotes there is there is an edge between r and k, $w_{rk} \approx 0$ to switch off the intensity constraint. For neighboring voxels which have radioactivity difference between μ and ν, MRI edge information is employed to ensure that there is an edge in the corrected image by $w_{rk} \approx 0$ if MRI presents an edge with $|\Delta l_{rk}| \gg \kappa$.

The CG minimization is performed by iterate update of the conjugate direction and the solution is denoted as:

$$o^{m+1} = o^m + \propto d^m, \tag{29}$$

where m is the iteration number, d^m is the conjugate direction, and $\propto$ is a positive step size which is determined by a line search (*200*).

4.1.3.2 Evaluation of PVC methods using simulated PET images

I. Materials and methods

The 4 PVC methods were first validated using a synthetic dataset generated in MATLAB. The synthetic dataset started with a given true "radiotracer" distribution on a 64×64×64 image which consisted of three rows of spheres, each row had 3 horizontal spheres, with different sizes (3.0, 1.0, 2.0 times of PSF FWHM (4 pixels) in diameter) and "radioactivity" intensities (20, 40, 60) in a large background sphere with intensity of 5 resulting in different contrasts of the spheres with

respect to the background. This true radioactivity image was added with Gaussian white noise of different levels (1%, 5%, 8%, and 12%) relative to the background activity. Then the noisy PET images were convoluted with a 3D Gaussian function having FWHMs of 4 pixels. The convolution simulated the PSF blurring of the true radioactivity signal. The PSF and image size were given with a unit of pixel which can be easily mapped to typical MRI and PET resolutions.

The anatomical images for the GTM method and anatomy image-guided method was created as a digital mask in MATLAB in the same dimension and voxel size as the simulated PET images. The intensities of the spheres, background, and outside background were semi-arbitrary – they can be any combination of values as long as the MRI edge constraint parameter κ used in the anatomy-image guided PVC algorithm is between the intensities of the spheres and the background. We set them 20, 5 and 0, respective, and therefore chose 10 as the value of κ.

II. Results

All 4 PVC methods improved the shape and intensities of the spheres in the simulated PET images and the results are presented in (Fig. 45). The GTM method was the simplest to implement and fastest to execute. The requirement of well-segmented ROIs with homogeneous tracer intensities was also easy to achieve in this digital phantom because all prior anatomical information was known. RL deconvolution was also an easy and fast PVC method, but it tended to amplify noise and generated Gibb's ring artifacts with increasing number of iterations. These unwanted side effects were successfully removed in RL-TV method during iterative deconvolution at the expense of extra running time. The calculation time of RL-TV method for an image with matrix size of 64×64×64 is about 3 minutes, while it take less than 10 seconds to complete the calculation using the RL method on the same image. The anatomy image-guided image restoration method

iteratively de-convolved the PET images with PET and MR based edge-preserving constrains. It is the slowest and most complicated PVC method among the four, but most accurately recovered the activity in objects of all size studied.

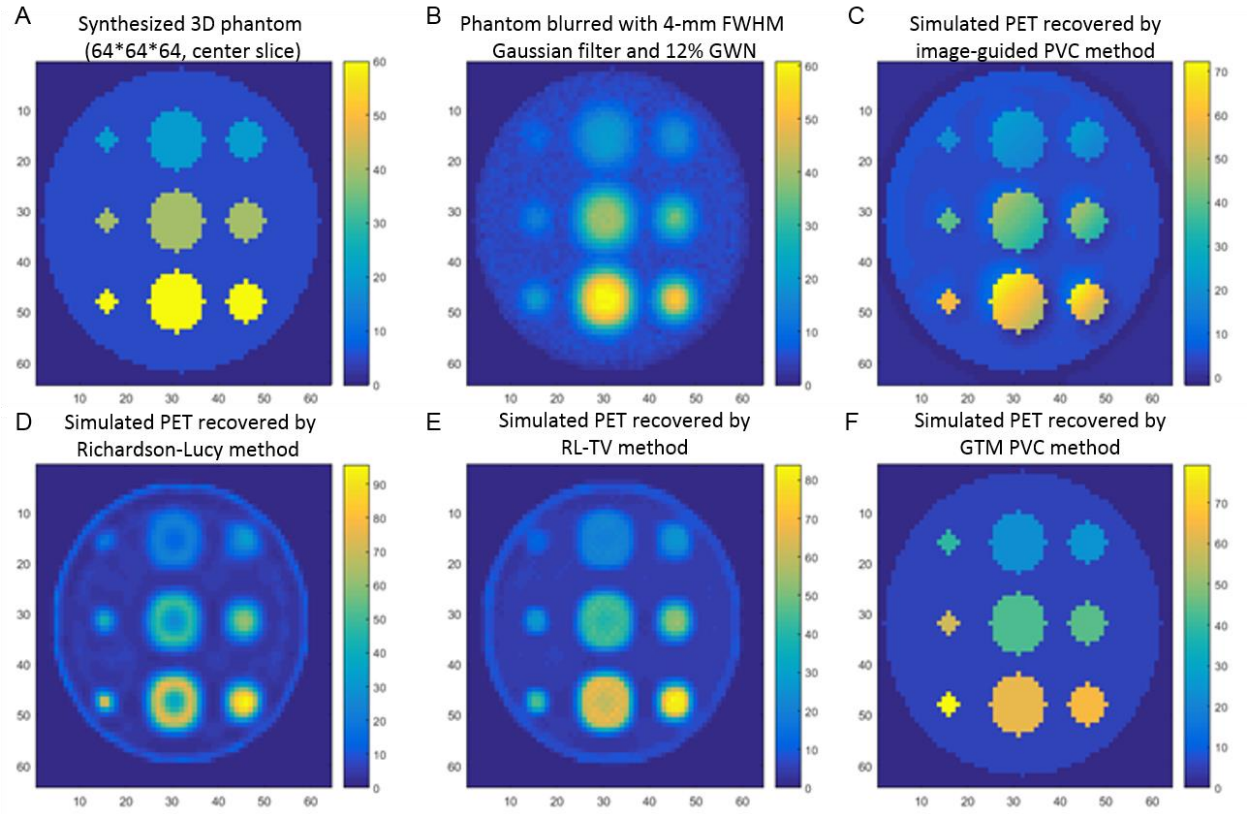

Figure 45 Partial volume correction of a simulated 64×64×64 3D image. (A) The sagittal view of center slice of the synthesized 3D digital phantom with true tracer radioactivity distribution. From left to right, the rows are objects having diameters of 1, 3, 2 times of PSF-FWHM. From top to bottom, the column are objects having tracer intensities of 20, 40 and 60. The background is a larger sphere with 60 pixels in diameter and tracer intensity is 50. (B) A representative simulated PET image created by convolving PSF with image from (A) with 12% Gaussian noise. Center slice of (B) the resultant partial volume corrected PET image using (C) anatomy image-guided method with $\lambda = 0.005$, $\mu = 0.5$, $\nu = 10$, $\kappa = 4$, (D) RL method, (E) RL-TV method with $\lambda_{TV} = 0.01$, which is chosen based on trials to achieve highest recovery coefficients but eliminate Gibbs ringing artifacts, and (F) geometric transfer matrix (GTM) method.

Table 5 compares the recovery coefficients of the spheres and the noise level in PET images using the 4 PVC methods. The recovery coefficients were less affected by the contrast and the added Gaussian noise in this digital phantom, probably because their contrasts relative to the background were all relatively high and the Gaussian noise levels were all relatively low. Generally, the larger

the size of an object, the less it would be affected by PVEs, and the PVC methods worked better to recover its tracer intensity. In this simulated phantom, the anatomy image-guided method was able to recover near 100% of the average radioactivity in each spheres. RL-TV did not result in better recovery coefficients compared the RL method and it's affected its regularization parameter which will be discussed in the next section. The recovery coefficients of the spheres were lifted with respect to increasing regularization parameter (λ) using the anatomy image-guided method, but lowered using the RL-TV method. For both anatomy image-guided and RL-TV methods, the noise in the recovered images were reduced with respect to more weighting of the regularization terms (larger λ), therefore it's important to choose an optimized regularization parameter to balance the recovery coefficients and image noise level.

Table 5 Summary of recovery coefficients of the spheres and noise levels in the unrecovered simulated PET image (12% GWN) and corrected PET images using the 4 PVC methods.

	Sphere radius	T/B contrast ratio	Uncorrected	GTM	RL	λ (RL-TV)					λ (anatomy image guided)					
						0.001	0.002	0.005	0.01	0.02	0.005	0.008	0.01	0.02	0.05	0.08
Recovery Coefficients	1-FWHM	4	0.22	2.31	0.56	0.54	0.52	0.47	0.39	0.30	0.99	0.97	0.97	0.95	0.97	0.96
		8	0.20	1.53	0.57	0.56	0.55	0.52	0.48	0.42	0.94	0.95	0.96	0.97	0.98	0.98
		12	0.21	1.35	0.61	0.60	0.59	0.56	0.51	0.45	0.96	0.96	0.96	0.97	0.99	0.98
	2-FWHM	4	0.52	1.32	0.79	0.79	0.79	0.79	0.78	0.76	1.01	1.00	1.00	1.00	1.01	1.01
		8	0.52	1.13	0.81	0.81	0.81	0.81	0.80	0.80	1.00	1.00	1.00	1.00	1.00	1.00
		12	0.52	1.09	0.81	0.80	0.80	0.80	0.80	0.79	0.89	0.92	0.91	0.94	1.00	1.00
	3-FWHM	4	0.67	1.16	0.88	0.88	0.88	0.87	0.87	0.86	1.00	1.00	1.00	1.00	1.00	1.00
		8	0.67	1.07	0.88	0.88	0.88	0.87	0.87	0.86	1.00	1.00	1.00	1.00	1.00	1.00
		12	0.67	1.04	0.88	0.88	0.88	0.88	0.87	0.87	0.94	0.94	0.95	0.99	1.00	1.00
Noise Level			0.35	0	2.87	2.41	2.12	1.55	1.08	0.82	0.17	0.12	0.11	0.06	0.02	0.02

Although the RL-TV method was faster than the anatomy image-guided method for the computation to reach a convergence, it did require a higher number of iterations which might generate more noise. Despite the difference in minimum values of the cost functions for the PET images of difference noise levels, the rates of convergence were always the same when the same PVC method and same parameters were chosen. (Fig. 46).

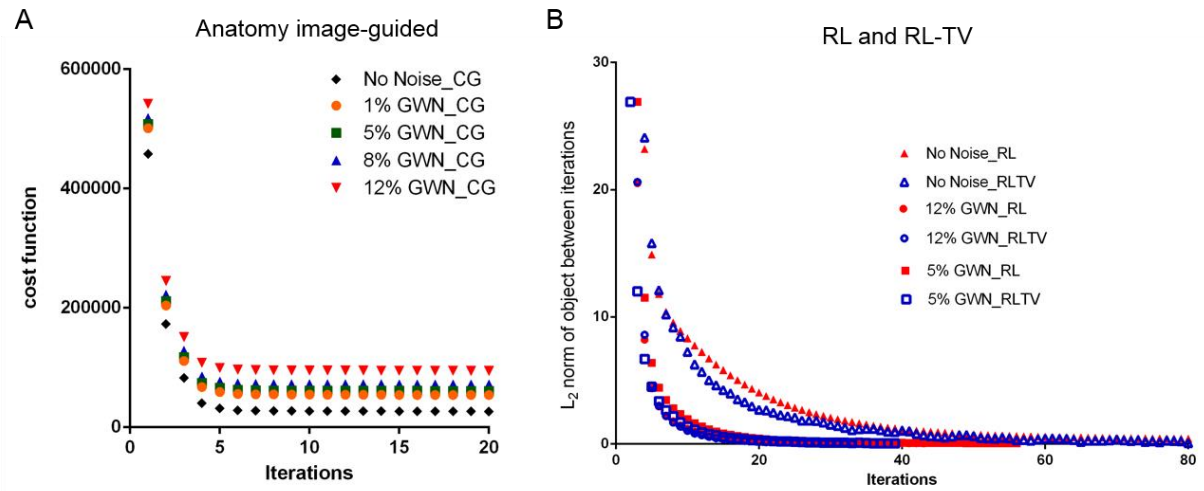

Figure 46 Comparison of rates of convergence using (A) anatomy image-guided method ($\lambda = 0.005$, $\mu = 0.5$, $\nu = 10$, $\kappa = 4$), and (B) RL and RL-TV ($\lambda_{TV} = 0.01$) method with different levels of Gaussian white noise.

4.1.3.3 Evaluation of PVC methods using an atherosclerotic plaque phantoms

I. Materials and methods

The 4 PVC methods were then evaluated on hand-made phantoms that simulated irregularly shaped plaque deposits of various thickness and activity concentrations on a blood vessel wall. For this phantom, ^{52}Mn was mixed with epoxy and a thin layer was deposited on the inner wall of 5 ml vials. The long half-life of ^{52}Mn (5.6 days) enabled long periods of study. The maximum and mean β+ energy, and maximum and mean positron range of ^{52}Mn (0.575 MeV, 0.245 MeV, 2.5 mm, and 0.63 mm, respectively) (*218*) are comparable to that of ^{64}Cu (0.653 MeV, 0.278 MeV, 2.9 mm, and 0.56 mm, respectively) (*219*), rendering its capacity to be used as a substitute to study the spatial resolution of ^{64}Cu-ATSM PET images. The property of epoxy material made it easy to create ^{52}Mn-glue deposit with comparable structure and shape to mimick human carotid plaques. The 5ml vial had a similar diameter (16 mm) to larger human arteries. Six plaque phantoms were created: three phantoms with 2.0 µCi ^{52}Mn in ~25µl epoxy, one with 9.6 µCi ^{52}Mn in ~100 µl epoxy, one with 22.0 µCi ^{52}Mn in ~200 µl epoxy, and one with 27.2 µCi ^{52}Mn in ~300 µl epoxy (Fig. 47). The true activity in the phantom was measured in a dose calibrator.

The phantom was imaged in the Siemens F220 microPET small animal PET scanner and reconstructed by the 2D-OSEM algorithm, using 16 subsets and 4 iterations with scattering and attenuation corrections, into a 128×128×159 matrix with 0.78×0.78×0.80 mm voxel size.

The small animal PET scanner had an approximately 1.8 mm spatial resolution (*220*) and therefore 1.8 mm was used as the PSF FWHM for the PVC methods. High-resolution CT imaging were acquired and used to delineate the lesions and determined their exact shape and dimensions. The reconstructed CT images had a matrix dimension of 512×512×512 and a voxel size of 0.2×0.2×0.2 mm. The reconstructed PET and CT images were registered and analyzed on Inveon Research Workplace (IRW; Siemens Medical Solutions USA, Inc., Malvern, PA).

II. The anatomy images for the GTM method and anatomy image-guided method were created as a digital mask in MATLAB based on the CT images, but interpolated and cropped to the same dimension and voxel size as the PET images. Only the "plaques" themselves that had radioactivity were included in the digital mask with an intensity of 10, and the background intensity was set to 0. These values, as the intensities of the anatomy image in the simulated digital phantom, are semi-arbitrary. They can be any combination of values as long as the MRI edge constraint parameter κ used in the anatomy-image guided PVC method is between the intensities of the "plaques" and the background. *Results*

The 2D-OSEM reconstructed PET images (Fig. 48) blurred by PVEs could be corrected by any one the 4 PVC methods (Fig. 49). It revealed similar advantages and disadvantages of using these PVC methods on real PET images compared to the simulated PET images as discussed in the previous section.

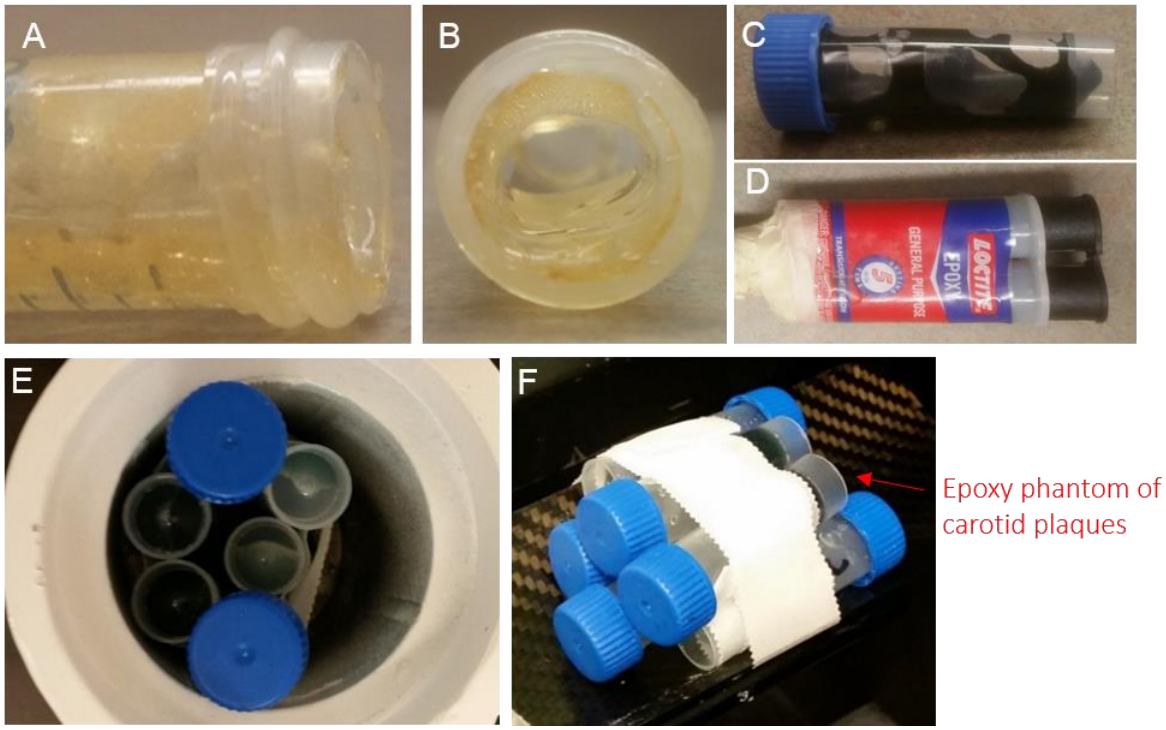

Figure 47 Set-up of plaque phantoms. (A) Sagittal and (B) transverse view of an individual plaque phantom of epoxy not mixed with ^{52}Mn. (C) Sagittal view of a plaque phantom mixed with ^{52}Mn. (D) Loctite® expoxy gel before the use. (E) 6 plaque phantoms were bundled with tape and placed in a lead shield in preparation for PET/CT scanning. (F) The bundled plaque phantoms were placed on the animal bed of the animal PET/CT scanner.

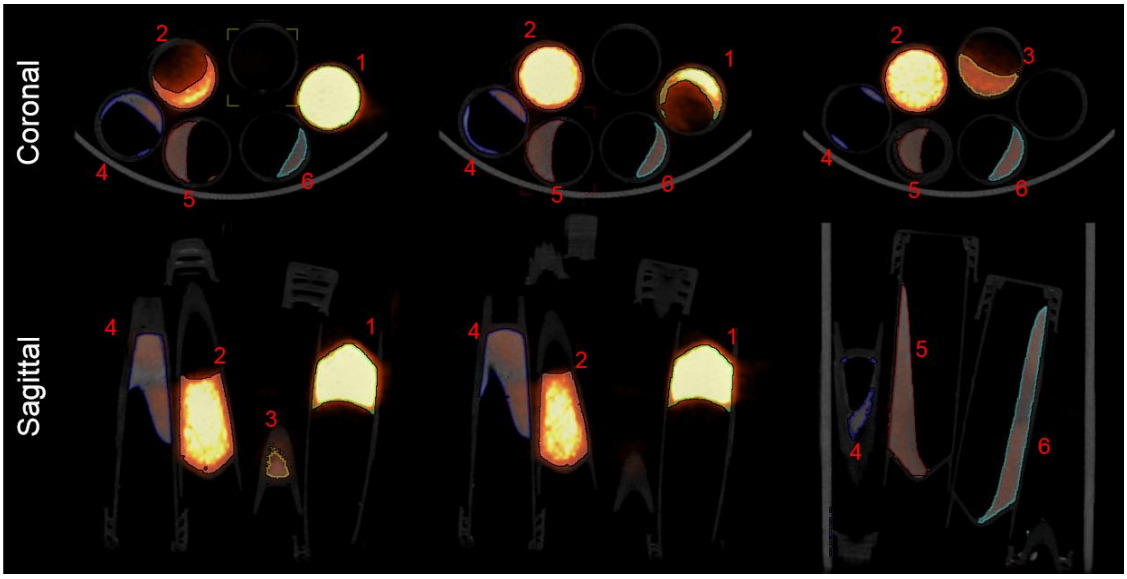

Figure 48 Coronal (top) and sagittal view of different slice of the fused PET/CT images showing the location and radioactivity intensities of 6 plaque phantoms.

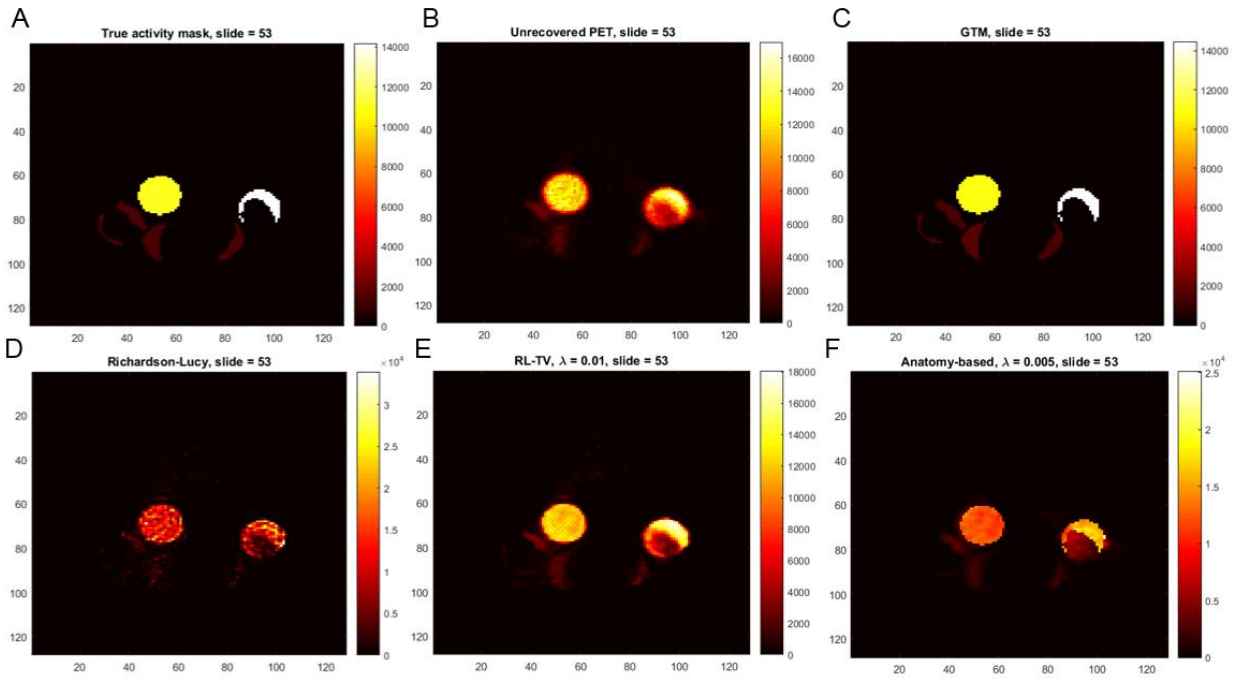

Figure 49 Application of PVC methods to the PET images of plaque phantoms. Transverse view of a selected slice of (A) simulated digital mask of true radioactivity concentration, (B) uncorrected PET image, and PET image corrected by (C) GTM method, (D) RL method, (E) RL-TV method with $\lambda_{TV} = 0.01$, and (F) anatomy image-guided method with $\lambda = 0.005$, $\mu = 10$, $\nu = 800$, $\kappa = 5$.

Table 6 summarized the total radioactivity of each carotid plaque phantom (ROI) in the uncorrected and corrected PET images, and the percentage difference from the measured radioactivity over the true activity, using the 4 PVC methods with representative regularization parameters (in applicable). The average radioactivity was calculated by multiplying the average radioactivity in the ROI measured in PET images by the total volume of the ROI measured in HD CT images after a segmentation process. PVEs resulted in an underestimation of the radioactivity of as much as greater than 20% (Table 6). All PVC methods were able to reduce the errors in radioactivity measurements to less than 10%. If was difficult to fully recover all plaque phantoms due to their different intensities and sizes, however full recovery of certain plaques for specific purpose was achievable by adjusting the parameters in the RL-TV and image-guided method. For example, as shown in Table 6, given $\lambda = 0.01$ and $\lambda = 0.005$ for the RL-TV and image-guided

methods respectively, ROI1, ROI2, ROI3, and ROI6 could achieve less 5% differences between the true and partial volume corrected activities.

Table 6 Total activity of each ROI in the uncorrected and corrected PET images, and the percentage difference from the measured activity over the true activity.

		Uncorrected PET image		GTM		RL		RL-TV (λ=0.01)		Image-guided (λ=0.005)	
ROI	True activity (μCi)	Activity (μCi)	% difference	Activity (μCi)	% difference	Activity (μCi)	% difference	Activity (μCi)	% difference	Activity (μCi)	% difference
1	27.2	24.2	11.2	27.4	0.7	28.6	5.3	28.1	3.3	27.3	0.2
2	22	19.3	12.4	22.4	1.8	22.9	4.3	22.4	1.8	21.9	0.5
3	9.6	8.4	12.7	9.7	0.9	10.0	4.0	9.8	2.2	9.5	0.9
4	2	1.6	20.2	2.2	8.0	1.9	4.6	1.9	5.9	1.9	7.4
5	2	1.6	20.6	2.1	4.2	1.9	3.8	1.9	6.0	1.8	8.6
6	2	1.6	18.6	2.2	9.5	2.0	1.5	2.0	0.7	1.9	4.6

The recovered radioactivity and recovery coefficients using the RL-TV and anatomy-image guided PVC methods were affected by the regularization parameter λ (Fig. 50, Fig. 51). Regularization parameters also changed the stop point of the converge using the RL-TV and anatomy-image guided methods, but the iteration number to achieve convergence was not affected if other parameters were kept constant (Fig. 52).

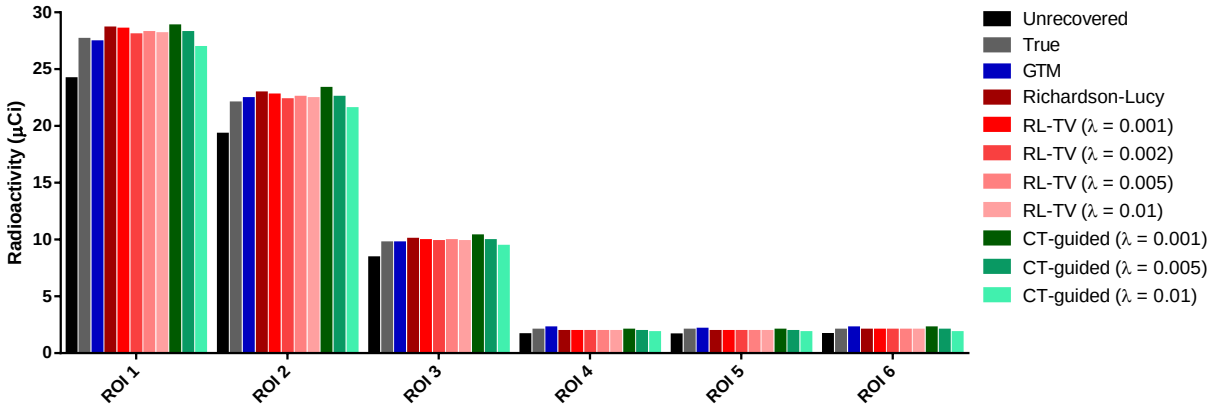

Figure 50 Comparison of true radioactivity concentrations of the 6 plaque phantoms (ROIs) to the measured mean radioactivity concentrations in the uncorrected PET image and PET image corrected by the 4 PVC methods with different regularization parameters as shown in the parenthesis of the legends. The μ, ν and κ used in the anatomy image-guided method were 10, 800, and 5, respectively.

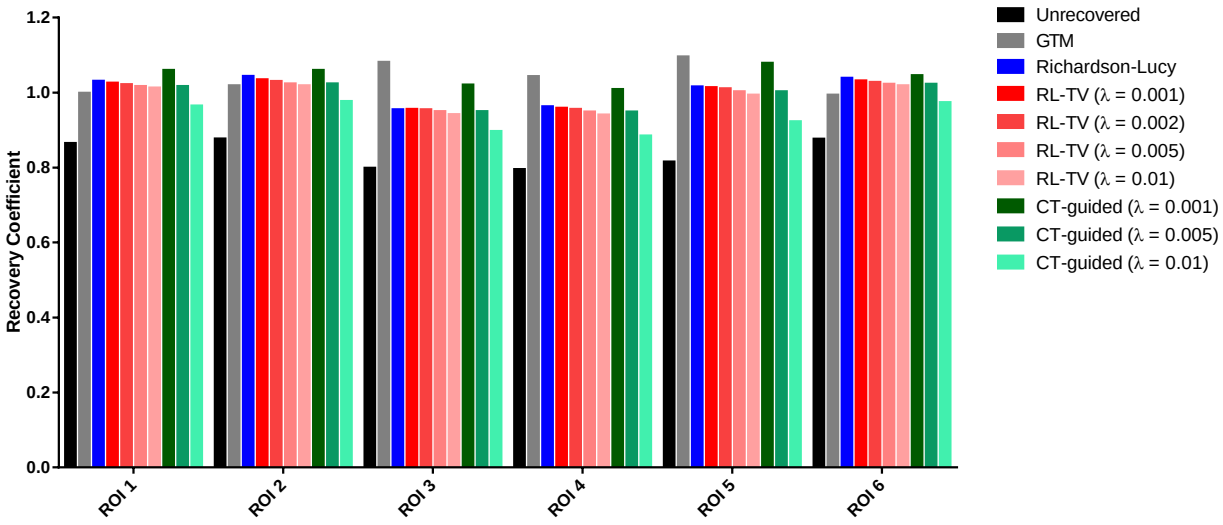

Figure 51 Comparison of recovery coefficients of the 6 plaque phantoms (ROIs) in the uncorrected PET image and PET image corrected by the 4 PVC methods with different regularization parameters as shown in the parenthesis of the legends. The μ, ν and κ used in the anatomy image-guided method were 10, 800, and 5, respectively. The recovery coefficients of the digital mask with true activity concentrations is 1.0.

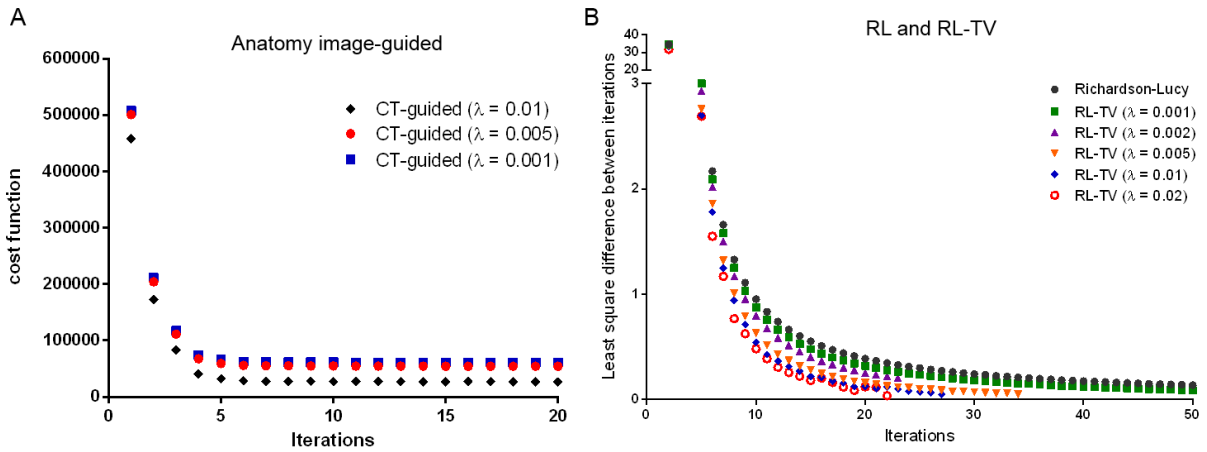

Figure 52 Comparison of rates of convergence using (A) anatomy image-guided method and (B) RL and RL-TV iterative deconvolution methods on the PET image of plaque phantoms using different regularization parameters as shown in the parenthesis of the legends. The μ, ν and κ used in the anatomy image-guided method were 10, 800, and 5, respectively.

4.1.3.4 Evaluation of PVC methods using clinical ^{64}Cu-ATSM PET/MR images of atherosclerotic plaques

I. Materials and methods

The 30-60 min carotid ^{64}Cu-ATSM PET image was reconstructed using the PSF–OSEM algorithm with 24 subsets, 8 iterations, and a 2-mm FWHM Gaussian post reconstruction smoothing filter.

A voxel size of 1.04×1.04×2.03 mm and matrix size of 344×344×127 was used. We evaluated the MR-guided, RL, and RL-TV, and GTM methods for partial volume correction. The PET images had approximately 4.2 mm effective spatial resolution based on previous measurement using the spherical phantom and using the same reconstruction parameters in PSF-OSEM algorithm (Fig. 40), therefore this 4.2 mm was used as the PSF FWHM for the PVC methods.

I. Results

All the evaluated PVC methods worked to improved signal intensity measurement of the plaque but not the background tissues (Fig. 53, Fig. 54, and Fig. 55(A)). The T_1-weighted MR image used for the anatomy image-guided method was processed beforehand by thresholding segmentation to improve contrast between the plaque and surround tissues, therefore a sharp edge was shown around the plaque in the corrected PET images. Ideally, the MR sequence would provide the appropriate contrast to allow for easy identification of the structure which would coincide to the areas of uptake by the PET tracer, then this algorithm will use an edge seen in MR and enhance an edge seen in PET. However, in reality the MR image of carotid plaques is not able to provide good enough contrast without pre-processing.

Similarly, because accurate segmentation of plaques into ROIs with homogenous radioactivity is difficult, GTM method can only provide a regional radioactivity in the ROI, but not corrected PET image on the voxel level (Fig. 54).

Due to PVC, the plaque-to-background signal intensity ratio which corresponded their radioactivity concentration ratio improved from 2 in the uncorrected PET image to 2.5-3.5 in the corrected PET images. The gain in RC varied depended on the different combinations of deconvolution parameters (Fig. 55(B)). Anatomy image (MRI)-guided method generally

generated higher ratios; RL-TV method does not improve the ratio compared to RL method, although it might work to remove the noise generated in RL deconvolution.

The results suggested that these PVC methods could potentially assist physicians to diagnose plaques using ^{64}Cu-ATSM PET/MR imaging. In ^{64}Cu-ATSM PET images, we measure the average activity concentration in the plaque and used the plaque-to-background SUV ratios to differentiate subjects with and without hypoxic vulnerable plaques. The improved plaque-to-background contrast ratios in the partial volume corrected PET images therefore will make the plaques easier and more precise to be identified. One the other hand, PVC restores the PET images that may improve the accuracy of quantitative estimation of the true activity of the plaques. Assuming that the uptake of ^{64}Cu-ATSM is associated with plaque hypoxic level, and thereby the vulnerability of the plaque, knowing the true activity will be valuable to determine the likelihood that the patient's plaque will rupture. However, further validation with more data and IHC staining are necessary to get these PVC methods clinically applicable. With the correlation of ^{64}Cu-ATSM spatial distribution as well as activity concentrations in partial volume effect corrected PET images to IHC staining of PIMO, HIF and macrophages, we will be able to demonstrate the hypothesis that PVC improves the qualitative estimation and quantitative measurement of hypoxic plaques using ^{64}Cu-ATSM PET images. Unfortunately, for reasons out of our control, we did not get IHC data to compare with yet, but the work will continue.

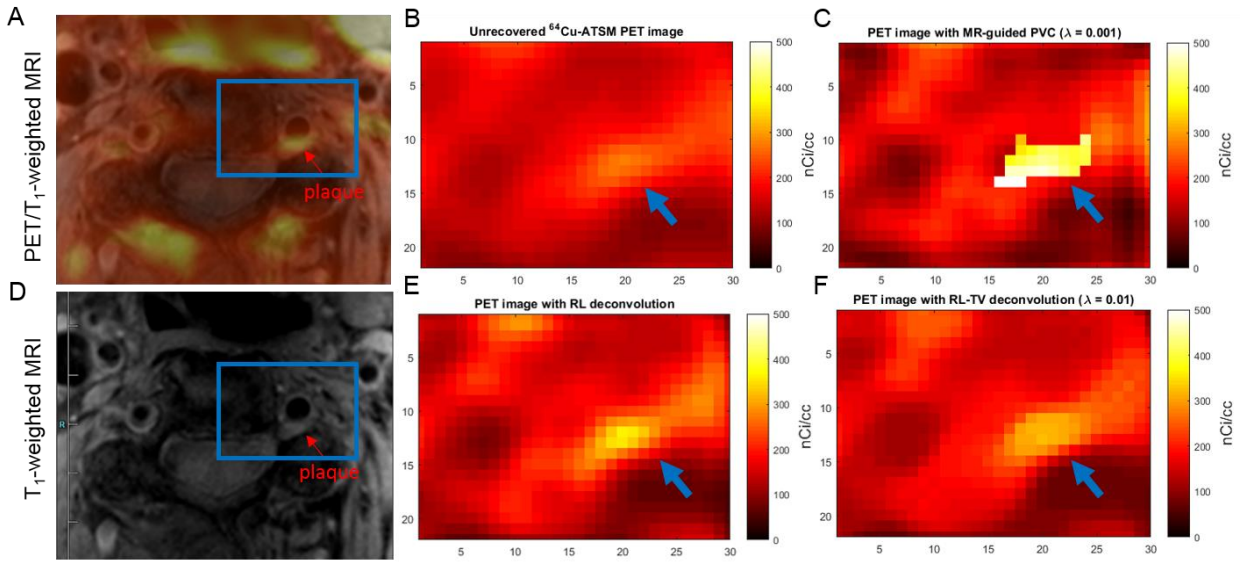

Figure 53 Application of PVC methods in clinical ^{64}Cu-ATSM PET/MR images of atherosclerotic plaques on the vertebral artery (patient #5). Transverse view of (A) ^{64}Cu-ATSM PET image fused with T_1-weighted MR image and (D) T_1-weighted MR image. (B) Region of interest indicating the vertebral plaque and surrounding tissue in blue box. Representative PVC corrected images using (C) anatomy image (MRI)-guided method with $\lambda = 0.001$, $\mu = 0.5$, $\nu = 200$, $\kappa = 100$, (E) RL method, and (F) RL-TV method with $\lambda_{TV} = 0.01$.

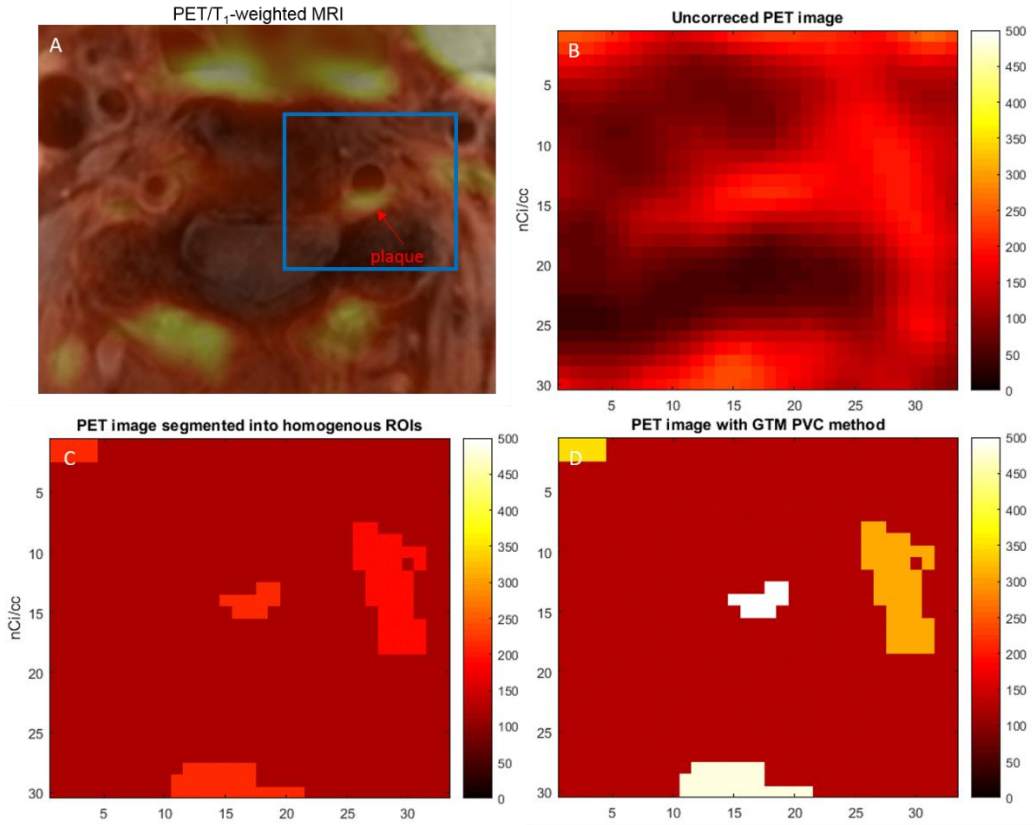

Figure 54 Application of GTM PVC method in clinical ^{64}Cu-ATSM PET/MR images of atherosclerotic plaques on the vertebral artery (patient #5). Transverse view of (A) ^{64}Cu-ATSM PET image fused with T_1-weighted MR image was zoomed in with the region of interests on the vertebral plaque and surrounding tissue in blue box. (B-D) shows the uncorrected PET image, PET imaged segmented into homogeneous ROIs and PET image after GTM partial volume correction.

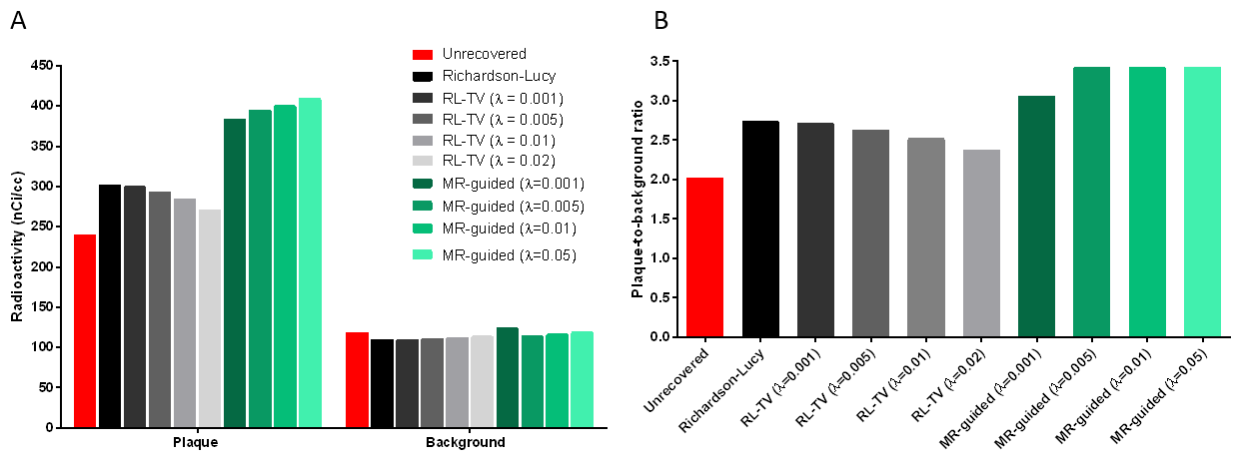

Figure 55 Comparison of the PVC results of ^{64}Cu-ATSM PET images of atherosclerotic plaques. (A) Mean radioactivity concentrations measured in the plaques and background of the uncorrected PET image, and image corrected by RL, RL-TV, and MR-guided PVC methods with various parameters as shown in the parenthesis of the legends. The μ, ν and κ used in the MR-guided method were 0.5, 200 and 100, respectively. (B) The corresponding plaque-to-background intensity (radioactivity concentration) ratio of the uncorrected PET image and the corrected PET images.

4.1.3.4 PVC via post-reconstruction image processing: discussion

We compared the effectiveness of various PVC methods with simulated data and homemade carotid phantoms and demonstrated that PVC was an effective image processing approach to improve the PET image quality in terms of its contrast, and may be a promising approach to improve the qualitative detection and/or quantitative measurement of hypoxic plaques at different levels of accuracy in carotid ^{64}Cu-ATSM PET/MR imaging, though further studies to correlate the partial volume recovered radiotracer activity and PET image to immunohistochemistry staining are necessary to validate the efficiency the PVC methods.

The ultimate goal of PVC is to reverse the effect of the system PSF in PET images and thereby qualitatively and quantitatively restore the true activity distribution. This can be achieved region- or ROI-based post-reconstruction approach that attempts to recover true radioactivity in the region level with the assumption of homogeneous radioactivity distribution with each ROI. Usually these ROIs are obtained by segmenting or classifying the co-registered anatomical images into a number of non-overlapping compartments (*221*). GTM method is a typical ROI-based method where a

regional point spread function is computed for each ROI by PSF convolution of the region assuming unit radioactivity (*186*), and then linear equations are formed to solve the regional corrections. The GTM approach not only requires registration and segmentation of anatomical images but also need the knowledge about regional structural and functional correspondence to satisfy the assumption of regionally homogeneous radioactivity. This is apparent in the initial proposed application of this approach – brain, which can be easily segmented into large ROIs of gray matter, white matter, and cerebrospinal fluid (CSF) in MR images (*186*). However, the segmentation of carotid plaque, on the scale of millimeter level, is more difficult. The homogeneous radioactivity assumption implies that the correction is performed between voxels in different segmented regions, but not between voxels in the same region (*191*). Considering the complex composition of atherosclerotic plaques, PVC should thus be considered, not as an exact correction, but as a first order approximation.

PVC can be also done by voxel-based deconvolution, either in the image domain post reconstruction or during iterative image reconstruction by incorporating the PSF in the system matrix such as the PSF-OSEM algorithm. The deconvolution during image reconstruction has a superior noise performance because a larger number of measured data values are involved in the reconstruction of each voxel value, resulting in noise averaging (*191*). However, similarly to the post-reconstruction deconvolution, the resulting images often suffer from so called 'Gibbs ringing artifacts', corresponding to ringing in the vicinity of sharp boundaries, which is related to missing high frequency information in the measurement. This could be caused by insufficient sampling in the image domain by the use of too large voxels. The RL iterative algorithm is post-reconstruction deconvolution PVC method derived for Poisson noise (*215, 216*) and commonly used in astronomy and microscopy image enhancement (*217, 222*). RL assumes that the Poisson noise model is

adequate for PET. The number of detected photons is a Poisson process whose variance is equal of the mean of the number of counted photons. The main advantage of the RL deconvolution PVC method is that it depends on PET image data only, and no anatomical data is needed. However the inclusion of anatomical information allows to increase PET signal contrast and improves quantitation accuracy at the lesion boundaries if properly identified. The main undesired property of the RL algorithm is that, in the presence of noise, deconvolution process converges to a solution which is dominated by noise (*223*). Because of the ill-conditioned nature of the deconvolution-based restoration problem, some sort of regularization must be used to avoid high-frequency noise-amplification and introduction of artifacts. This can be achieved in a variety of ways such as early iteration termination, post-reconstruction filter or by incorporating a regularization term or anatomical information and tissue homogeneity constraints into the deconvolution iteration. The total variation (TV) regularization is often applied in the RL algorithm (*217, 222*) to increase the sharpness of object borders and obtain smooth homogeneous areas (*223*). It assumes uniform uptake within regions. This algorithm and many similar approached introduce a balancing parameter that allows to weigh in the importance of the penalty term with respect to the data fidelity term. In RL-TV, this parameter is λ_{TV}. We determined the regularization parameters by optimization of the recovery coefficients. Some studies estimate the TV regularization parameter from the images as the algorithm process (*222*). The anatomical image-guided PVC methods, in contrast utilizes structural information from other imaging modalities as a priori information (in the form of a penalty terms) in order to favor solutions where lesion edges in the anatomical images are used to emphasize contrast in the PET images. We make the assumption that the identified structure in the anatomical image is the region of increase uptake in PET, which is not necessarily true for other cases. Regularization term (the weighting coefficient) in this method contains 4

unknown parameters that must be carefully chosen to achieve optimal deconvolution results that would be as close as possible to the 'true' image.

To accurately measure uptake in small structures is challenging, and PVC is even more challenging in preclinical imaging of rodents where structures are extremely small relative to the achievable resolution even on preclinical small-animal scanner (~1.8 mm for Siemens *micro*PET/CT scanner). In addition, for PVC in small animal preclinical imaging it may be important to take into account the spatial variation of the PSF as well as the positron range in the case of PET (*191*). However, since our dedicated animal (mouse and rabbit) models were developed for demonstrating the ability of ^{64}Cu-ATSM to image hypoxic plaques, there was no quantitative end point where the absolute level of tracer uptake was required.

It should also be pointed out that image noise and noise correlations, as well as the precision of quantitative estimates of activity, are measures that can often be equally important as image fidelity or quantitative accuracy (*191*), and therefore it is crucial to evaluate on the noise handling of the PVC methods in further studies. Also the sensitivity of PVC techniques to error in pre-correction processing steps, such as registration and segmentation in anatomically guided methods should be evaluated.

To conclude this section, PVC is an important aspect of quantitative analysis in PET and remains an area of active research. A large number of different methods for PVC have been proposed in the past – some methods utilize anatomical information while some do not. Some methods produce only mean values for one or more regions, while some perform a voxel-by-voxel correction for a region or the whole image. Some methods are applied to a reconstructed image, while some are incorporated in the reconstruction algorithm. Although these PVC methods were originally

developed for cardiology, neurology or oncology with either PET or SPECT, most methods may be applicable in multiple areas. However, although their application is theoretically straightforward for the most part, it is difficult in practice. A given, very specific problem may require extensive validation and this was the purpose of our study. The validation also need to be done against a gold standard. In this case, it would have been IHC staining which would have provided the absolute hypoxic level value. Unfortunately, we don't have IHC data yet.

Conventionally, it is believed that there is no need for clinical evaluation of PVC methods and PVCs are believed to increase variance. Nevertheless, as the systems of multimodality systems, which combine PET (or SPECT) with CT or MRI to allow acquisition of co-registered functional and anatomical images, are becoming widely available, we can expect that the time has come for PVC to be routinely used in clinical practice including but not limited to carotid plaque ^{64}Cu-ATSM PET/MR imaging.

4.2 Correction for attenuation effects due to the carotid surface coil and the thermoplastic holder

PET is a fully quantitative technology and well known to be affection from attenuation of the annihilation photons in the body by photo-electric effect and by Compton scatter, one reason being that true coincidence events are absorbed in the body. Attenuation correction (AC) for photon attenuation is thus an essential step when reconstructing high-quality, quantitatively accurate PET images. In PET-CT, attenuation correction is performed routinely based on the available CT transmission data (*224*). In PET-MR, most MR-AC strategies require the use of complementary MR or morphology templates generated from MR images. MR-AC consists of MR image acquisition, segmentation, truncation compensation, μ-value assignment, and correction for patient table and RF coils. (*225*)

Yet one challenge to the MR-AC approach is the absence of the flexible body or surface coils in the MR attenuation correction. Although built using low density material and judicious placement of the electronic components, these coil will show some attenuation to annihilation photons. Radio-frequency (RF) receiver coils are commonly placed as close to the subject as possible to maximize SNR in MR data acquisition. It has been recognized that these coils will attenuate (and scatter) annihilation photon emission data if they are present inside and during the PET scan. These coils do not appear in the MR image (*226*). As such, an AC map (μ-map) derived purely from an MRI will not be complete because it lacks the coil structure that also causes attenuation. Static coils (head/neck, spine) and patient bed can be integrated into the μ-map via templates (*227*, *228*). However, the carotid surface coils as well as the thermoplastic holder that was used to fixed the patient's neck to minimize motion artifacts used in our study contain elastic components and hence cannot be located easily with respect to the gradient coil or the patient.

This situation is much more difficult to treat with a template AC method because the active components of the coil can be in different position relative to each other, meaning a previously acquired scan may not match the distribution of attenuating material in a patient scan. Despite the optimization of surface coils for PET (design, low-attenuating materials), it may still introduce errors in MR-AC (*224*, *225*, *229*, *230*). Neglecting the attenuation effects caused by MR body surface coils in combined PET/MR imaging leads to as much as 20% underestimation bias in measured activity concentration (*231*).

Currently, in our Siemens mMR whole-body PET/MR system, a MR attenuation μ-map is derived from a 2-point Dixon VIBE (volumetric interpolated breath-hold examination) sequence that generates a water only, fat only, in-phase, and opposed phase imaging series (*232*). Dixon-based MR-AC is a tissue segmentation approach that permits segmentation of fat, soft tissue, lung and

air (*233*). The attenuation effects resulting from the carotid surface coil will be taken in consideration in the Dixon-based MR attenuation μ-map.

Some methods of estimating the amount of attenuation caused by MRI surface coils in the PET field of view during combined PET/MRI scanning have been reported to achieve accurate quantitative recovery in the PET images (*231, 234, 235*). We applied a method that was modified from a recently published template approach developed by our colleagues in Washington University (*227, 228, 236*), in which the coils and holder were imaged beforehand in a CT scanner, then converted into appropriate attenuation correction μ-maps for PET data, and inserted into the AC map for the object being imaged.

4.2.1 Correction for attenuation effects: material and methods

I. Validation with Phantom: Set-up

The phantom was created using a 2-liter (~10 cm in diameter) cylindrical plastic bottle that was completed filled with distilled water. The bottle was wrapped with the 2 pieces of carotid surface coils on sides and secured on a block of Styrofoam with the thermoplastic holder and paper tape. The 3T carotid surface coil used at our institution is a dedicated two sided, four-channel phased array surface coil (Machnet, Netherlands) to improve the signal-to-noise ratio in carotid arteries. The effective length of the coil in the anterior posterior direction is 105 mm, and the width is 60 mm. The carotid coils were rigidly attached to the thermoplastic holder. 4 Vitamin E capsules were place on each piece carotid coil, secured with paper tape, as the fiducial markers for visualization in PET/MR imaging (Fig. 56).

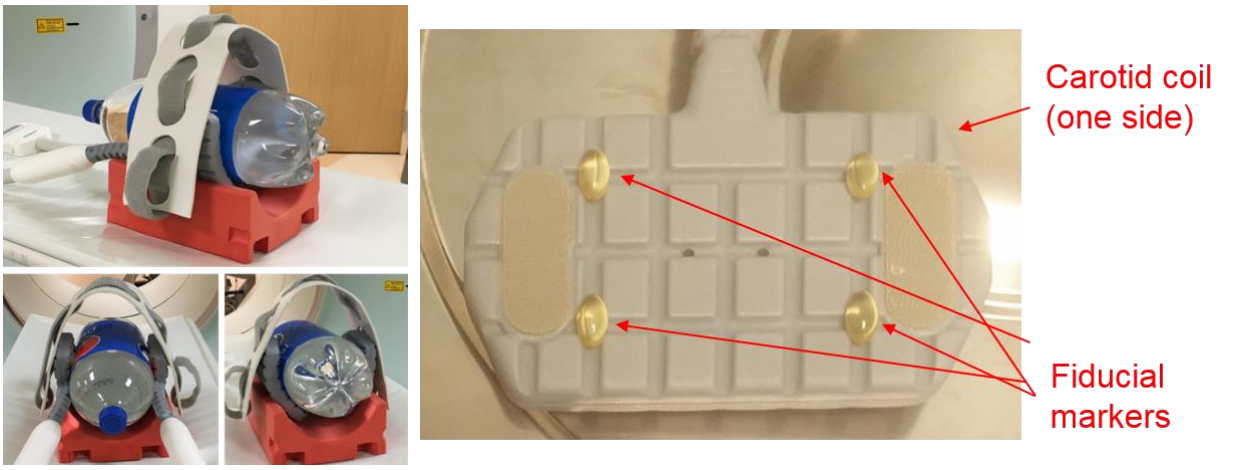

Figure 56 Pictures showing the set-up of radioactive phantom and the places to place the fiducial markers on the carotid coils.

II. High-Resolution CT

A CT scout scan was acquired on a Biograph 40 TruePoint PET/CT (Siemens Healthcare) followed by a high-resolution, low-amperage CT scan with the following parameters: 120-kV collimation, 1.5-mm slice thickness (40×0.6 mm), 35 mAs, and 300-cm FOV. Images were reconstructed with 1.5-mm slice thickness and 0.48-mm pixel size on a 512×512 matrix. This scan provided the template images that were registered to the anatomic MR attenuation map.

III. Transmission scan

A 45-min transmission scan of the phantom was obtained on a Focus 220 small-animal PET scanner (Siemens Medical Solutions) using a rotating ^{57}Co point source. The ^{57}Co transmission image (attenuation map) was reconstructed using the *maximum a posteriori* (*MAP*) *reconstruction algorithm and analyzed with ASIPro (Siemens Medical Solutions) to measure the attenuation coefficient of the coil. The known attenuation coefficient of water for 511 keV photon provided the reference.*

IV. Image Processing

The CT images of the phantom were processed in MATLAB to create a digital mask that extracted the pixels elements only belonging to the carotid coils and thermoplastic holder. The measured CT Hounsfield unites of the carotid coils and thermoplastic holder were then scaled to the attenuation coefficients, by the equation:

$$HU = 1000 \times \frac{\mu - \mu_{water}}{\mu_{water} - \mu_{air}}, \quad (30)$$

where μ is the average linear attenuation coefficient in a voxel of carotid coils or thermoplastic holder, μ_{water} and μ_{air} are respectively the attenuation coefficient of water and air. The digital mask was split into its left and right halves. The fiducial markers were identified in the CT images and co-localized the water-only images acquired in the MR-AC acquisition. Rigid point based registration was performed to align the fiducial markers in the images of the RF-coil/holder CT images to the fiducial markers on the MR images for each half of RF-coil/holder arrangement. The algorithm proceeded by the least square minimization of the three dimensional distances in CT and MR images through successive operation of rotations and translations. Minimization was performed using Powell minimization algorithm in IDL. Each half of the CT template was then overlaid on the measured MR-AC u-maps of the phantom. Clinical human carotid plaque ^{64}Cu-ATSM PET/MR images then were used to evaluate the carotid coil attenuation correction method. The fiducial makers (Vitamin E pills) were used to locate the carotid coils (and thermoplastic holder). The spatial location of the fiducial markers, with respect to the MR scanner coordinates, were clearly visualized with the 2-point Dixon MR imaging sequence and extracted from the water-only MR images using this sequence. A 3D rigid transformation of CT template of the carotid coil was then performed to minimize the sum of the square difference of the spatial location of the fiducial markers as seen on the CT template and in-phase MR images. The algorithm was

coded in IDL, version 8.1 (Interactive Data Language, Exelis Inc.), and used the Powell minimization algorithm (*236*).

In order to validate the accuracy of the correction, we used the same bottle phantom filled with 37 MBq (1 mCi) ^{18}F-FDG and water, compared the measurements of *decay-corrected* radioactivity concentration in PET/MR images with carotid coils on and off.

4.2.2 Correction for attenuation effects: results

A digital mask of CT template in Hounsfield unites (HU) of the carotid coils and thermoplastic holder was created from the CT template. The water ROI on the Focus 220 ^{57}Co transmission image revealed a measured attenuation coefficient of 0.092 cm^{-1} which was consistent to the nominal value (0.092 cm^{-1}), indicating an accurate calibration of the Focus 220 for attenuation correction measurement. The measured CT Hounsfield unites of the carotid coils and thermoplastic holder (approximately on the range 500-3000) scaled to the attenuation coefficients were mostly on the range 0.1-0.3 cm^{-1}. The digital mask was interpolated to have a matrix size of 344×344×127 with a voxel size of 2.08626×2.08626×2.03125 mm^3 in order to in order to match the dimension of the MR attenuation map (Fig. 57).

The overall improvement in radioactivity concentration of ^{64}Cu-ATSM PET images with carotid coil attenuation correction was on average 7.6% (Fig. 58). The coil attenuation effects were not equally distributed in PET images; higher effects were found around the neck of the patient where the coils were placed (Fig. 59).

The results of the bottle phantom with and without coil in ^{18}F-FDG PET/MR imaging showed that the average attenuation effects due to carotid coils was 6.2% (Fig. 60). This number was a little

smaller but reasonable compared to the improvements with attenuation effects correction in our study, considering that we also took the effects from thermoplastic holder into account.

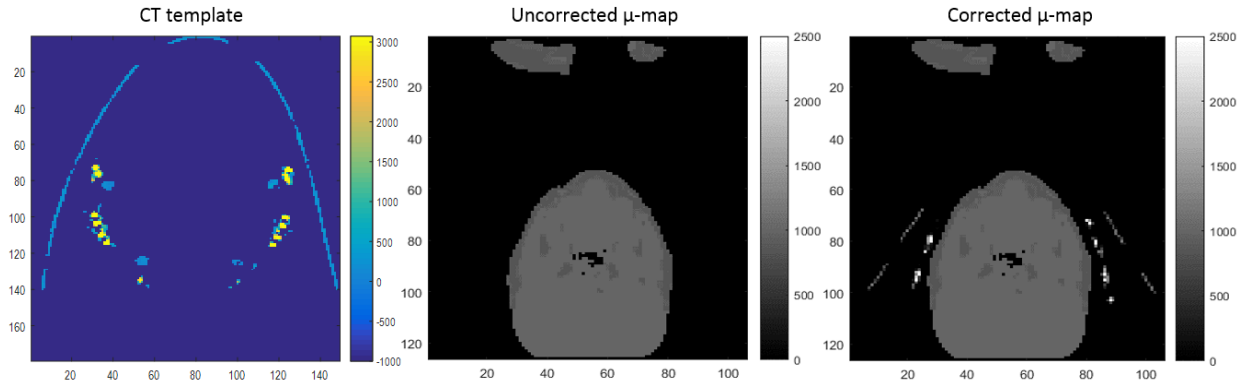

Figure 57 From left to right, the coronal view of the CT template of carotid coils and thermoplastic holder in CT Hounsfield unites, the uncorrected MR attenuation μ-map acquired by the 2-point Dixon MR imaging sequence, and the μ-map that incorporated the carotid coils and thermoplastic holder.

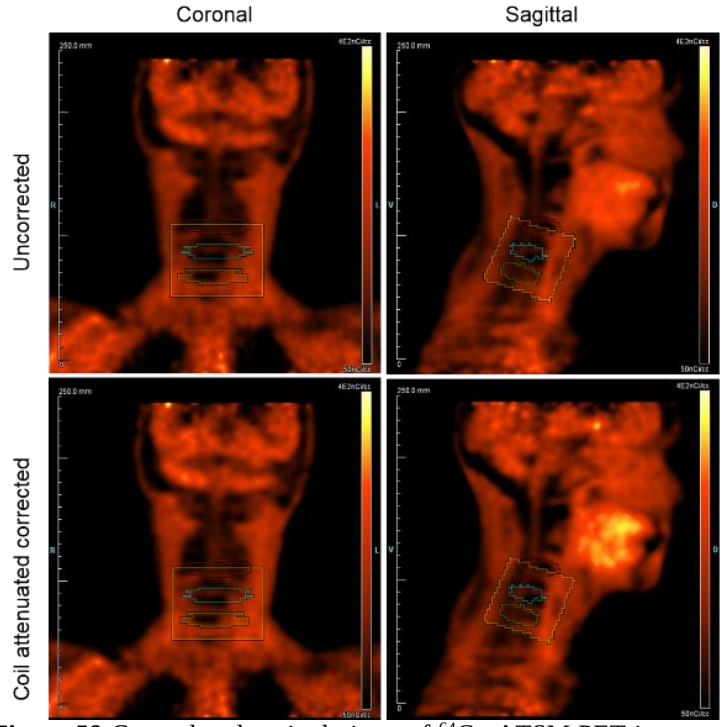

	Without coil correction (nCi/cc)	With coil correction (nCi/cc)	Increase (%)
Total	153.7	165.4	7.6
Top	100.8	110.7	9.8
Middle	104.0	111.7	7.4
Bottom	138.9	147.6	6.3

Figure 58 Coronal and sagittal views of ^{64}Cu-ATSM PET images without and with carotid coil attenuation effects correction. The activity concentration (nCi/cc) was measured on the top, middle, bottom and overall regions of the patient's neck, and the relative improvements with carotid coil attenuation effects correction were calculated respectively (right panel).

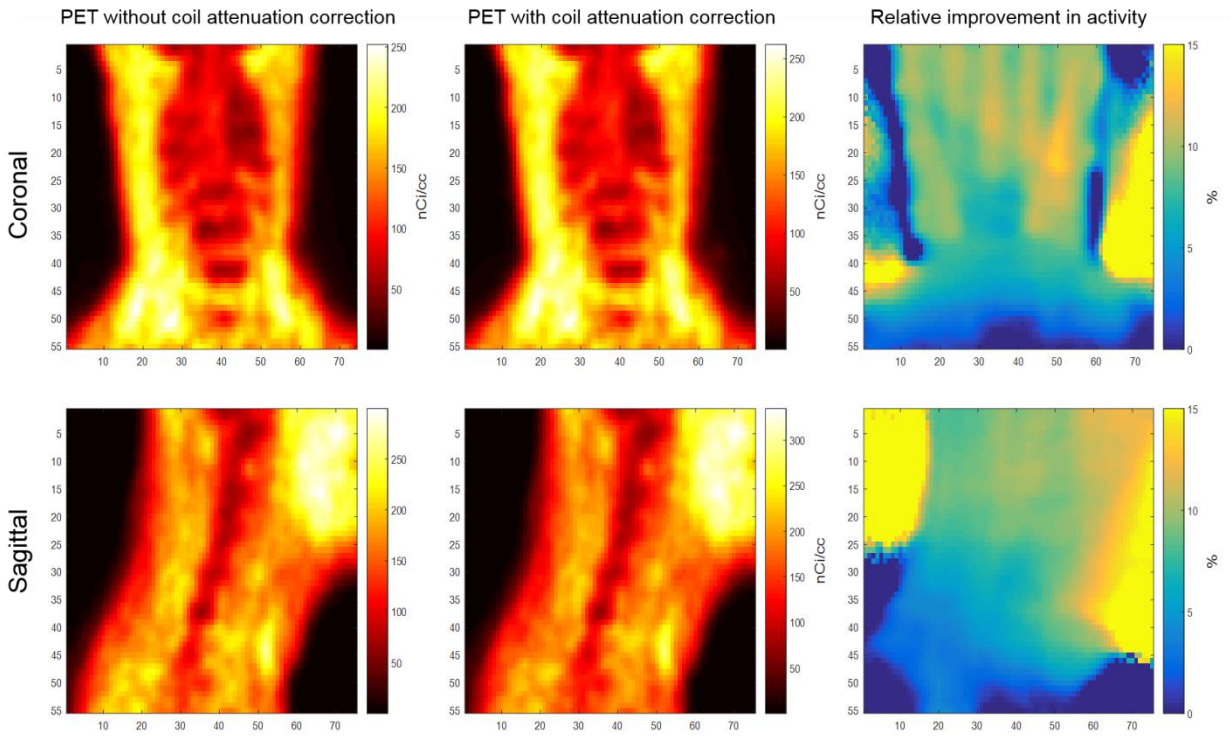

Figure 59 From left to right, coronal and sagittal views of ^{64}Cu-ATSM PET images focused on the neck area of the patient without and with carotid coil attenuation effects correction and the relative improvement in activity concentration on each pixel after correction.

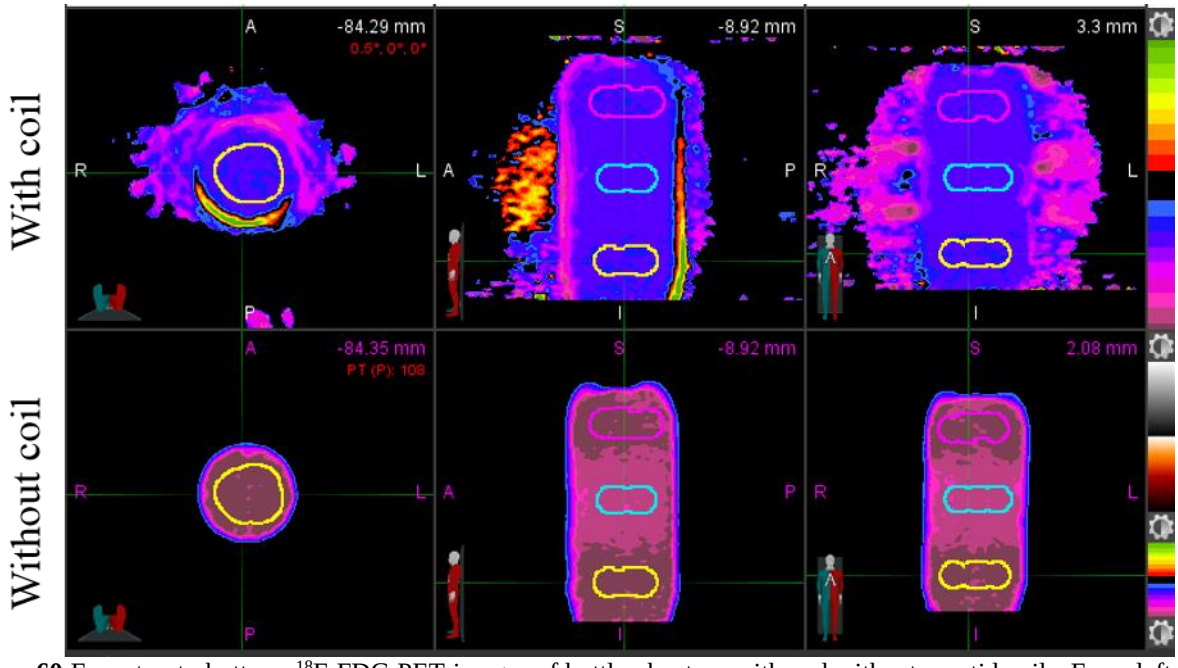

Figure 60 From top to bottom, ^{18}F-FDG PET images of bottle phantom with and without carotid coils. From left to right, transverse, sagittal and coronal views of the PET images. The attenuation effect from the carotid coils is overall 6.2% and equally distributed in the phantom.

4.2.3 Correction for attenuation effects: discussion

We used a template approach to incorporate the attenuation effects of the carotid surface coils and neck thermoplastic holder into the MR attenuation μ-map for carotid artery ^{64}Cu-ATSM PET image reconstruction.

Due to the inhomogeneous improve in radioactivity concentration in the PET images, the attenuation correction method can be potentially used in human carotid plaque ^{64}Cu-ATSM PET/MR images to improve the accuracy of measured target-to-background ratios.

In addition to the template approach, ultrashort echo time (UTE) MR sequences, as well as the combine UTE-Dixon sequence, shows promise to correct for attenuation effects from carotid coils. The UTE uses a greatly reduced echo time to capture rapidly decaying signals have demonstrated the ability to detect a signal from even cortical bone (*237*). Hofmann *et al* claimed that MR sequences with UTE could possibly help detect surface coil landmarks and thus account for their attenuation (*224*). Eldib et al used a combination of and non-rigid registration of a CT-based attenuation map and the UTE image of carotid coils for markless attenuation correction (*238*). However, UTE-based sequences are not yet FDA approved for clinical use (*236*)

Chapter 5: Commercialization of ^{64}Cu-ATSM

At the end my doctoral training, I completed a 3-month internship/co-op as a data analyst in a healthcare consulting company named Velocity Biogroup, Inc. in Philadelphia, PA.

During this co-op, I started with learning the United States laws and policies regarding patent and intellectual property, FDA approval regularizations, the respective coverage of Medicaid and Medicare programs, and so on. Since it was a biomedical product oriented company, I was significantly involved in reviewing and evaluating the new medical devices and brand name drugs or FDA 505(b)(2) approved generic drugs for the company's clients from the US and other countries (e.g. France, Korea, India) who are seeking for their markets in the US. I also helped to develop a recipe to extract useful information from a big healthcare database using MySQL and IBM Watson Analytics service, and visualize the results with the company-owned software.

In the meanwhile, I put some of my focus to think of how to move the imaging agent ^{64}Cu-ATSM from the preclinical studies into patients in light of what I've learned during the co-op in terms of translation and innovation. ^{64}Cu-ATSM is currently an FDA approved investigational new drug (IND), but it was first synthesized 20 years and a lot of groups worldwide are able to make ^{64}Cu-ATSM compounds. Despite that we disclosed the potential usage of ^{64}Cu-ATSM in imaging hypoxic carotid atherosclerosis in PET, it is not patent protected. In order to get ^{64}Cu-ATSM FDA approved for this specific aim, a large-scale Phase II and/or Phase III clinical trial is necessary. This, however, takes a lot of time, money and efforts. It might be doubtfully to devote such great resources to perform the clinical trial for very limited commercial opportunities, even though there

is no obstacle to recruit patients in the strict condition of vulnerable carotid plaques who may have to undertake carotid endarterectomy.

However, given that this agent is disclosed, there are still some commercial opportunities open to us as a university which can manufacture it, because we are one of the only 3-4 facilities in the United States who makes ^{64}Cu weekly by an on-site cryotron. We have rich connections and plenty of experience to supply ^{64}Cu to other facilities, and therefore we can be the most convenient supplier of ^{64}Cu-ATSM to those facilities who can't either make ^{64}Cu or ATSM themselves. Without a large-scale clinical trial, ^{64}Cu-ATSM alone may not be used as the direct predictor of carotid vulnerable plaques, but as a supportive evidence of it. The ^{64}Cu-ATSM uptake in the PET and plaque MR image of the patient will then be recorded and saved in the patient's database, together with other information of the patient, such as his/her age, gender, weight, ethnicity, disease history, using an statistically analytic method, such as the IBM Watson Analytics, may improve the success to predict the probability the patient of developing advanced vulnerable plaques.

The other commercial opportunities exist in using ^{64}Cu-ATSM to target other hypoxic cells with a patent before the disclosure, which is left for future studies.

Chapter 6: Conclusions

In this dissertation research, we showed the feasibility of ^{64}Cu-ATSM to identify hypoxic atherosclerotic plaque in a genetically-altered mouse model. We fully validated the feasibility of using ^{64}Cu-ATSM to image the extent of hypoxia in a rabbit model of atherosclerotic-like plaques using a simultaneous PET/MR system. Then we proceeded with a pilot clinical trial to determine whether ^{64}Cu-ATSM MR/PET scanning is capable of detecting hypoxic carotid atherosclerosis in human subjects.

We investigated 4 partial volume correction methods to correct for partial volume effects and incorporated the attenuation effect of the carotid surface coil to MR attenuation correction μ-map to correct for photon attention.

In the long term, this imaging strategy will help identify patients at risk for cardiovascular events, guide therapy, and study plaque biology in human patients.

Bibliography

1. Broderick J, Brott T, Kothari R, et al. The Greater Cincinnati/Northern Kentucky Stroke Study: preliminary first-ever and total incidence rates of stroke among blacks. *Stroke; a journal of cerebral circulation.* 1998;29:415-421.

2. Barzilay JI, Spiekerman CF, Kuller LH, et al. Prevalence of clinical and isolated subclinical cardiovascular disease in older adults with glucose disorders - The Cardiovascular Health Study. *Diabetes Care.* 2001;24:1233-1239.

3. Libby P, Zhao DX. Allograft arteriosclerosis and immune-driven angiogenesis. *Circulation.* 2003;107:1237-1239.

4. Virmani R, Kolodgie FD, Burke AP, Farb A, Schwartz SM. Lessons from sudden coronary death: a comprehensive morphological classification scheme for atherosclerotic lesions. *Arterioscler Thromb Vasc Biol.* 2000;20:1262-1275.

5. Lusis AJ. Atherosclerosis. *Nature.* 2000;407:233-241.

6. Hansson GK. Inflammation, atherosclerosis, and coronary artery disease. *N Engl J Med.* 2005;352:1685-1695.

7. Purushothaman KR, Purushothaman M, Muntner P, et al. Inflammation, neovascularization and intra-plaque hemorrhage are associated with increased reparative collagen content: implication for plaque progression in diabetic atherosclerosis. *Vasc Med.* 2011;16:103-108.

8. Fuster D, Magrina J, Ricart MJ, et al. Noninvasive assessment of cardiac risk in type I diabetic patients being evaluated for combined pancreas-kidney transplantation using dipyridamole-MIBI perfusion tomographic scintigraphy. *Transpl Int.* 2000;13:327-332.

9. Blower PJ, Lewis JS, Zweit J. Copper radionuclides and radiopharmaceuticals in nuclear medicine. *Nucl Med Biol.* 1996;23:957-980.

10. Wada K, Fujibayashi Y, Tajima N, Yokoyama A. Cu-ATSM, an intracellular-accessible superoxide dismutase (SOD)-like copper complex: evaluation in an ischemia-reperfusion injury model. *Biol Pharm Bull.* 1994;17:701-704.

11. Fujibayashi Y, Taniuchi H, Yonekura Y, Ohtani H, Konishi J, Yokoyama A. Copper-62-ATSM: a new hypoxia imaging agent with high membrane permeability and low redox potential. *J Nucl Med.* 1997;38:1155-1160.

12. Lewis JS, McCarthy DW, McCarthy TJ, Fujibayashi Y, Welch MJ. Evaluation of 64Cu-ATSM in vitro and in vivo in a hypoxic tumor model. *J Nucl Med.* 1999;40:177-183.

13. Lewis JS, Sharp TL, Laforest R, Fujibayashi Y, Welch MJ. Tumor uptake of copper-diacetyl-bis(N(4)-methylthiosemicarbazone): effect of changes in tissue oxygenation. *J Nucl Med.* 2001;42:655-661.

14. Dehdashti F, Grigsby PW, Mintun MA, Lewis JS, Siegel BA, Welch MJ. Assessing tumor hypoxia in cervical cancer by positron emission tomography with 60Cu-ATSM: relationship to therapeutic response-a preliminary report. *Int J Radiat Oncol Biol Phys.* 2003;55:1233-1238.

15. Rudd JH, Myers KS, Bansilal S, et al. (18)Fluorodeoxyglucose positron emission tomography imaging of atherosclerotic plaque inflammation is highly reproducible: implications for atherosclerosis therapy trials. *J Am Coll Cardiol.* 2007;50:892-896.

16. Bourgeois M, Rajerison H, Guerard F, et al. Contribution of [64Cu]-ATSM PET in molecular imaging of tumour hypoxia compared to classical [18F]-MISO--a selected review. *Nucl Med Rev Cent East Eur.* 2011;14:90-95.

17. Silvola JM, Saraste A, Forsback S, et al. Detection of hypoxia by [18F]EF5 in atherosclerotic plaques in mice. *Arterioscler Thromb Vasc Biol.* 2011;31:1011-1015.

18. Yuan H, Schroeder T, Bowsher JE, Hedlund LW, Wong T, Dewhirst MW. Intertumoral differences in hypoxia selectivity of the PET imaging agent 64Cu(II)-diacetyl-bis(N4-methylthiosemicarbazone). *J Nucl Med.* 2006;47:989-998.

19. O'Donoghue JA, Zanzonico P, Pugachev A, et al. Assessment of regional tumor hypoxia using 18F-fluoromisonidazole and 64Cu(II)-diacetyl-bis(N4-methylthiosemicarbazone) positron emission tomography: Comparative study featuring microPET imaging, Po2 probe measurement, autoradiography, and fluorescent microscopy in the R3327-AT and FaDu rat tumor models. *Int J Radiat Oncol Biol Phys.* 2005;61:1493-1502.

20. Hansen AE, Kristensen AT, Jorgensen JT, et al. (64)Cu-ATSM and (18)FDG PET uptake and (64)Cu-ATSM autoradiography in spontaneous canine tumors: comparison with pimonidazole hypoxia immunohistochemistry. *Radiat Oncol.* 2012;7:89.

21. Carlin S, Zhang H, Reese M, Ramos NN, Chen Q, Ricketts SA. A comparison of the imaging characteristics and microregional distribution of 4 hypoxia PET tracers. *J Nucl Med.* 2014;55:515-521.

22. Valtorta S, Belloli S, Sanvito F, et al. Comparison of 18F-fluoroazomycin-arabinofuranoside and 64Cu-diacetyl-bis(N4-methylthiosemicarbazone) in preclinical models of cancer. *J Nucl Med.* 2013;54:1106-1112.

23. Li F, Jorgensen JT, Forman J, Hansen AE, Kjaer A. 64Cu-ATSM reflects pO2 levels in human head and neck cancer xenografts but not in colorectal cancer xenografts. *J Nucl Med.* 2015.

24. Mayr M, Sidibe A, Zampetaki A. The paradox of hypoxic and oxidative stress in atherosclerosis. *J Am Coll Cardiol.* 2008;51:1266-1267.

25. Janssens GO, Rademakers SE, Terhaard CH, et al. Accelerated radiotherapy with carbogen and nicotinamide for laryngeal cancer: results of a phase III randomized trial. *J Clin Oncol.* 2012;30:1777-1783.

26. Sluimer JC, Gasc JM, van Wanroij JL, et al. Hypoxia, hypoxia-inducible transcription factor, and macrophages in human atherosclerotic plaques are correlated with intraplaque angiogenesis. *J Am Coll Cardiol.* 2008;51:1258-1265.

27. Fujibayashi Y, Cutler CS, Anderson CJ, et al. Comparative studies of Cu-64-ATSM and C-11-acetate in an acute myocardial infarction model: ex vivo imaging of hypoxia in rats. *Nucl Med Biol.* 1999;26:117-121.

28. Takahashi N, Fujibayashi Y, Yonekura Y, et al. Copper-62 ATSM as a hypoxic tissue tracer in myocardial ischemia. *Ann Nucl Med.* 2001;15:293-296.

29. Hoffman JM, Rasey JS, Spence AM, Shaw DW, Krohn KA. Binding of the hypoxia tracer [3H]misonidazole in cerebral ischemia. *Stroke; a journal of cerebral circulation.* 1987;18:168-176.

30. Hulten LM, Levin M. The role of hypoxia in atherosclerosis. *Current Opinion in Lipidology.* 2009;20:409-414.

31. Bjornheden T, Levin M, Evaldsson M, Wiklund O. Evidence of hypoxic areas within the arterial wall in vivo. *Arterioscler Thromb Vasc Biol.* 1999;19:870-876.

32. Hueper WC. Arteriosclerosis. *Archives of Pathology.* 1944;38:0350-0364.

33. Weber C, Zernecke A, Libby P. The multifaceted contributions of leukocyte subsets to atherosclerosis: lessons from mouse models. *Nat Rev Immunol.* 2008;8:802-815.

34. Libby P, Ridker PM, Hansson GK. Progress and challenges in translating the biology of atherosclerosis. *Nature.* 2011;473:317-325.

35. Ross R. Atherosclerosis is an inflammatory disease. *Am Heart J.* 1999;138:S419-420.

36. Moreno PR. Vulnerable plaque: definition, diagnosis, and treatment. *Cardiol Clin.* 2010;28:1-30.

37. Finn AV, Nakano M, Narula J, Kolodgie FD, Virmani R. Concept of vulnerable/unstable plaque. *Arterioscler Thromb Vasc Biol.* 2010;30:1282-1292.

38. Didangelos A, Simper D, Monaco C, Mayr M. Proteomics of acute coronary syndromes. *Curr Atheroscler Rep.* 2009;11:188-195.

39. Ross R. Atherosclerosis--an inflammatory disease. *N Engl J Med.* 1999;340:115-126.

40. Ross R. The pathogenesis of atherosclerosis: a perspective for the 1990s. *Nature.* 1993;362:801-809.

41. Fuster V, Moreno PR, Fayad ZA, Corti R, Badimon JJ. Atherothrombosis and high-risk plaque: part I: evolving concepts. *J Am Coll Cardiol.* 2005;46:937-954.

42. Tabas I, Williams KJ, Boren J. Subendothelial lipoprotein retention as the initiating process in atherosclerosis: update and therapeutic implications. *Circulation.* 2007;116:1832-1844.

43. Bjornheden T, Bondjers G. Oxygen consumption in aortic tissue from rabbits with diet-induced atherosclerosis. *Arteriosclerosis.* 1987;7:238-247.

44. Ribatti D, Levi-Schaffer F, Kovanen PT. Inflammatory angiogenesis in atherogenesis--a double-edged sword. *Ann Med.* 2008;40:606-621.

45. Nakashima Y, Wight TN, Sueishi K. Early atherosclerosis in humans: role of diffuse intimal thickening and extracellular matrix proteoglycans. *Cardiovasc Res.* 2008;79:14-23.

46. Stary HC. Lipid and macrophage accumulations in arteries of children and the development of atherosclerosis. *Am J Clin Nutr.* 2000;72:1297S-1306S.

47. Bostrom P, Magnusson B, Svensson PA, et al. Hypoxia converts human macrophages into triglyceride-loaded foam cells. *Arterioscler Thromb Vasc Biol.* 2006;26:1871-1876.

48. Rydberg EK, Salomonsson L, Hulten LM, et al. Hypoxia increases 25-hydroxycholesterol-induced interleukin-8 protein secretion in human macrophages. *Atherosclerosis.* 2003;170:245-252.

49. Hulten LM, Levin M. The role of hypoxia in atherosclerosis. *Current Opinion in Lipidology.* 2009;20:409-414.

50. Rydberg EK, Krettek A, Ullstrom C, et al. Hypoxia increases LDL oxidation and expression of 15-lipoxygenase-2 in human macrophages. *Arterioscler Thromb Vasc Biol.* 2004;24:2040-2045.

51. Leppanen O, Bjornheden T, Evaldsson M, Boren J, Wiklund O, Levin M. ATP depletion in macrophages in the core of advanced rabbit atherosclerotic plaques in vivo. *Atherosclerosis.* 2006;188:323-330.

52. Oorni K, Kovanen PT. Enhanced extracellular lipid accumulation in acidic environments. *Current Opinion in Lipidology.* 2006;17:534-540.

53. Sneck M, Kovanen PT, Oorni K. Decrease in pH strongly enhances binding of native, proteolyzed, lipolyzed, and oxidized low density lipoprotein particles to human aortic proteoglycans. *J Biol Chem.* 2005;280:37449-37454.

54. Brown MS, Ho YK, Goldstein JL. The cholesteryl ester cycle in macrophage foam cells. Continual hydrolysis and re-esterification of cytoplasmic cholesteryl esters. *J Biol Chem.* 1980;255:9344-9352.

55. Fraisl P, Mazzone M, Schmidt T, Carmeliet P. Regulation of angiogenesis by oxygen and metabolism. *Dev Cell.* 2009;16:167-179.

56. Sluimer JC, Daemen MJ. Novel concepts in atherogenesis: angiogenesis and hypoxia in atherosclerosis. *J Pathol.* 2009;218:7-29.

57. Moulton KS, Heller E, Konerding MA, Flynn E, Palinski W, Folkman J. Angiogenesis inhibitors endostatin or TNP-470 reduce intimal neovascularization and plaque growth in apolipoprotein E-deficient mice. *Circulation.* 1999;99:1726-1732.

58. Moulton KS, Vakili K, Zurakowski D, et al. Inhibition of plaque neovascularization reduces macrophage accumulation and progression of advanced atherosclerosis. *Proc Natl Acad Sci U S A.* 2003;100:4736-4741.

59. Virmani R, Kolodgie FD, Burke AP, et al. Atherosclerotic plaque progression and vulnerability to rupture: angiogenesis as a source of intraplaque hemorrhage. *Arterioscler Thromb Vasc Biol.* 2005;25:2054-2061.

60. Carmeliet P. VEGF as a key mediator of angiogenesis in cancer. *Oncology.* 2005;69 Suppl 3:4-10.

61. Semenza GL. Regulation of physiological responses to continuous and intermittent hypoxia by hypoxia-inducible factor 1. *Exp Physiol.* 2006;91:803-806.

62. Walsh JC, Lebedev A, Aten E, Madsen K, Marciano L, Kolb HC. The clinical importance of assessing tumor hypoxia: relationship of tumor hypoxia to prognosis and therapeutic opportunities. *Antioxid Redox Signal.* 2014;21:1516-1554.

63. Hockel M, Vaupel P. Tumor hypoxia: definitions and current clinical, biologic, and molecular aspects. *J Natl Cancer Inst.* 2001;93:266-276.

64. Lopci E, Grassi I, Chiti A, et al. PET radiopharmaceuticals for imaging of tumor hypoxia: a review of the evidence. *Am J Nucl Med Mol Imaging.* 2014;4:365-384.

65. Vikram DS, Zweier JL, Kuppusamy P. Methods for noninvasive imaging of tissue hypoxia. *Antioxid Redox Signal.* 2007;9:1745-1756.

66. Lapi SE, Voller TF, Welch MJ. Positron Emission Tomography Imaging of Hypoxia. *PET Clin.* 2009;4:39-47.

67. Wang W, Lee NY, Georgi JC, et al. Pharmacokinetic analysis of hypoxia (18)F-fluoromisonidazole dynamic PET in head and neck cancer. *J Nucl Med.* 2010;51:37-45.

68. Price JM, Robinson SP, Koh DM. Imaging hypoxia in tumours with advanced MRI. *Q J Nucl Med Mol Imaging.* 2013;57:257-270.

69. Chapman JD, Franko AJ, Sharplin J. A marker for hypoxic cells in tumours with potential clinical applicability. *Br J Cancer.* 1981;43:546-550.

70. Mees G, Dierckx R, Vangestel C, Van de Wiele C. Molecular imaging of hypoxia with radiolabelled agents. *Eur J Nucl Med Mol Imaging.* 2009;36:1674-1686.

71. Dierckx RA, Van de Wiele C. FDG uptake, a surrogate of tumour hypoxia? *Eur J Nucl Med Mol Imaging.* 2008;35:1544-1549.

72. Folco EJ, Sheikine Y, Rocha VZ, et al. Hypoxia but not inflammation augments glucose uptake in human macrophages: Implications for imaging atherosclerosis with 18fluorine-labeled 2-deoxy-D-glucose positron emission tomography. *J Am Coll Cardiol.* 2011;58:603-614.

73. van Baardwijk A, Dooms C, van Suylen RJ, et al. The maximum uptake of (18)F-deoxyglucose on positron emission tomography scan correlates with survival, hypoxia inducible factor-1alpha and GLUT-1 in non-small cell lung cancer. *Eur J Cancer.* 2007;43:1392-1398.

74. Busk M, Horsman MR, Kristjansen PE, van der Kogel AJ, Bussink J, Overgaard J. Aerobic glycolysis in cancers: implications for the usability of oxygen-responsive genes and fluorodeoxyglucose-PET as markers of tissue hypoxia. *International Journal of Cancer.* 2008;122:2726-2734.

75. Warburg O. On respiratory impairment in cancer cells. *Science.* 1956;124:269-270.

76. Kaira K, Okumura T, Ohde Y, et al. Correlation between 18F-FDG uptake on PET and molecular biology in metastatic pulmonary tumors. *J Nucl Med.* 2011;52:705-711.

77. Airley RE, Mobasheri A. Hypoxic regulation of glucose transport, anaerobic metabolism and angiogenesis in cancer: novel pathways and targets for anticancer therapeutics. *Chemotherapy.* 2007;53:233-256.

78. Kim JW, Gao P, Dang CV. Effects of hypoxia on tumor metabolism. *Cancer Metastasis Rev.* 2007;26:291-298.

79. Martin GV, Caldwell JH, Graham MM, et al. Noninvasive detection of hypoxic myocardium using fluorine-18-fluoromisonidazole and positron emission tomography. *J Nucl Med.* 1992;33:2202-2208.

80. Sorger D, Patt M, Kumar P, et al. [18F]Fluoroazomycinarabinofuranoside (18FAZA) and [18F]Fluoromisonidazole (18FMISO): a comparative study of their selective uptake in hypoxic cells and PET imaging in experimental rat tumors. *Nucl Med Biol.* 2003;30:317-326.

81. Piert M, Machulla HJ, Picchio M, et al. Hypoxia-specific tumor imaging with 18F-fluoroazomycin arabinoside. *J Nucl Med.* 2005;46:106-113.

82. Okada RD, Johnson G, 3rd, Nguyen KN, Edwards B, Archer CM, Kelly JD. 99mTc-HL91. Effects of low flow and hypoxia on a new ischemia-avid myocardial imaging agent. *Circulation.* 1997;95:1892-1899.

83. Jerabek PA, Patrick TB, Kilbourn MR, Dischino DD, Welch MJ. Synthesis and biodistribution of 18F-labeled fluoronitroimidazoles: potential in vivo markers of hypoxic tissue. *Int J Rad Appl Instrum A.* 1986;37:599-605.

84. Grierson JR, Link JM, Mathis CA, Rasey JS, Krohn KA. A radiosynthesis of fluorine-18 fluoromisonidazole. *J Nucl Med.* 1989;30:343-350.

85. Hoigebazar L, Jeong JM. Hypoxia imaging agents labeled with positron emitters. *Recent Results Cancer Res.* 2013;194:285-299.

86. Takasawa M, Moustafa RR, Baron JC. Applications of nitroimidazole in vivo hypoxia imaging in ischemic stroke. *Stroke; a journal of cerebral circulation.* 2008;39:1629-1637.

87. Cher LM, Murone C, Lawrentschuk N, et al. Correlation of hypoxic cell fraction and angiogenesis with glucose metabolic rate in gliomas using 18F-fluoromisonidazole, 18F-FDG PET, and immunohistochemical studies. *J Nucl Med.* 2006;47:410-418.

88. Eschmann SM, Paulsen F, Reimold M, et al. Prognostic impact of hypoxia imaging with 18F-misonidazole PET in non-small cell lung cancer and head and neck cancer before radiotherapy. *J Nucl Med.* 2005;46:253-260.

89. Valk PE, Mathis CA, Prados MD, Gilbert JC, Budinger TF. Hypoxia in human gliomas: demonstration by PET with fluorine-18-fluoromisonidazole. *J Nucl Med.* 1992;33:2133-2137.

90. Lee NY, Mechalakos JG, Nehmeh S, et al. Fluorine-18-labeled fluoromisonidazole positron emission and computed tomography-guided intensity-modulated radiotherapy for head and neck cancer: a feasibility study. *Int J Radiat Oncol Biol Phys.* 2008;70:2-13.

91. Arabi M, Piert M. Hypoxia PET/CT imaging: implications for radiation oncology. *Q J Nucl Med Mol Imaging.* 2010;54:500-509.

92. Nunn A, Linder K, Strauss HW. Nitroimidazoles and imaging hypoxia. *Eur J Nucl Med.* 1995;22:265-280.

93. Vavere AL, Lewis JS. Cu-ATSM: a radiopharmaceutical for the PET imaging of hypoxia. *Dalton Trans.* 2007:4893-4902.

94. McQuade P, Martin KE, Castle TC, et al. Investigation into 64Cu-labeled Bis(selenosemicarbazone) and Bis(thiosemicarbazone) complexes as hypoxia imaging agents. *Nucl Med Biol.* 2005;32:147-156.

95. McCarthy DW, Shefer RE, Klinkowstein RE, et al. Efficient production of high specific activity 64Cu using a biomedical cyclotron. *Nucl Med Biol.* 1997;24:35-43.

96. Jodal L, Le Loirec C, Champion C. Positron range in PET imaging: non-conventional isotopes. *Phys Med Biol.* 2014;59:7419-7434.

97. Phelps ME, Hoffman EJ, Huang SC, Ter-Pogossian MM. Effect of positron range on spatial resolution. *J Nucl Med.* 1975;16:649-652.

98. Takahashi N, Fujibayashi Y, Yonekura Y, et al. Evaluation of 62Cu labeled diacetyl-bis(N4-methylthiosemicarbazone) as a hypoxic tissue tracer in patients with lung cancer. *Ann Nucl Med.* 2000;14:323-328.

99. Hockel M, Knoop C, Schlenger K, et al. Intratumoral pO2 predicts survival in advanced cancer of the uterine cervix. *Radiotherapy and Oncology.* 1993;26:45-50.

100. Dearling JL, Lewis JS, Mullen GE, Rae MT, Zweit J, Blower PJ. Design of hypoxia-targeting radiopharmaceuticals: selective uptake of copper-64 complexes in hypoxic cells in vitro. *Eur J Nucl Med.* 1998;25:788-792.

101. Dehdashti F, Mintun MA, Lewis JS, et al. In vivo assessment of tumor hypoxia in lung cancer with 60Cu-ATSM. *Eur J Nucl Med Mol Imaging.* 2003;30:844-850.

102. Dearling JL, Lewis JS, Mullen GE, Welch MJ, Blower PJ. Copper bis(thiosemicarbazone) complexes as hypoxia imaging agents: structure-activity relationships. *J Biol Inorg Chem.* 2002;7:249-259.

103. Burgman P, O'Donoghue JA, Lewis JS, Welch MJ, Humm JL, Ling CC. Cell line-dependent differences in uptake and retention of the hypoxia-selective nuclear imaging agent Cu-ATSM. *Nucl Med Biol.* 2005;32:623-630.

104. Maurer RI, Blower PJ, Dilworth JR, Reynolds CA, Zheng Y, Mullen GE. Studies on the mechanism of hypoxic selectivity in copper bis(thiosemicarbazone) radiopharmaceuticals. *J Med Chem.* 2002;45:1420-1431.

105. Kume M, Carey PC, Gaehle G, et al. A semi-automated system for the routine production of copper-64. *Appl Radiat Isot.* 2012;70:1803-1806.

106. Nie X, Randolph GJ, Elvington A, et al. Imaging of hypoxia in mouse atherosclerotic plaques with (64)Cu-ATSM. *Nucl Med Biol.* 2016;43:534-542.

107. Khallou-Laschet J, Varthaman A, Fornasa G, et al. Macrophage plasticity in experimental atherosclerosis. *PLoS One.* 2010;5:e8852.

108. Zhang SH, Reddick RL, Piedrahita JA, Maeda N. Spontaneous hypercholesterolemia and arterial lesions in mice lacking apolipoprotein E. *Science.* 1992;258:468-471.

109. Stary HC, Chandler AB, Dinsmore RE, et al. A definition of advanced types of atherosclerotic lesions and a histological classification of atherosclerosis. A report from the Committee on Vascular Lesions of the Council on Arteriosclerosis, American Heart Association. *Circulation.* 1995;92:1355-1374.

110. Duivenvoorden R, Tang J, Cormode DP, et al. A statin-loaded reconstituted high-density lipoprotein nanoparticle inhibits atherosclerotic plaque inflammation. *Nat Commun.* 2014;5:3065.

111. Amirbekian V, Lipinski MJ, Briley-Saebo KC, et al. Detecting and assessing macrophages in vivo to evaluate atherosclerosis noninvasively using molecular MRI. *Proc Natl Acad Sci U S A.* 2007;104:961-966.

112. Tacke F, Alvarez D, Kaplan TJ, et al. Monocyte subsets differentially employ CCR2, CCR5, and CX3CR1 to accumulate within atherosclerotic plaques. *J Clin Invest.* 2007;117:185-194.

113. Angheloiu GO, van de Poll SW, Georgakoudi I, et al. Intrinsic versus laser-induced fluorescence spectroscopy for coronary atherosclerosis: a generational comparison model for testing diagnostic accuracy. *Appl Spectrosc.* 2012;66:1403-1410.

114. Potteaux S, Gautier EL, Hutchison SB, et al. Suppressed monocyte recruitment drives macrophage removal from atherosclerotic plaques of Apoe-/- mice during disease regression. *J Clin Invest.* 2011;121:2025-2036.

115. Hag AM, Pedersen SF, Christoffersen C, et al. (18)F-FDG PET imaging of murine atherosclerosis: association with gene expression of key molecular markers. *PLoS One.* 2012;7:e50908.

116. Gray RE, Fitch M, Saunders PR, et al. Complementary health practitioners' attitudes, practices and knowledge related to women's cancers. *Cancer Prev Control.* 1999;3:77-82.

117. Bends A, Burns C, Yellowman-Caye P, et al. Community-university Research Liaisons: Translating the Languages of Research and Culture. *Pimatisiwin.* 2013;11:345-357.

118. Smith JD, Trogan E, Ginsberg M, Grigaux C, Tian J, Miyata M. Decreased atherosclerosis in mice deficient in both macrophage colony-stimulating factor (op) and apolipoprotein E. *Proc Natl Acad Sci U S A.* 1995;92:8264-8268.

119. Mateo J, Izquierdo-Garcia D, Badimon JJ, Fayad ZA, Fuster V. Noninvasive assessment of hypoxia in rabbit advanced atherosclerosis using (1)(8)F-fluoromisonidazole positron emission tomographic imaging. *Circ Cardiovasc Imaging.* 2014;7:312-320.

120. Furukawa T, Yuan Q, Jin ZH, et al. A limited overlap between intratumoral distribution of 1-(5-fluoro-5-deoxy-alpha-D-arabinofuranosyl)-2-nitroimidazole and copper-diacetyl-bis[N(4)-methylthiosemicarbazone]. *Oncol Rep.* 2015;34:1379-1387.

121. Bowen SR, van der Kogel AJ, Nordsmark M, Bentzen SM, Jeraj R. Characterization of positron emission tomography hypoxia tracer uptake and tissue oxygenation via electrochemical modeling. *Nucl Med Biol.* 2011;38:771-780.

122. Brown JM, Wilson WR. Exploiting tumour hypoxia in cancer treatment. *Nat Rev Cancer.* 2004;4:437-447.

123. Colombie M, Gouard S, Frindel M, et al. Focus on the Controversial Aspects of (64)Cu-ATSM in Tumoral Hypoxia Mapping by PET Imaging. *Front Med (Lausanne).* 2015;2:58.

124. Vavere AL, Lewis JS. Examining the relationship between Cu-ATSM hypoxia selectivity and fatty acid synthase expression in human prostate cancer cell lines. *Nucl Med Biol.* 2008;35:273-279.

125. Zhang Z, Machac J, Helft G, et al. Non-invasive imaging of atherosclerotic plaque macrophage in a rabbit model with F-18 FDG PET: a histopathological correlation. *BMC Nucl Med.* 2006;6:3.

126. Handley MG, Medina RA, Nagel E, Blower PJ, Southworth R. PET imaging of cardiac hypoxia: opportunities and challenges. *J Mol Cell Cardiol.* 2011;51:640-650.

127. Carli M. FDG Imaging of Atherosclerosis: How Good is the Evidence? : Society of Nuclear Medicine and Molecular Imaging.

128. Rudd JH, Myers KS, Bansilal S, et al. Atherosclerosis inflammation imaging with 18F-FDG PET: carotid, iliac, and femoral uptake reproducibility, quantification methods, and recommendations. *J Nucl Med.* 2008;49:871-878.

129. Gao L, Chen Q, Zhou X, Fan L. The role of hypoxia-inducible factor 1 in atherosclerosis. *Journal of Clinical Pathology.* 2012;65:872-876.

130. Casteleyn C, Trachet B, Van Loo D, et al. Validation of the murine aortic arch as a model to study human vascular diseases. *Journal of Anatomy.* 2010;216:563-571.

131. Nie XY, Laforest R, Zheng J, et al. PET/MR imaging of hypoxic atherosclerosis using Cu-64-ATSM in a rabbit model. *Journal of Nuclear Medicine.* 2015;56.

132. Zheng J, Ochoa E, Misselwitz B, et al. Targeted contrast agent helps to monitor advanced plaque during progression: a magnetic resonance imaging study in rabbits. *Invest Radiol.* 2008;43:49-55.

133. Liu Y, Abendschein D, Woodard GE, et al. Molecular imaging of atherosclerotic plaque with (64)Cu-labeled natriuretic peptide and PET. *J Nucl Med.* 2010;51:85-91.

134. Delso G, Furst S, Jakoby B, et al. Performance measurements of the Siemens mMR integrated whole-body PET/MR scanner. *J Nucl Med.* 2011;52:1914-1922.

135. Rischpler C, Nekolla SG, Beer AJ. PET/MR imaging of atherosclerosis: initial experience and outlook. *Am J Nucl Med Mol Imaging.* 2013;3:393-396.

136. Saam T, Hatsukami TS, Takaya N, et al. The vulnerable, or high-risk, atherosclerotic plaque: noninvasive MR imaging for characterization and assessment. *Radiology.* 2007;244:64-77.

137. Rudd JH, Warburton EA, Fryer TD, et al. Imaging atherosclerotic plaque inflammation with [18F]-fluorodeoxyglucose positron emission tomography. *Circulation.* 2002;105:2708-2711.

138. Temma T, Saji H. Radiolabelled probes for imaging of atherosclerotic plaques. *Am J Nucl Med Mol Imaging.* 2012;2:432-447.

139. Nolting DD, Nickels ML, Guo N, Pham W. Molecular imaging probe development: a chemistry perspective. *Am J Nucl Med Mol Imaging.* 2012;2:273-306.

140. Balyasnikova S, Lofgren J, de Nijs R, Zamogilnaya Y, Hojgaard L, Fischer BM. PET/MR in oncology: an introduction with focus on MR and future perspectives for hybrid imaging. *Am J Nucl Med Mol Imaging.* 2012;2:458-474.

141. Dehne N, Brune B. HIF-1 in the inflammatory microenvironment. *Exp Cell Res.* 2009;315:1791-1797.

142. Mazziotta JC, Phelps ME, Plummer D, Kuhl DE. Quantitation in positron emission computed tomography: 5. Physical--anatomical effects. *J Comput Assist Tomogr.* 1981;5:734-743.

143. Izquierdo-Garcia D, Davies JR, Graves MJ, et al. Comparison of methods for magnetic resonance-guided [18-F]fluorodeoxyglucose positron emission tomography in human carotid arteries: reproducibility, partial volume correction, and correlation between methods. *Stroke; a journal of cerebral circulation.* 2009;40:86-93.

144. Hoffman EJ, Huang SC, Phelps ME. Quantitation in positron emission computed tomography: 1. Effect of object size. *J Comput Assist Tomogr.* 1979;3:299-308.

145. Biograph mMR: Technical Details. http://www.healthcare.siemens.com/magnetic-resonance-imaging/mr-pet-scanner/biograph-mmr/technical-details.

146. Chang T-S. *Techniques and Applications in Microsurgery*.

147. Ripa RS, Kjaer A. Imaging atherosclerosis with hybrid positron emission tomography/magnetic resonance imaging. *Biomed Res Int.* 2015;2015:914516.

148. Wang J, Liu H, Sun J, et al. Varying correlation between 18F-fluorodeoxyglucose positron emission tomography and dynamic contrast-enhanced MRI in carotid atherosclerosis: implications for plaque inflammation. *Stroke; a journal of cerebral circulation.* 2014;45:1842-1845.

149. Truijman MT, Kwee RM, van Hoof RH, et al. Combined 18F-FDG PET-CT and DCE-MRI to assess inflammation and microvascularization in atherosclerotic plaques. *Stroke; a journal of cerebral circulation.* 2013;44:3568-3570.

150. Saito H, Kuroda S, Hirata K, et al. Validity of dual MRI and F-FDG PET imaging in predicting vulnerable and inflamed carotid plaque. *Cerebrovasc Dis.* 2013;35:370-377.

151. Calcagno C, Ramachandran S, Izquierdo-Garcia D, et al. The complementary roles of dynamic contrast-enhanced MRI and 18F-fluorodeoxyglucose PET/CT for imaging of carotid atherosclerosis. *Eur J Nucl Med Mol Imaging.* 2013;40:1884-1893.

152. Silvera SS, Aidi HE, Rudd JH, et al. Multimodality imaging of atherosclerotic plaque activity and composition using FDG-PET/CT and MRI in carotid and femoral arteries. *Atherosclerosis.* 2009;207:139-143.

153. Aasi J, Abadie J, Abbott BP, et al. Constraints on cosmic strings from the LIGO-Virgo gravitational-wave detectors. *Phys Rev Lett.* 2014;112:131101.

154. Huang X, Yang C, Yuan C, et al. Patient-specific artery shrinkage and 3D zero-stress state in multi-component 3D FSI models for carotid atherosclerotic plaques based on in vivo MRI data. *Mol Cell Biomech.* 2009;6:121-134.

155. Parker GJ, Roberts C, Macdonald A, et al. Experimentally-derived functional form for a population-averaged high-temporal-resolution arterial input function for dynamic contrast-enhanced MRI. *Magn Reson Med.* 2006;56:993-1000.

156. Tofts PS. Modeling tracer kinetics in dynamic Gd-DTPA MR imaging. *J Magn Reson Imaging.* 1997;7:91-101.

157. Duguet A, Tantucci C, Lozinguez O, et al. Expiratory flow limitation as a determinant of orthopnea in acute left heart failure. *J Am Coll Cardiol.* 2000;35:690-700.

158. A Primer on Perfusion MRI. *Pharmascan Clinical Trials*.

159. Kolodgie FD, Gold HK, Burke AP, et al. Intraplaque hemorrhage and progression of coronary atheroma. *N Engl J Med.* 2003;349:2316-2325.

160. Moreno PR, Purushothaman KR, Zias E, Sanz J, Fuster V. Neovascularization in human atherosclerosis. *Curr Mol Med.* 2006;6:457-477.

161. Kerwin W, Hooker A, Spilker M, et al. Quantitative magnetic resonance imaging analysis of neovasculature volume in carotid atherosclerotic plaque. *Circulation.* 2003;107:851-856.

162. Kerwin WS, O'Brien KD, Ferguson MS, Polissar N, Hatsukami TS, Yuan C. Inflammation in carotid atherosclerotic plaque: a dynamic contrast-enhanced MR imaging study. *Radiology.* 2006;241:459-468.

163. Kerwin WS, Oikawa M, Yuan C, Jarvik GP, Hatsukami TS. MR imaging of adventitial vasa vasorum in carotid atherosclerosis. *Magn Reson Med.* 2008;59:507-514.

164. Calcagno C, Mani V, Ramachandran S, Fayad ZA. Dynamic contrast enhanced (DCE) magnetic resonance imaging (MRI) of atherosclerotic plaque angiogenesis. *Angiogenesis.* 2010;13:87-99.

165. Calcagno C, Lobatto ME, Dyvorne H, et al. Three-dimensional dynamic contrast-enhanced MRI for the accurate, extensive quantification of microvascular permeability in atherosclerotic plaques. *NMR Biomed.* 2015;28:1304-1314.

166. Vucic E, Dickson SD, Calcagno C, et al. Pioglitazone Modulates Vascular Inflammation in Atherosclerotic Rabbits Noninvasive Assessment With FDG-PET-CT and Dynamic Contrast-Enhanced MR Imaging. *Jacc-Cardiovascular Imaging.* 2011;4:1100-1109.

167. Calcagno C, Ramachandran S, Izquierdo-Garcia D, et al. The complementary roles of dynamic contrast-enhanced MRI and F-18-fluorodeoxyglucose PET/CT for imaging of carotid atherosclerosis. *Eur J Nucl Med Mol Imaging.* 2013;40:1884-1893.

168. Kerwin WS, O'Brien KD, Ferguson MS, Polissar N, Hatsukami TS, Yuan C. Inflammation in carotid atherosclerotic plaque: A dynamic contrast-enhanced MR imaging study. *Radiology.* 2006;241:459-468.

169. Kerwin WS, Oikawa M, Yuan C, Jarvik GP, Hatsukami TS. MR imaging of adventitial vasa vasorum in carotid atherosclerosis. *Magnetic Resonance in Medicine.* 2008;59:507-514.

170. Sun J, Song Y, Chen HJ, et al. Adventitial Perfusion and Intraplaque Hemorrhage A Dynamic Contrast-Enhanced MRI Study in the Carotid Artery. *Stroke; a journal of cerebral circulation.* 2013;44:1031-+.

171. Wang J, Liu HB, Sun J, et al. Varying Correlation Between F-18-Fluorodeoxyglucose Positron Emission Tomography and Dynamic Contrast-Enhanced MRI in Carotid Atherosclerosis Implications for Plaque Inflammation. *Stroke; a journal of cerebral circulation.* 2014;45:1842-1845.

172. Truijman MTB, Kwee RM, van Hoof RHM, et al. Combined F-18-FDG PET-CT and DCE-MRI to Assess Inflammation and Microvascularization in Atherosclerotic Plaques. *Stroke; a journal of cerebral circulation.* 2013;44:3568-3570.

173. van Hoof RH, Heeneman S, Wildberger JE, Kooi ME. Dynamic Contrast-Enhanced MRI to Study Atherosclerotic Plaque Microvasculature. *Curr Atheroscler Rep.* 2016;18:33.

174. Tofts PS, Brix G, Buckley DL, et al. Estimating kinetic parameters from dynamic contrast-enhanced T(1)-weighted MRI of a diffusable tracer: standardized quantities and symbols. *J Magn Reson Imaging.* 1999;10:223-232.

175. Tofts PS, Kermode AG. Measurement of the blood-brain barrier permeability and leakage space using dynamic MR imaging. 1. Fundamental concepts. *Magn Reson Med.* 1991;17:357-367.

176. Patlak CS, Blasberg RG, Fenstermacher JD. Graphical evaluation of blood-to-brain transfer constants from multiple-time uptake data. *J Cereb Blood Flow Metab.* 1983;3:1-7.

177. Chen H, Li F, Zhao X, Yuan C, Rutt B, Kerwin WS. Extended graphical model for analysis of dynamic contrast-enhanced MRI. *Magn Reson Med.* 2011;66:868-878.

178. Gaens ME, Backes WH, Rozel S, et al. Dynamic contrast-enhanced MR imaging of carotid atherosclerotic plaque: model selection, reproducibility, and validation. *Radiology.* 2013;266:271-279.

179. Aerts HJWL, van Riel NAW, Backes WH. System identification theory in pharmacokinetic modeling of dynamic contrast-enhanced MRI: Influence of contrast injection. *Magnetic Resonance in Medicine.* 2008;59:1111-1119.

180. van Hoof RH, Hermeling E, Truijman MT, et al. Phase-based vascular input function: Improved quantitative DCE-MRI of atherosclerotic plaques. *Med Phys.* 2015;42:4619-4628.

181. Rothwell PM, Eliasziw M, Gutnikov SA, et al. Analysis of pooled data from the randomised controlled trials of endarterectomy for symptomatic carotid stenosis. *Lancet.* 2003;361:107-116.

182. Henze E, Huang SC, Ratib O, Hoffman E, Phelps ME, Schelbert HR. Measurements of regional tissue and blood-pool radiotracer concentrations from serial tomographic images of the heart. *J Nucl Med.* 1983;24:987-996.

183. Kessler RM, Ellis JR, Jr., Eden M. Analysis of emission tomographic scan data: limitations imposed by resolution and background. *J Comput Assist Tomogr.* 1984;8:514-522.

184. Rousset O, Ma Y, Kamber M, Evans AC. 3D simulations of radiotracer uptake in deep nuclei of human brain. *Comput Med Imaging Graph.* 1993;17:373-379.

185. Links JM, Zubieta JK, Meltzer CC, Stumpf MJ, Frost JJ. Influence of spatially heterogeneous background activity on "hot object" quantitation in brain emission computed tomography. *J Comput Assist Tomogr.* 1996;20:680-687.

186. Rousset OG, Ma Y, Evans AC. Correction for partial volume effects in PET: principle and validation. *J Nucl Med.* 1998;39:904-911.

187. Limbu YR, Gurung G, Malla R, Rajbhandari R, Regmi SR. Assessment of carotid artery dimensions by ultrasound in non-smoker healthy adults of both sexes. *Nepal Med Coll J.* 2006;8:200-203.

188. Muehllehner G. Letter: Resolution limit of positron cameras. *J Nucl Med.* 1976;17:757-758.

189. Derenzo SE, Budinger TF. Resolution limit for positron-imaging devices. *J Nucl Med.* 1977;18:491-492.

190. Moses WW. Fundamental Limits of Spatial Resolution in PET. *Nucl Instrum Methods Phys Res A.* 2011;648 Supplement 1:S236-S240.

191. Erlandsson K, Buvat I, Pretorius PH, Thomas BA, Hutton BF. A review of partial volume correction techniques for emission tomography and their applications in neurology, cardiology and oncology. *Phys Med Biol.* 2012;57:R119-159.

192. Rapisarda E, Bettinardi V, Thielemans K, Gilardi MC. Image-based point spread function implementation in a fully 3D OSEM reconstruction algorithm for PET. *Phys Med Biol.* 2010;55:4131-4151.

193. Hoffman EJ, Huang SC, Plummer D, Phelps ME. Quantitation in positron emission computed tomography: 6. effect of nonuniform resolution. *J Comput Assist Tomogr.* 1982;6:987-999.

194. Qi JY, Leahy RM, Cherry SR, Chatziioannou A, Farquhar TH. High-resolution 3D Bayesian image reconstruction using the microPET small-animal scanner. *Phys Med Biol.* 1998;43:1001-1013.

195. Alessio AM, Kinahan PE, Lewellen TK. Modeling and incorporation of system response functions in 3-D whole body PET. *IEEE Trans Med Imaging.* 2006;25:828-837.

196. Panin VY, Kehren F, Michel C, Casey M. Fully 3-D PET reconstruction with system matrix derived from point source measurements. *IEEE Trans Med Imaging.* 2006;25:907-921.

197. Reader AJ, Julyan PJ, Williams H, Hastings DL, Zweit J. EM algorithm system modeling by image-space techniques for PET reconstruction. *Ieee Transactions on Nuclear Science.* 2003;50:1392-1397.

198. Sureau FC, Reader AJ, Comtat C, et al. Impact of image-space resolution modeling for studies with the high-resolution research tomograph. *Journal of Nuclear Medicine.* 2008;49:1000-1008.

199. Strul D, Bendriem B. Robustness of anatomically guided pixel-by-pixel algorithms for partial volume effect correction in positron emission tomography. *J Cereb Blood Flow Metab.* 1999;19:547-559.

200. Wang H, Fei B. An MR image-guided, voxel-based partial volume correction method for PET images. *Med Phys.* 2012;39:179-195.

201. imaging technolgy news. *Siemens Reconstructs PET in High Definition*; 2007.

202. SIEMENS Healthineers. *Biograph mMR* 2016.

203. Hudson HM, Larkin RS. Accelerated Image-Reconstruction Using Ordered Subsets of Projection Data. *IEEE Trans Med Imaging.* 1994;13:601-609.

204. Holte S, Schmidlin P, Linden A, Rosenqvist G, Eriksson L. Iterative Image-Reconstruction for Positron Emission Tomography - a Study of Convergence and Quantitation Problems. *Ieee Transactions on Nuclear Science.* 1990;37:629-635.

205. Boellaard R, van Lingen A, Lammertsma AA. Experimental and clinical evaluation of iterative reconstruction (OSEM) in dynamic PET: Quantitative characteristics and effects on kinetic modeling. *Journal of Nuclear Medicine.* 2001;42:808-817.

206. Wang CX, Snyder WE, Bilbro G, Santago P. Performance evaluation of filtered backprojection reconstruction and iterative reconstruction methods for PET images. *Computers in Biology and Medicine.* 1998;28:13-25.

207. Chen GP, Branch KR, Alessio AM, et al. Effect of reconstruction algorithms on myocardial blood flow measurement with N-13-ammonia PET. *Journal of Nuclear Medicine.* 2007;48:1259-1265.

208. Qi J, Leahy RM. Iterative reconstruction techniques in emission computed tomography. *Phys Med Biol.* 2006;51:R541-578.

209. Shepp LA, Vardi Y. Maximum likelihood reconstruction for emission tomography. *IEEE Trans Med Imaging.* 1982;1:113-122.

210. Lange K, Carson R. EM reconstruction algorithms for emission and transmission tomography. *J Comput Assist Tomogr.* 1984;8:306-316.

211. Hudson HM, Larkin RS. Accelerated image reconstruction using ordered subsets of projection data. *IEEE Trans Med Imaging.* 1994;13:601-609.

212. Qi J, Leahy RM, Cherry SR, Chatziioannou A, Farquhar TH. High-resolution 3D Bayesian image reconstruction using the microPET small-animal scanner. *Phys Med Biol.* 1998;43:1001-1013.

213. Mumcuoglu EU, Leahy RM, Cherry SR. Bayesian reconstruction of PET images: methodology and performance analysis. *Phys Med Biol.* 1996;41:1777-1807.

214. Lodge MA, Rahmim A, Wahl RL. A practical, automated quality assurance method for measuring spatial resolution in PET. *J Nucl Med.* 2009;50:1307-1314.

215. Richards.Wh. Bayesian-Based Iterative Method of Image Restoration. *Journal of the Optical Society of America.* 1972;62:55-&.

216. Lucy LB. Iterative Technique for Rectification of Observed Distributions. *Astronomical Journal.* 1974;79:745-754.

217. Dey N, Blanc-Feraud L, Zimmer C, et al. Richardson-Lucy algorithm with total variation regularization for 3D confocal microscope deconvolution. *Microsc Res Tech.* 2006;69:260-266.

218. Topping GJ, Schaffer P, Hoehr C, Ruth TJ, Sossi V. Manganese-52 positron emission tomography tracer characterization and initial results in phantoms and in vivo. *Med Phys.* 2013;40.

219. Jodal L, Le Loirec C, Champion C. Positron range in PET imaging: non-conventional isotopes. *Phys Med Biol.* 2014;59:7419-7434.

220. Kim JS, Lee JS, Im KC, et al. Performance measurement of the microPET focus 120 scanner. *J Nucl Med.* 2007;48:1527-1535.

221. Zaidi H, Ruest T, Schoenahl F, Montandon ML. Comparative assessment of statistical brain MR image segmentation algorithms and their impact on partial volume correction in PET. *Neuroimage.* 2006;32:1591-1607.

222. Laasmaa M, Vendelin M, Peterson P. Application of regularized Richardson-Lucy algorithm for deconvolution of confocal microscopy images. *J Microsc.* 2011;243:124-140.

223. Nicolas Dey LB-Fe, Christophe Zimmer, Pascal Roux, Zvi Kam. 3D Microscopy Deconvolution using Richardson-Lucy Algorithm with Total Variation Regularization. *Research Report.* 2004;RR-5272:71.

224. Hofmann M, Pichler B, Scholkopf B, Beyer T. Towards quantitative PET/MRI: a review of MR-based attenuation correction techniques. *Eur J Nucl Med Mol Imaging.* 2009;36 Suppl 1:S93-104.

225. Wagenknecht G, Kaiser HJ, Mottaghy FM, Herzog H. MRI for attenuation correction in PET: methods and challenges. *MAGMA.* 2013;26:99-113.

226. Zaidi H, Del Guerra A. An outlook on future design of hybrid PET/MRI systems. *Med Phys.* 2011;38:5667-5689.

227. Zhang B. PD, Hu Z., Ojha N., Guo T., Muswick G., Tung C., and Kaste J. Attenuation correction for MR table and coils for a sequential PET/MR system. Paper presented at: Nuclear Science Symposium Conference Record (NSS/MIC), 2009; Orlando.

228. Delso G, Martinez-Moller A, Bundschuh RA, et al. Evaluation of the attenuation properties of MR equipment for its use in a whole-body PET/MR scanner. *Phys Med Biol.* 2010;55:4361-4374.

229. Hosokawa R, Nohara R, Fujibayashi Y, et al. Myocardial kinetics of iodine-123-BMIPP in canine myocardium after regional ischemia and reperfusion: implications for clinical SPECT. *J Nucl Med.* 1997;38:1857-1863.

230. Herzog H, Pietrzyk U, Shah NJ, Ziemons K. The current state, challenges and perspectives of MR-PET. *Neuroimage.* 2010;49:2072-2082.

231. MacDonald LR, Kohlmyer S, Liu C, Lewellen TK, Kinahan PE. Effects of MR surface coils on PET quantification. *Med Phys.* 2011;38:2948-2956.

232. Martinez-Moller A, Souvatzoglou M, Delso G, et al. Tissue Classification as a Potential Approach for Attenuation Correction in Whole-Body PET/MRI: Evaluation with PET/CT Data. *Journal of Nuclear Medicine.* 2009;50:520-526.

233. Bezrukov I, Schmidt H, Mantlik F, et al. MR-based attenuation correction methods for improved PET quantification in lesions within bone and susceptibility artifact regions. *J Nucl Med.* 2013;54:1768-1774.

234. Kartmann R, Paulus DH, Braun H, et al. Integrated PET/MR imaging: Automatic attenuation correction of flexible RF coils. *Med Phys.* 2013;40.

235. Kot M, Pilc A, Daniel WA. Simultaneous alterations of brain and plasma serotonin concentrations and liver cytochrome P450 in rats fed on a tryptophan-free diet. *Pharmacological Research.* 2012;66:292-299.

236. Ferguson A, McConathy J, Su Y, Hewing D, Laforest R. Attenuation Effects of MR Headphones During Brain PET/MR Studies. *J Nucl Med Technol.* 2014;42:93-100.

237. Reichert IL, Robson MD, Gatehouse PD, et al. Magnetic resonance imaging of cortical bone with ultrashort TE pulse sequences. *Magn Reson Imaging.* 2005;23:611-618.

238. Eldib M, Bini J, Robson PM, et al. Markerless attenuation correction for carotid MRI surface receiver coils in combined PET/MR imaging. *Phys Med Biol.* 2015;60:4705-4717.